The power of combining the radio and far infrared to study galaxy evolution

Ian Nicholas McCheyne

Submitted for the degree of Doctor of Philosophy
University of Sussex
September 2021

Declaration

I hereby declare that this thesis has not been and will not be submitted in whole or in part to another University for the award of any other degree.

Chapter 2 contributed to work that was published in *The LOFAR Two-meter Sky Survey: Deep Fields Data Release 1 III.Host-galaxy identifications and value added catalogues*, Kondapally et al 2021, Astronomy and Astrophysics, Volume 648. I contributed to this work by running the likelihood ratio method on the Lockman Hole data which this chapter focuses on, with details from the paper included to give context for this work.

Chapter 3 has been submitted to Astronomy and Astrophysics. I contributed to all aspects of the paper with other authors providing comments, helped in some aspects of the analysis and provided access to data.

Signature:

Ian Nicholas McCheyne

UNIVERSITY OF SUSSEX

Ian Nicholas McCheyne, Doctor of Philosophy

The power of combining the radio and far infrared to study galaxy evolution

Summary

This thesis focuses on how the combination of far infrared (FIR) and radio emission can be used to better understand galaxy evolution. Radio and FIR emission is linked to star formation, which plays a major role in the evolution of galaxies. I have combined FIR observations from *Herschel* and radio observation from the LOFAR radio telescope in order to take advantage of this.

Chapter 2 details the construction of a joint FIR-radio catalogue, using the likelihood ratio method, to link the radio catalogue to a multiwavelength optical/NIR catalogue. Subsequently the FIR fluxes were measured by deblending the FIR maps using the radio galaxies as positional priors. This method creates a perfect sample for measuring the far infrared radio correlation (FIRC). Chapter 3 focuses on the measurement of the FIRC at 150MHz with a mass complete sample. I find that the FIRC is primarily dependent on the stellar mass of the host galaxy with a minor dependence on the redshift.

Finally, chapter 4 describes how I used XID+ to measure the flux posterior for galaxies at 150MHz that were undetected in the LOFAR radio catalogues. I found that XID+ is able to accurately measure the flux of point like radio galaxies. These results were used to remeasure the FIRC and evaluate the best approach for extending XID+ to work on radio maps.

Acknowledgements

My First thanks of course goes to my supervisor Seb Oliver. He guided me through my PhD, always helping me keep my work in perspective and not get lost in coding optimisation. Despite his busy schedule he always managed to find time to provide help even if I just needed reassurance that what I was doing was right. I also want to thank Mark Sargent for his perspective on my work. He never failed to help me view my results from a different angle.

My thanks also go out to all the wonderful astronomers I have worked with both in and outside of Sussex. Special mention should go to my office mates over the years Ciaran, Chris, Dimitrios, Jess and Will who have always been happy be a wooden Indian when I needed it. Many thanks to all the HELP team members who were so supportive when I was starting my PhD and continued throughout; Maria, Pete, Raph, Ken, Kasia, Yannick and of course Louise.

I wouldn't have been able to overcome all the difficulties encountered during my PhD without the support of my good friends; Chris, who was always there to tell to give me a push when I needed it, Jack, whose optimism and faith in my abilities was consistent even when my imposter syndrome was at it highest and Alice, whose support and companionship during lockdown is probably the reason I got this thesis written in time.

Most importantly I want to thank my partner through this whole thing, Annie, who kept me sane during proposal deadlines and constantly telling me "You got dis". My brother Alex for making sure I always knew that most people don't care about physics in the real world and of course my parents who encouraged my curiosity and never told me to stop asking questions.

The most important step a man can take.

It's not the first one, is it?

It's the next one.

BRANDON SANDERSON

Contents

List of Tables

List of Figures

Chapter 1

Introduction

Galaxies are estimated to be the most numerous astronomical objects in the observable universe and how they evolve is one of the most fundamental questions in astronomy. There are a multitude of physical mechanisms whose interactions influence the growth and evolution of galaxies, from star formation to feedback from their active galactic nucleus (AGN). To estimate the effect these processes have on their host galaxy we need accurate flux measurements at wavelengths sensitive to these processes. In this thesis I will present my work on the Far Infrared Radio Correlation (FIRC) and how it can be used to inform the flux measurements of individual galaxies. In the introduction I will discuss how star formation (SF) affects the host galaxy's spectral energy distribution and the different tracers used to measure their SFR, focusing on the FIR and radio. I will then describe different techniques for measuring these tracers and how the individual detections at different wavelengths can be crossmatched. Next I will discuss the origins of the FIRC and how it can be used to calibrate the radio-SFR relation. This can be incorporated into a Bayesian hierarchical model to provide additional constraints when measuring the FIR and radio fluxes of individual galaxies and I will describe the underlying theory for such a model in my introduction.

Here I go through the electromagnetic spectrum and describe the physical mechanisms within a galaxy that produce emission of that type. I will then focus on how the Far InfraRed (FIR) and radio are observed and the surveys/data used in this thesis. Finally I will detail the Far Infrared Radio Correlation (FIRC) including previous measurements and the underlying theory.

1.1 Galaxies

Galaxies are the most common astronomical object that can be directly observed outside of the Milky Way. They form within dark matter halos, clusters of matter that have no electromagnetic interactions and are only affected by gravity, whose gravitational pull originally accreted hydrogen gas from the surrounding environment. Galaxies are composed of multiple different sources of electromagnetic radiation that are visible from modern telescopes. Stars, gas, dust and AGN are the main sources of emission from galaxies and they produce radiation that covers the whole electromagnetic spectrum. To describe a galaxy's emission I refer to their spectral energy distribution (SED). We can also model a galaxy's SED by modeling the underlying physical processes such as stellar emission and star formation. By fitting observations of the galaxy's emission at different wavelengths with a combination of these physical models we can measure the galaxy's underlying parameters such as it's stellar mass, age and star formation rate. Here we will focus on mechanisms behind SF and active galactic nuclei (AGN) and the emission produced by those mechanisms.

1.1.1 Star formation

Star formation in galaxies is affected by a variety of macro and microscopic processes. These range from the accretion of molecular hydrogen from the intracluster medium (ICM) to the collapse of a molecular cloud into individual stars. Fully understanding these process requires a detailed knowledge of astrochemistry, to model the creation of H_2 from H^+, and magnetohydrodynamics, to model the movement of the hydrogen gas in the form of an ionised plasma.

In short, H_2 began to accrete onto dark matter halos non uniformly, due to small scale density fluctuations in the gas or dark matter halo or electromagnetic interactions between the hydrogen molecules. These small fluctuations (small on the scale of the universe) could give rise to giant molecular clouds (GMC) which have a density of $\approx 100\mathbf{cm}^{-3}$. In these denser regions collisions between hydrogen molecules will occur more frequently and some of the kinetic energy of the collision will be converted to potential energy stored either by rotation, internal vibration or by raising an electron to a higher energy level. This stored energy can then be "lost" by emitting a photon which, if it escapes the GMC without being absorbed, will lower the average temperature of the GMC. As the cloud continues to lose energy it will collapse further causing a continued increase in density. The mass of the GMC required for collapse is known as the Jeans Mass (M_J) and is calculated by considering when the gravitational potential energy of the GMC overcomes the internal thermal energy and is calculated by,

$$M_J = \left(\frac{5k_bT}{Gm}\right)^{3/2}\left(\frac{3}{4\pi\rho}\right)^{1/2} \tag{1.1}$$

where m is the mean particle mass, T is the average temperature, k_b is the Boltzmann constant, and G is the gravitational constant. Considering only gravitational effects GMC's will take $\approx 10^6$years to collapse. However, this ideal situation does not occur. As the GMC collapses and its density increases there will be increased collisions and therefore more photon emission. As the kinetic energy in collisions increases the released photons energy also increases. The increased density will make it harder for these photons to escape the GMC and eventually the gas becomes opaque to these high energy photons. The effect of which is that temperature will rise as the density increases eventually causing the molecular hydrogen to dissociate into H^+. These combined effects make it harder for the cloud to cool so its average temperature will rise, causing M_J to increase and potentially halting collapse. Collapse will resume when either more mass has been accreted from the interstellar medium or the gas has had time to cool. Eventually the temperature will rise to the point where the kinetic energy of the protons in the centre, of the now proto star, is high enough to allow them to nearly overcome the coulomb barrier. To cover the remaining distance between them and allow the strong nuclear force to overcome the electromagnetic repulsion quantum tunneling occurs. This random movement of the protons within their probability cloud allows them to tunnel through the portion of the Coulomb barrier that their kinetic energy alone is not enough to overcome. Once this begins to occur then nuclear fusion will begin to take place, further raising the temperature, and therefore kinetic energy, of the surrounding protons. This will increases the likelihood of more fusion occurring in a runaway process that ends with a star forming.

An interesting property of the Jeans Mass is that it is $\propto \rho^{-1/2}$ so as the cloud collapses in a non uniform manner (due to turbulence) the Jeans Mass will also decrease. This means that as the GMC collapses non-uniformly it will fragment into smaller clumps that will collapse independently. These separate clumps can each form stars (presuming that the forming stars do not disrupt other clumps with their emission) of differing mass depending on how the cloud fragments. This fragmentation process is unpredictable and is governed by the exact density and temperature profile of the GMC as well as the effect of the internal and external magnetic fields.

It is also worth noting that the density of a GMC can increase through mechanisms other than gravitational collapse, such as compression caused by supernovae or AGN

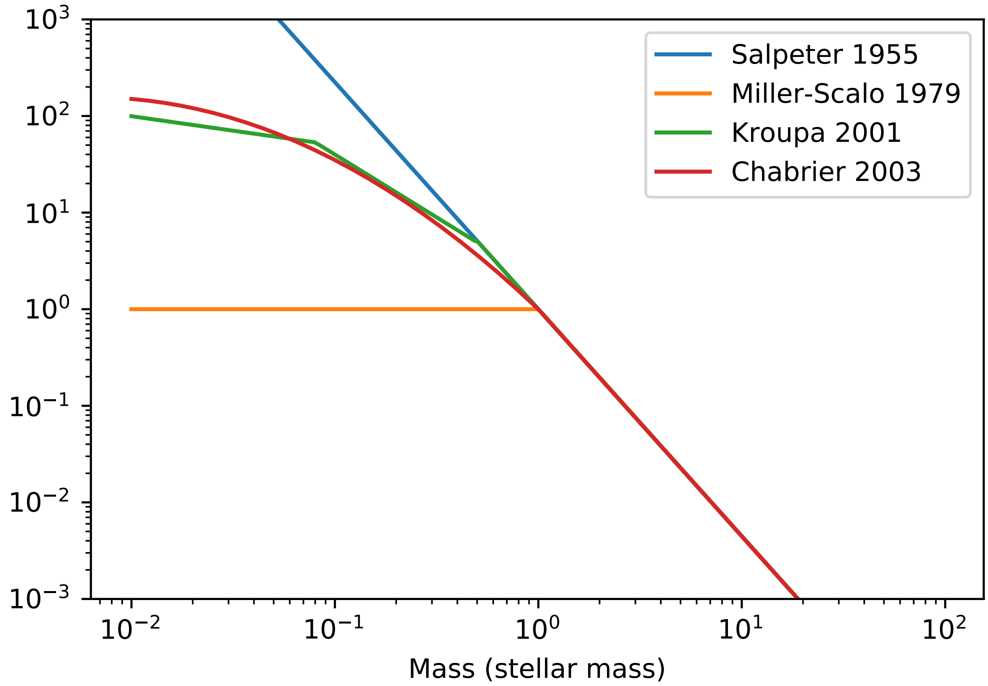

Figure 1.1: Comparison between four different initial mass functions from Salpeter (1955); Miller and Scalo (1979); Kroupa (2001); Chabrier (2003). All have been normalised to N(m)=1 at m=1$M_\odot$.

feedback, causing stars to form faster than when unaffected by outside feedback.

With star formation being dependent on so many physical processes a measure of a galaxy's SFR is essential to constrain models of galaxy evolution. There are multiple measures of SFR, most of which depend on the same underlying principle. Star formation occurs within giant molecular clouds (GMC) of H_2 as it splits into small dense regions that form individual stars. This splitting process is more likely to form less massive clumps, and therefore stars, than massive ones. The probability function of a star with a given mass forming is known as the initial mass function (IMF), one of the oldest is from Salpeter (1955) which is a linear relation (in log space) with slope -2.35 (. The stellar spectrum can be approximated as a blackbody of the form,

$$I(\lambda, T) = \frac{2hc^2}{\lambda^5}.\frac{1}{e^{\frac{hc}{k\lambda T}}} \tag{1.2}$$

where I is the intensity, λ is the wavelength, T is the temperature of the blackbody (in this case it is the surface temperature of the star) and h, c and k are Planck's constant, the speed of light and Boltzmann's constant respectively. The peak wavelength, as a function of temperature, can be found using Wien's law,

$$\lambda_{peak}(T) = \frac{2.9 \times 10^{-3} Km}{T} \tag{1.3}$$

and the bolometric luminosity can be calculated by integrating equation 1.2 across all wavelengths, which gives

$$L(T) = \sigma T^4 A \tag{1.4}$$

where σ is the Stefan-Boltzmann constant and A is the emitting area of the blackbody. It was found that a star's luminosity scales with its mass

$$L = M^{\alpha} \tag{1.5}$$

with alpha varying between 2.5-3.5. A star's lifetime (τ) is proportional to its mass divided by its luminosity. So by this we can show that massive stars will have shorter lifetimes then less massive stars, with the most massive stars having lifetimes on the scale of 10 million years. So if we know how many massive stars are in a galaxy we can combine that with our IMF to know the total mass of stars formed in roughly the last 10 million years. This principle forms the basis for measuring the SFR of a galaxy. By measuring different tracers for massive stars we can estimate a SFR for a galaxy using:

$$SFR = \alpha L_{tracer} \tag{1.6}$$

where L_{tracer} is the luminosity of the tracer we are using and α is the proportionality constant that needs calibrating. Massive stars have a higher luminosity (Equ 1.5) and therefore a higher temperature (Equ 1.4) causing the majority of their emission to be in the UV (1.3). Using stellar synthesis modules the UV luminosity proportionality constant is measured, this is described in greater detail in Kennicutt, Jr. (1998). UV continuum emission does have some disadvantages. Firstly, UV telescopes cannot operate from the ground as the atmosphere absorbs UV emission. This makes observing UV emission from low redshift galaxies difficult as you need a space based telescope (such as *Hubble*). The restframe UV emission from higher redshift galaxies can be measured from optical telescopes as it is redshifted out of the UV. For low redshift galaxies it would be ideal to have a SFR tracer at optical wavelengths. Fortunately massive stars are surrounded by gas (left over from when they formed) and their UV emission will ionise any H_2 into H^+. As electrons recombine with the H^+ ions and relax to their ground state ($n = 1$) they will typically transition from the $n = 3$ to $n = 2$ state (known as H-α) which emits a photon at 656.3nm. This is much more practical to observe as ground based telescopes can be used as well as specific filters that only transmit light with wavelengths close to 656.3nm. In theory many hydrogen lines could be used as SFR tracers but as $H-\alpha$ is the brightest optical emission line (and therefore easily observable for a large number of galaxies simultaneously) it is the most commonly used. However, due to $H-\alpha$'s high wavelength it is difficult to observe in high redshift galaxies. As it moves into the NIR instruments with high enough spectral resolution to measure the H-α line, for a large number of galaxies simultaneously, accurately do not currently exist.

All of these measures of SFR are still dependent on a large number of parameters. Any changes to the IMF or SPS models can have a dramatic effect on any SFR measurements. SPS models are constantly being improved by including additional stellar types, for example the Binary Population and Spectral Synthesis (BPASS) model (Eldridge et al., 2017) includes binary star systems in its SPS models. Binary star interactions lead to increased $H-\alpha$, UV and x-ray emission from the accretion disks present in many binary star systems. This changes the proportionality constants for these tracers decreasing the measured SFR for a fixed UV luminosity. Another major source of uncertainty is the form and evolution of the IMF. Direct measurements of the IMF come from globular clusters within our galaxy and other nearby galaxies. However, if the IMF varies depending on the galaxy's redshift or mass then measurements of the SFR would be incorrect. This is of particular issue for population III stars in the first galaxies. These stars formed without metals and therefore are expected to have different properties to population I and II stars. These uncertainties are usually unaccounted for in SFR measurements made from SED fitting as SED fitters can return the error with the parameter sace they are investigating. However, when comparing the measured SFR when some stars are in a binary system as opposed to all stars being solitary there will be a significant difference in the measured SFR. If the SED fitter used to measure the SFR does not consider both of these scenarios then its measured SFR uncertainty will not account for this additional uncertainty. Therefore these unaccounted for uncertainties should be held in mind throughout this thesis.

1.1.2 Dust

Despite galaxies containing billions of stars (on average) they are mostly empty. This empty space is filled with gas and dust which forms the interstellar medium (ISM). Emission from stars interacts with the ISM in a variety of ways that can modify the observed spectrum of an individual star or galaxy. Gas and dust absorb emission from stars and are heated. This heated material then radiates as a blackbody, leading to increased emission at longer wavelengths. Understanding how this emission is absorbed, what wavelengths are most affected by this absorption and the spectrum of the re emitted light is a crucial step in understanding a galaxy's spectra. In this section we will focus on answering these questions for the dust within the ISM. While gas plays a vital role in SF my research focuses on the affect that dust has on our ability to measure the underlying physical parameters of a galaxy (such as stellar mass and SFR).

Dust in the ISM takes the form of molecular grains that cluster together to form larger grains, whose sizes range from nanometers to hundreds of micrometers in diameter. These molecules are composed of metals (in astronomy metals are defined as any elements heavier than helium) formed in massive stars. How these molecules bond together to form large dust grains is still in debate. There has been evidence for dust forming from AGB stars and in supernova remnants. However, both of these processes could also be responsible for the destruction of large dust grains so their net effect is still being investigated. Dust also plays an important role in SF. Stars are formed in collapsing clouds of molecular hydrogen. The formation of molecular hydrogen from H^+ is catalysed on the surface of dust grains. This ensures that most SF occurs within dusty regions. Though the geometry and mass of the dust within the SFR region can vary from region to region.

The amount of light absorbed by dust varies with wavelength and is described by an attenuation or extinction curve. These curves have been measured by comparing the difference in luminosity of the Balmer lines. The relative height of these lines can be calculated theoretically and by observing the discrepancy from the theory the attenuation curve can be measured. In addition, the slope of the UV spectrum can also be used to measure the attenuation curve of a galaxy. Both of these methods require high spectral resolution measurements of a galaxy that can be difficult to obtain for a variety of galaxies (those with low luminosities or high redshift galaxies for instance). So for galaxies whose attenuation curve cannot be measured directly an attenuation curve is typically assumed. Several models are commonly used including the Calzetti law (Calzetti et al., 1994) and the observed attenuation of the Andromeda galaxy, to name a few. While the exact shape of these attenuation curves varies they all show a much stronger absorption at shorter wavelengths. This can lead to dusty galaxies having no observable UV emission as it is all absorbed by dust in the ISM and can cause significant reddening.

This can cause obvious problems when measuring the SFR of a galaxy. If the SFR is being estimated from the UV or Balmer lines then any emission absorbed by dust will cause the SFR of the galaxy to be underestimated. The dust attenuation can be accounted for theoretically, but in practice this can be difficult to do for a galaxy whose UV flux density is below your detection limit. On top of this the choice of attenuation law can cause significant differences in your measurement of SFR.

The best way to account for this is to directly measure the amount of energy that is being absorbed by dust in the ISM. This is possible because the absorbed UV and optical emission heats up the dust and causes it to emit radiation in the IR. If the FIR SED can be measured then the total infrared (TIR) luminosity (typically defined as between $8 - 1000\mu$ m) is equal to the absorbed UV and optical luminosity. Ideally you would measure the SFR of a galaxy by measuring the UV luminosity and the TIR luminosity of your galaxy and calibrate this against some measure of SFR that is unaffected by dust emission. More recent SF tracers that exist at longer wavelengths include some oxygen emission lines (Wilkins et al., 2020).

If we want to measure the TIR luminosity we need a model for the FIR SED. The simplest model is that the dust is uniformly heated so that all the dust has the same temperature. If all the dust grains had the same makeup and size then the FIR SED would be a simple blackbody whose temperature we could measure from the peak of the SED (assuming the redshift of the galaxy was known). Unfortunately these assumptions are untrue, with each dust grain having its own temperature and structure. This ignores the internal chemistry of the dust grains, which would change each dust grain's individual SED from a blackbody to a combination of a blackbody and complex series of emission lines, dependent on the molecular structure of the grain. In practice these individual SEDs are far to complex to model and the FIR SED can be well approximated as a modified blackbody, known as a greybody, of the form

$$S(\nu) = \frac{(1 - e^{-\tau(\nu)})\nu^3}{e^{h\nu/kT} - 1} \tag{1.7}$$

where the $(1 - e^{-\tau(\nu)})$ term accounts for absorption along the line of sight as well as the non uniform emissivity of the individual dust grains, which is dependent on the frequency (ν) and typically $\tau(\nu) = (\nu/\nu_0)^\beta$. T is the average temperature of the dust and h and k and Plank and Boltzman's constant respectively. In the optically thin case where $\nu << \nu_0$ (for the frequency range that covers the FIR) then $(1 - e^{-\tau(\nu)})$ simplifies to ν^β and the equation becomes

$$S(\nu) = \frac{\nu^{\beta+3}}{e^{h\nu/kT} - 1} \tag{1.8}$$

Due to the small number of free parameters in the greybody model (there are four if you include redshift and TIR luminosity) it can be fit to a small number of photometric observations in the FIR. This fitted greybody can be used to measure properties of the dust SED as a whole such as the TIR luminosity and dust temperature within a reasonable degree of accuracy. It should be noted that if using photometric observations then they should cover the peak of the FIR SED, otherwise the TIR luminosity is near impossible to constrain. It should also be noted that a greybody does not match the polycyclic aromatic hydrocarbon (PAH) spectral features observed in the MIR (typically defined at $5 - 40\mu$m). However, these features have a very minor affect on the TIR luminosity and not accounting for them causes a smaller affect than the measurement uncertainty. Measuring the redshift and temperature of a greybody can have complications. The major effect of temperature is to change the peak of the FIR SED and redshift similarly causes the peak to move. This leads to a degeneracy between redshift and temperature when fitting greybodies. The ideal way to break this degeneracy is to know the redshift of the galaxy beforehand. Either from spectral line measurements of from photometric redshift estimates (e.g. by using Easy and Accurate Z from Yale, EAZY Brammer et al. (2008)). The final free parameter in the greybody equation is the emissivity, which mainly affects the Rayleigh-Jeans tail at long wavelengths and therefore require multiple measurements along the tail to be constrained. Emissivity has been found to vary between $1 - 2.5$ with most works assuming a fixed value of 1.5 (see Casey (2012) for more detail on this topic).

We have now discussed multiple tracers of SFR in galaxies many of which have a complex interplay between them. So how can we combine all these different tracers of SF together to accurately measure the total SFR of a galaxy? The answer is usually to measure the obscured and unobscured SFR and add them together. Obscured SFR can be measured from a monochromatic flux or from the TIR luminosity, while the unobscured SFR is measured from on the many optical/UV tracers discussed above.

Finally we should discuss the role of SED fitters in measuring the SFR of a galaxy. SED fitters, such as *magphys* (Da Cunha et al., 2008) and *CIGALE* (Boquien et al., 2018) fit the underlying physical parameters of a galaxy, such as stellar mass, age, metallicity, dust mass and SFR from photometric measurements of the galaxy from the x-ray to radio. Each source of emission in a galaxy is modelled from the stellar emission to any potential AGN emission. For example, a galaxy's star formation history (SFH), which is a galaxy's SFR as a function of age, in combination with an IMF and SPS models can provide a model for a galaxy's unobscured SED in the UV to NIR. If we model a galaxy's SFH as exponentially decaying, plus a burst of SF that also decays exponentially with the following equation,

$$SFR(t) = SFR_{delayed}(t) + SFR_{burst}(t) \tag{1.9}$$

where $SFR(t)$ is the SFH $SFR_{delayed} \propto te^{-t/\tau_{main}}$ and $SFR_{burst} \propto e^{-(t-t_0)/\tau_{burst}}$ as long as $t > t_0$ and $SFR_{burst} = 0$ if $t < t_0$. The factor τ is the e folding time for the main stellar population and a late starburst population (More details of this SFH model can be found in Ciesla et al. (2015)). We can predict the number of stars, as well as their mass in the galaxy. Combining this with SPS models we can predict the spectrum of our galaxy in the UV to NIR. This predicted spectrum can be further modified by additional models that account for other sources of emission, such as nebular emission, dust absorption and emission from AGN. By comparing this predicted spectrum to observations (either photometric or spectral) we can use the fitted models parameters to measure physical properties of the observed galaxy, such as the current SFR, stellar mass, dust temperature (if we have FIR observations) and the presence or absence of an AGN.

By simultaneously fitting the entire galaxy's SED, consistency checks can be used to better calibrate certain aspects of the SED fitting. For the purposes of this work the most important is the use of energy balance. This is the process of calculating the amount of energy absorbed by dust in the UV and optical and comparing it to the energy emitted in the IR. This can be used to ensure that neither the IR or UV/optical are being incorrectly fit and can point out incorrect flux measurements or cases where FIR emission has been incorrectly attributed to a galaxy. This technique has also been used to constrain the TIR luminosity for galaxies with no FIR flux measurements(Małek et al., 2019).

1.1.3 Radio

So far we have focused on measures of SF that directly measure emission from massive stars. However, massive stars affect their local environment in a variety of ways outside of their electromagnetic radiation. Firstly massive stars (with $M > 8M_\odot$) produce type Ib, Ic and type II supernova. Both of which produce shock waves in the ISM that accelerate cosmic ray (CR) particles. These CRs are moving in the presence of the galactic magnetic field, causing them to experience a Lorentz force of the form

$$\mathbf{F} = q\mathbf{v} \times \mathbf{B} \tag{1.10}$$

where $\mathbf{F}$ is the force experienced by the charged particle, q is the charge of the particle, $\mathbf{v}$ is its velocity and $\mathbf{B}$ is the magnetic field it is passing through. This causes the CR to spiral in the galactic magnetic field and emit synchrotron radiation as the charged particles (usually only electrons are considered) are accelerated by the galactic magnetic field. Each individual cosmic ray will have an individual spectrum depending on its energy and the strength of the magnetic field perpendicular to it's velocity. When averaging over all CR in a galaxy it is found that the combined spectrum from synchrotron radiation form a power law with a slope (which in this context is called the spectral index). Typical values of this slope have been measured around -0.7 (though the exact value varies from galaxy to galaxy and depending on the frequency range considered). However, the slope of the synchrotron spectrum is dependent on the individual CR spectra, which in turn is dependent on their energy. As CR emit synchrotron radiation they will lose energy and thus their spectra will change. The CR with the highest energy are responsible for emission at shorter wavelengths and therefore result in an overall shallower spectra. Therefore we can deduce that galaxies with a lower spectral index (and therefore steeper spectra) have had supernovae more recently and therefore injected more energy into their CRs.

Massive stars are also responsible for radio emission through a separate mechanism, free free emission. As massive stars will primarily emit high energy UV photons with > 13.6eV (the amount of energy needed to eject an electron from the n=1 shell of atomic hydrogen) they are surrounded by a shell of ionised H^+ gas. The ionised gas will be in the form of a very low density plasma composed primarily of protons and electrons. Collisions between these particles will give rise to thermal bremsstrahlung radiation as one of the particles, typically the electrons, is slowed by its collision with another particle, typically a proton or heavier metal nucleus. Collisions between particles of the same mass result in smaller changes of momentum and therefore production of fewer photons. This emission is referred to as free free emission because the emitting electron is free at the beginning and end of the emission mechanism. Calculating the expected spectrum of this free free emission is a difficult task. The emitted energy of a cloud of ionised H^+ is dependent on the distribution of electron velocities (as during electron proton collisions the electrons will have a much greater velocity as all particles will have similar kinetic energy if the gas is in thermal equilibrium) and the collision parameters. Solving the necessary equations requires making reasonable assumptions about a number of these parameters. With reasonable assumptions it is found that the predicted spectrum from free free emission have a spectral index of $\simeq -0.1$ and has a lower luminosity then the synchrotron emission (figure 1.2).

Both of these emission mechanisms require massive stars and therefore can be used as a tracer of recent SF as massive stars have a short lifetime and therefore if observed must

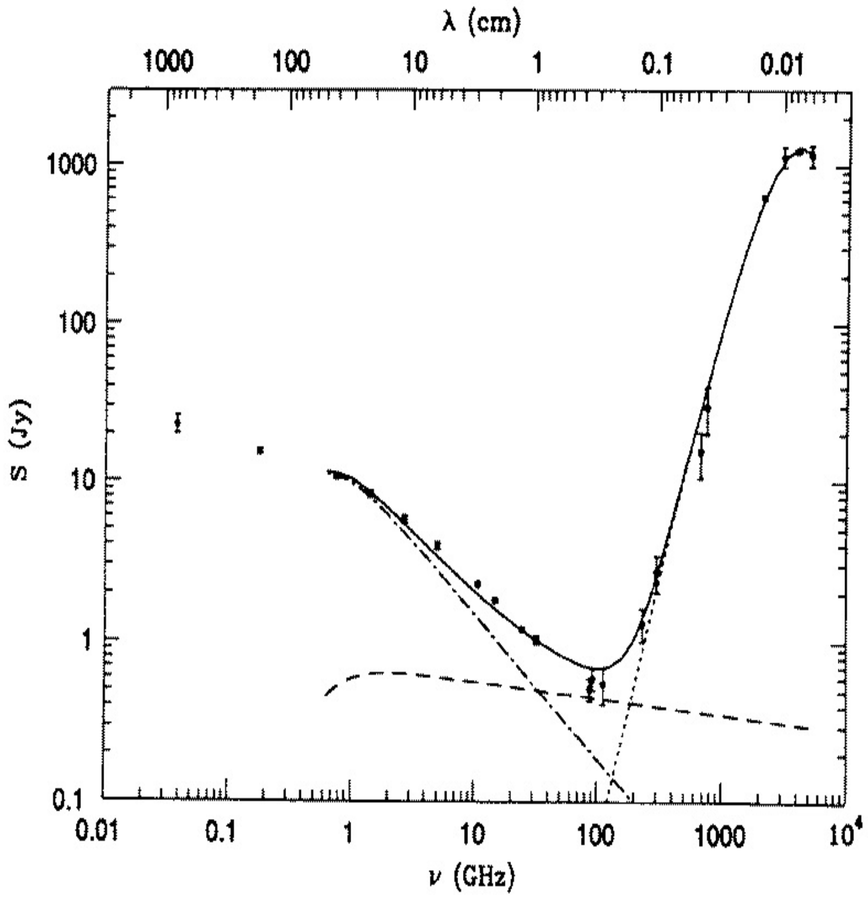

Figure 1.2: Spectrum of M82 in the radio and FIR. The black points are from Webber and Willis (1971) and Carlstrom and Kronberg (1991). The solid black line is the total SED while the dot-dash and dashed lines are the synchrotron and free free emission respectively and the dotted line is the dust emission. Credit: Terzian (1972).

have formed recently. By converting emission from predominately massive stars, such as the synchrotron emission from supernova produced by massive stars, to the number of massive stars, using a proportionality constant, then the SFR can be ascertained from this (this requires a measurement or assumed IMF, see section 1.1.1). However, finding a theoretical proportionality constant between radio luminosity, at a given frequency, and SFR is a complicated problem. Unlike the UV, where stellar synthesis models can accurately predict the UV emission of a massive star, predicting the amount of synchrotron and free free emission produced by a massive stars has many unknowns. The main unknown for synchrotron radiation is the amount of energy transferred to the ISM as well as the density of CR within the ISM. Free free emission is even more uncertain with a large number of parameters (see above) that are poorly constrained and hard to measure. These uncertainties mean that calibrating the radio SFR relation is best done by comparing the radio luminosity of a galaxy to its SFR, measured using another known SF tracer. However, this process can lead to biases depending on the radio galaxies selected to form the sample. In addition, the physical mechanisms behind synchrotron and free free emission could change with an individual galaxy's properties, such as redshift, stellar mass or spectral index. For example, at higher redshift there is expected to be reverse Compton scattering between the synchrotron radiation and the cosmic microwave background which is predicted to decrease the radio emission from high redshift galaxies. However, despite these difficulties radio SFR provide an ideal advantage over SFR measured from the UV, optical or FIR. Radio emission is unaffected by dust along the line of sight so can provide accurate SFR for dusty galaxies that are undetected in the UV/optical. In addition radio telescopes, through the use of interferometry, can provide high resolution images with full width half maximums (FWHM) of < 1" as well as cover wide areas of the sky (Van Haarlem et al., 2013; Dewdney et al., 2009). This is in contrast to current FIR observations from *Herschel* which while covering over 1000deg^2 have a large angular resolution of > 18" depending on the wavelength observed.

1.2 AGN

Quasi Stellar Objects (QSOs) were first discovered by Schmidt (1963) by matching a bright radio source to an optical counterpart. This spectrum of the optical object was observed to have extremely bright Balmer emission lines which placed it at a redshift of 0.158 (at the time placing it in the high redshift category). This suggested that the luminosity of this object was ≈ 100 times greater than the typical spiral galaxy yet the emission originated from a compact point source. As time went on more and more QSOs were observed and found to outshine their host galaxy. Observationally QSOs are roughly defined as having strong emission lines, blue colours and generally high redshifts. The bright radio emission that originally drew attention to the first QSO was not replicated in the majority of later identified QSOs based on their optical properties. Finally radio galaxies were identified as galaxies with large roughly symmetric radio lobes. These radio galaxies were later categorised as radio loud AGN.

These individually discovered objects (Seyfert galaxies, QSO's and radio galaxies) were eventually found to originate from the same astrophysical mechanism. In 1933 Jansky (1933) made the first observation of Sagittarius A, the supermassive black hole (SMBH) in the centre of the Milky Way, at 20.5MHz. It is now believed that at the centre of every galaxy there is a super massive black hole (SMBH) that plays a significant role in the galaxy's evolution. As these SMBH accrete matter they produce huge amounts of electromagnetic radiation from the x-ray to radio in addition to releasing energetic particles into the ISM. This can significantly affect observations of the host galaxy as the most powerful AGN have been known to outshine their host galaxy. It is these Active Galactic Nucleai (AGN) that are responsible for observations of Seyfert galaxies, QSOs and radio galaxies.

How can an accreting SMBH be responsible for the wide variety of observations seen from Seyfert galaxies, QSOs and radio galaxies? The most widely accepted theory in the unified model first proposed by Antonucci (1993) postulated that the variety of observed AGN is caused by a combination of two parameters: the inclination of the plane of rotation of the SMBH and the source's luminosity. In this model AGN are made up of several components:

1. A subparsec-rotation-dominated accretion flow that we will refer to as a accretion disc.

2. High density dust clumps moving at Keplerian velocities around 0.01-1pc from the SMBH (known as the Broad Line Region or BLR).

3. Surrounding the accretion disc is an asymmetric dusty torus that can span 0.1-10pc (dependent on the luminosity).

4. Outside the torus and along the direction along the opening in the torus there is lower density gas moving at lower velocities than the gas in the BLR and is known as the Narrow Line Region (NLR).

5. Occasionally a radio jet is associated with the AGN

Whether emission from these individual components is observed is dependent on the inclination of the AGN to the observer. If the torus' axis of rotation is facing the observer then the accretion disc and BLR will be directly observable. This will cause the galaxy to have an abundance of UV and x-ray emission, from the accretion disc, as well as exhibit broad spectral lines. Conversely if the torus has an inclination of 90 degrees to the observer than it is likely that neither of these will be observed (presuming the torus is optically thick in all directions). However, the presence of the AGN could still be detected from an excess of emission in the NIR and MIR from the torus itself. Figure 1.3 shows how the viewing angle of the observer to the rotational plane of the AGN dictates which type of AGN is observed.

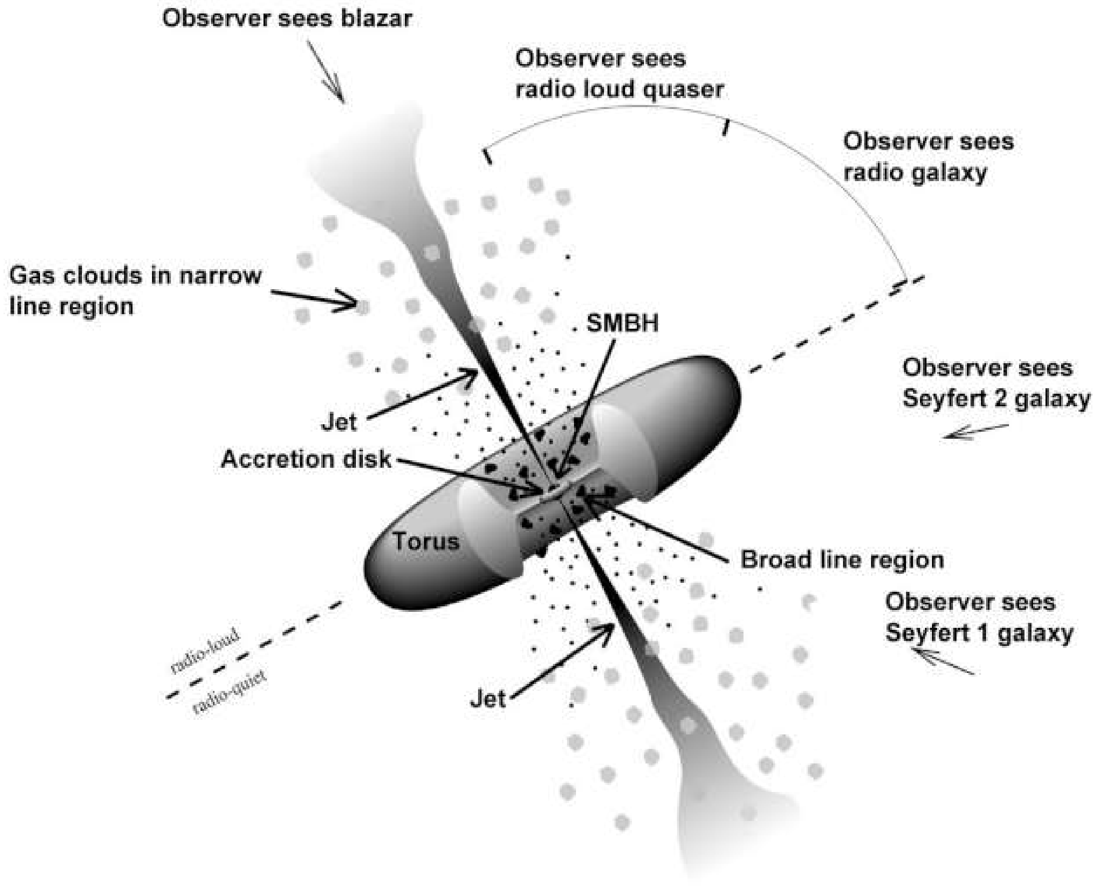

Figure 1.3: Visual image of the AGN unification scheme which shows how the viewing angle of the observer can affect the type of AGN observed. The dotted line shows the difference between a radio loud or radio quiet AGN as the main difference between Seyferts and QSO/radio galaxies is the AGN luminosity. Credit: Fermi and NASA: https://fermi.gsfc.nasa.gov/science/eteu/agn/

AGN also affect their host galaxy in a number of ways. Evidence for this can be seen in both the $M_{BH} - \sigma$ relation and the cosmic SFR and AGN accretion rate. Ferrarese and Merritt (2000) observed a correlation between a a galaxy's velocity dispersion in the bulge and the mass of its central SMBH. These results were later updated by Woo et al. (2013), who showed that the relation was the same for galaxies that were hosting an AGN and those that were not. This suggests that the central SMBH of a galaxy affects more than its immediate vicinity and therefore has additional affects on its host galaxies that cannot be explained by its gravitational force alone. The cosmic SFR density and the AGN accretion rate volume density are also found to be in alignment (Bouwens et al., 2012; Aird et al., 2010) suggesting that both SF and AGN accretion originate from the same processes.

There is evidence for AGN feedback affecting their host galaxy and is typically divided into two forms: radiative mode and radio mode. The radiative mode is thought to originate from the radiation from AGN that are efficiently accreting cold gas. This radiation will heat gas in the central region of the galaxy and cause outflows of gas, see Fabian (2012) for a review on the topic. While these radiation driven winds can be caused by SF and supernovae these are unlikely to generate high enough velocities, in a substantial enough amount of gas, to cause a significant decrease in the galaxies SF for longer than a few thousand years, see review by Veilleux et al. (2005). These slower winds will only cause a small fraction of the galaxies gas to escape from its gravitational well. This gas will eventually cool and fall back into the galaxy where it can be used to fuel additional SF so feedback from SF and supernovae are unlikely to be responsible for quenching galaxies. By using emission line data velocities of $1000\mathrm{kms}^{-1}$ and mass outflow rates of $1200\mathrm{M}_{\odot}\mathrm{yr}^{-1}$ have been measured in the central parsec region of the AGN (Pérez-Torres et al., 2021) making it unlikely that they can remove sufficient gas from the galaxy to fully quench the galaxy. At higher redshifts there is evidence for larger outflows on kpc scales (Harrison et al., 2012). However, these outflows are found to effect low density gas found throughout the galaxy without impacting the dense gas responsible for SF. In addition, these high outflows are primarily seen in extreme QSOs and rarely seen in lower mass star forming galaxies. This limits the evidence for radiative feedback to impact the majority of galaxies and therefore its importance is still debated.

Radio mode is the other main mechanism for AGN feedback and is caused by the kinetic energy contained with the radio jets. This released mechanical energy can do significant work on the host galaxy and its surrounding environment. This kinetic energy can be larger than the radio luminosity of the AGN. As radio jets are triggered by hot gas within the local halo cooling and accreting onto the AGN they are expected to be self regulating in all but the most massive galaxies. As the radio jet deposits mechanical energy into the surrounding gas it will cause it to heat at a rate that is equal to or exceeds to its cooling rate. With the gas unable to effectively cool itself it will be unable to collapse and be accreted onto the AGN. With its fuel supply cut off the jets will cease and the gas heating will stop. The gas will then be able to cool again, accretion will resume and the jets will be triggered again. This self regulating cycle will have a significant impact on the host galaxy as the jets will heat gas within the host galaxy and prevent star formation. The heated gas within the halo will also affect other nearby galaxies. The heated gas will need to cool before it can collapse onto any galaxy and could reduce SF in nearby galaxies. Evidence for this can be seen from x-ray observations of galaxy clusters where a hot cavity is seen that overlaps with the radio emission. These cavities can be used to estimate the mechanical energy of the jet that created them. The energy is assumed to be proportional to ρV of the cavity (Birzan et al., 2004) such that $E_{cav} = f_{cav}\rho V$ where E_{cav} is the energy of the cavity and f_{cav} is the proportionality constant. This constant must be greater than one for the cavity to have formed and the relativistic plasmas within the jets are found to have values close to 4.

However, there is some evidence that radio mode feedback can result in increased SFR. Molnár et al. (2017) found evidence in HE04502958 that its radio jet was impacting the SF of its neighbouring galaxy. The shock of the jet was postulated to be compressing gas within the neighbouring galaxy and potentially inducing SF. If this is true it is not unreasonable to assume that similar jet induced SF could be present in jet mode galaxies during the early stages of the jets formation. However, as jets are expected to have lifetimes on the order of 10^7 years and this shock induced SF would only occur during the early stages of the jet it is unlikely to observe a system in which this occurring. Adding to this unlikelihood is the rarity of radio jet galaxies.

Additionally, there is potential for AGN emission to heat dust in the ISM on kpc scales (Symeonidis et al., 2016). If so then Some IR emission from ultra luminous infrared galaxies (ULIRGS, galaxies whose $\mathrm{L}_{TIR} > 10^{13}\mathrm{L}_{\odot}$) may be attributed to the AGN rather than from SF, as is typically assumed. While this is not the classical definition of feedback this affect of the AGN on its host galaxy would cause the observed SFR to artificially inflated unless the TIR luminosity is corrected for any AGN contamination.

Finally many cosmological simulations have found it necessary to introduce AGN feedback in some manner in order to match the observed galaxy mass function and galaxy luminosity function. AGN feedback introduced in either a heuristic approach or physically motivated prevents continued SF in galaxies. Without this feedback simulations find a greater number of massive/luminous galaxies compared to when AGN feedback is included (Croton et al., 2006) and is further evidence for the importance of AGN feedback in galaxy evolution.

1.3 Simulations

Understanding the physical processes behind galaxy formation and evolution is a complex task. There are huge number of interacting effects and many of them occur stocastically, which causes difficultly in creating concrete predictions which can be compared to observations. However, by simulating the some volume of the universe we can predict what kind of universe a given set of initial conditions and physical processes would produce. By comparing some simple parameters of the simulated universe with our observed universe (such as the galaxy mass function) we can determine what cosmological parameters our universe has (such as Hubble's constant, which tells us the expansion rate of the universe). However, simulating the even a fraction of the universe for 13 billion years is an extremely complex task. It would be impossible to simulate every individual article as well as the numerous interactions between them in detail with our current hardware. To overcome this issue several different approaches are taken. N-body simulations are typically used to simulate collisonless fluids such as dark matter. Baryonic matter can be simulated either using a semi-analytic model (SAM) or a Hydrodynamic simulation.

1.3.1 N-body Simulations

Galaxies form within the gravitational potential wells of dark matter halos so simulating the formation of the dark matter halos is an essential part of any cosmological simulation. Luckily as dark matter only interacts with other particles gravitationally so can be well modelled as a collisionless fluid. The usually approach is to populate a co-moving volume with dark matter and periodic boundary conditions. The Newtonian gravitational force between the dark matter particles can then be calculated and their motion calculated from this (the effects of general relatively are mild and therefore ignored). The number of calculations needed for this scales with N^2 where N is the number of dark matter particles. More efficient algorithms have been developed to decrease the computational burden such as the hierachical tree approach. This method divides the dark matter particles in groups (based on proximity) that are in turn grouped together into larger groups and so on. The gravitational force between distant groups can be approximated by using the mass of the group as a whole rather then calculating the force from each particle individually. This algorithm scales with $N\mathbf{log}(N)$ and was used by the Millenium simulation (Springel et al., 2005) which simulated a cubic box (with side length of roughly 2 billion light years) from z=127 to z=0.

1.3.2 Semi-analytic models

Semi-analytic models are built on top of the outputs of dark matter only simulations. They use differential equations as well as the movement of the underlying dark matter particles to simulate how the baryonic matter, and therefore galaxies, evolve (Baugh, 2006). One example of a SAM is L-Galxies (Guo et al., 2011). The growth of supermassive black holes (SMBH) in the centre of galaxies is governed by two different mechanisms. The first is controlled by galaxy mergers and causes the merged galaxies' SMBH's mass to be equal to the sum of the galaxies' SMBH before the merger (this is called the quasar mode). Afterwards there is a period of accretion of cold gas. Secondly the SMBH can accrete hot gas from the dark matter halo and leads to hot bubbles of gas and jets (known as the radio mode). The quasar mode results in rapid growth of SMBH without inducing significant feedback while the radio mode results in limited growth but causes significant feedback that prevents accretion of cold gas from the dark matter halo.

1.3.3 Hydrodynamic Simulations

Hydrodynamic simulations model the baryonic and dark matter simultaneously. This approach allows a consistent approach to measure the properties of both. These simulations are computationally expensive and therefore are run on smaller regions than N-body simulations. For example the Evolution and Assembly of GaLaxies and their Environments (*Eagle*, Schaye et al. (2015)) simulation was run on a co moving volume of 100Mpc^3 (compare this to the Millennium simulation that was run 10 years prior). In addition, the spatial resolution of these simulations is limited and for scales below this resolution sub grid models need to be employed. These are similar to SAMs but on a smaller scale.

The SIMBA simulation (Davé et al., 2019) is a modern state of the art hydrodynamic simulation that uses physically motivated feedback from SF and AGN to model the quenching of SF galaxies. It builds on the previous simulation ,MUFASA (Davé et al., 2016), which used a heuristic approach to model AGN feedback. In SIMBA AGN accretion occurs in two modes: torque limited accretion and Bondi accretion (Bondi, 1952) the former for cold gas (T$\leq 10^5$K) and the latter for hot gas. Torque limited accretion is appropriate for gravitationally driven instabilities on the galactic scale down to the scale of the accretion disk which predominately affect cold gas in the ISM. However, for hot gas Bondi accretion is a more suitable model as this gas tends to be spherically distributed and is computed with the standard formula

$$\dot{M}_{Bondi} = \epsilon_m \frac{4\pi G^2 M_{BH}^2 \rho}{(\nu^2 + c_s^2)^{3/2}} \tag{1.11}$$

where $\dot{M}_{Bondi}$ is the Bondi accretion rate, ϵ_m is the efficiency of the Bondi accretion and is taken to be 0.1, G is the gravitatonal constant, M_{BH} is the mass of the SMBH, ρ is the mean density of hot gas around the SMBH, ν is the average velocity difference between the gas and the SMBH and c_s is the speed of sound of the gas. The total accretion rate is the sum of these two modes multiplied by a radiative efficiency factor of 0.9. This accretion rate is further limited to the Eddington accretion rate.

These accretion rates were then used to compute the AGN feedback and its affect on the host galaxy and its environment. This feedback has two main forms: kinetic and x-ray. Kinetic feedback is when nearby gas particles are randomly injected with momentum (the probability of injection is dependant on the mass of the particle and the accretion rate). The exact momentum injection is dependant on the accretion rate of the SMBH with higher accretion rates leading to lower momentum injections (these are refered to as radiative AGN winds) and as the accretion rate drops below 0.2f_{edd} (where f_{edd} is the eddington ratio) the injected momentum increases (known as jet mode). It should be noted that jets have not been observed from low mass SMBH so jet mode is prevented for SMBH with M$< 10^{7.5} M_*$. X-ray feedback simulates the heating of the ISM by x-rays emitted from the inner region of the accretion disk. This feedback is only simulated for AGN in jet mode as in more gas rich galaxies the gas would be able to efficiently absorb and radiate away the excess heat. For non ISM gas affected by this feedback the temperature is raised based on the heating flux at its position. However, If this was done for ISM gas directly the physics of the SIMBA simulation would cause the heat to radiate away quickly, due to the low resolution and high pressure of the ISM. This physically unrealistic result is a consequence of the limitations of the simuations rather than a physically relevant result. To more closely mirror observations half of the heat is added as a radial kick outwards.

In later works using SIMBA radio luminosities were derived for simulated galaxies. These radio luminosities were made up of contributions from the AGN and from SF. SF radio luminosities were derived using the relations from Terzian (1972). This requires the number of supernovae and can be derived from the SFR and the IMF (they used the IMF of Chabrier (2003)). This gives the radio power from both thermal and synchrotron emission as

$$\left(\frac{P_{non-thermal}}{WHz^{-1}}\right) = 5.3 \times 10^{21} \left(\frac{\nu}{GHz}\right)^{-0.8} \left(\frac{SFR[M > M_{\odot}]}{M_{\odot}yr^{-1}}\right), \tag{1.12}$$

$$\left(\frac{P_{thermal}}{WHz^{-1}}\right) = 5.5 \times 10^{20} \left(\frac{\nu}{GHz}\right)^{-0.1} \left(\frac{SFR[M > M_{\odot}]}{M_{\odot}yr^{-1}}\right), \tag{1.13}$$

where ν is the observed frequency and $SFR[M > M_{\odot}]$ is the rate of formation of stars with mass larger than 5M$_{\odot}$. The total radio power is taken as the sum of these two emission mechanism powers.

AGN radio emission comes from core emission as well as extended emission from the jets. Core emission was computed using the empirical relation from Körding et al. (2008)'

$$\frac{P_{rad}}{10^{30}ergs^{-1}} = \left(\frac{\dot{M}_{BH}}{4 \times 10^{17}gs^{-1}}\right)^{17/12}. \tag{1.14}$$

This formula describes optically thick emission from the accretion disk typically within ten parsecs of the SMBH. The more complex extended emission is harder to model. Luckily, depending on your point view, galaxies with extended emission are rare and due to the relativeky small size of the simulated volume (it has a comoving volume of 100Mpc^3) these type of galaxies are not present. Alternatively these galaxies are not observed in SIMBA due to the feedback models being unable to produce galaxies with high enough accretion rates at z=0.

With the addition of radio luminosities to the SIMBA simulation they were able to predict the total radio luminosity function as well as the individual radio luminosity function for SF galaxies and AGN. They found that AGN dominate the luminosity function at high radio powers with the crossover at P$\approx$10$^{22.5}$ at z=0. This crossover power increased with redshift as the relative importance of AGN decreased, while the total luminosity function remained relatively unchanged, with the crossover occurring at P$\approx$10$^{24.5}$ at z=3. The radio luminocity functions found in SIMBA are a good match to the results of Mauch and Sadler (2007) suggesting that the feedback mechanisms used in SIMBA to simulate AGN feedback are good approximations for the true physial processing occuring in galaxies. However, caution should be taken for the most luminous radio galaxies that are not found in within SIMBA. It is difficult to know whether the lack of radio loud QSOs is a result of the feedback models being unable to produce AGN of this type of whether their absence is just random chance in small simulation.

1.4 FIR Observations

Observing in the FIR (typically defined as 15-1000μm) is a necessary compliment to UV and emission line measurements when measuring the SFR of a galaxy due to dust absorption in the ISM. However, FIR observations have some unique technical problems that need to be overcome in order for useful observations to be made. Firstly the resolution of any telescope is given by

$$\theta \simeq \frac{\lambda}{D} \tag{1.15}$$

where θ is the resolution in radians, λ is the observed wavelength and D is the diameter of the telescope lens. So an optical telescope observing at 300-700nm will have a resolution 100x better than a FIR telescope. In addition, the atmosphere absorbs FIR radiation meaning that FIR telescope need to be space based, making building large telescopes (with high resolution) nearly impossible.

1.4.1 Bolometers

The history of FIR astronomy began with the discovery of infrared radiation by William Herschel. He discovered this while attempting to measure the amount of heat contained in light of different wavelengths. By diffracting light through a prism and placing a thermometer in different regions of the diffracted light. Herschel observed that the greatest increase in temperature was when the thermometer was placed out of the diffracted light on the red side. Nearly 80 years later the bolometer was invented as a way to measure the intensity of infrared radiation. At its simplest a bolometer is a conductor, with a current passing through it, whose resistance depends on its temperature. As infrared emission falls onto the bolometer it is heated and its resistance changes, causing the current flowing through the bolometer to change. This change in current can be calibrated to measure the IR flux on the bolometer. The limiting factors of a bolometer are the cooling time of the bolometer and the background thermal radiation from the detector itself. As IR photons impact the bolometer it will begin to heat up and if this continues then if the detector's resistance is a non linear function of its temperature it will not be able to accurately detect the energy of the incoming IR photons. This is why it is important that bolometers can cool down, this can be accomplished by either designing the bolometer with sufficient cooling or by allowing time for the bolometer to cool down between observing periods. Removing background thermal emission is important to allow detection of faint IR sources. However, unlike an optical telescope, background IR noise can come from the telescope itself. To overcome this issue the telescope and detectors need to be cooled to very low temperatures to detect photons in the FIR. While theoretically bolometers could be used to measure flux at any wavelength they are used almost exclusively for FIR measurements and have been used in the *Herschel* space telescope Pilbratt et al. (2010) and the James Clerk Maxwell Telescope (JCMT).

1.4.2 *Herschel*

The most recent space based FIR telescope was *Herschel* (Pilbratt et al., 2010), which was launched in 2009 and was operational for 4 years. *Herschel* has a primary mirror with a 3.5m diameter and to reduce thermal background noise was placed at the Earth-Sun Lagrangian point 2 (L2) to place it far from the Earth as well as being in the Earth's shadow. In addition, liquid helium was used to cool the instruments, further reducing thermal noise. However, with *Herschel* being located at L2 it was impossible to replace the liquid helium and therefore limited *Herschel's* observing time to 4 years. FIR continuum observations were made by two instruments on board *Herschel*: the Photodetector Array Camera and Spectrometer (PACS Poglitsch et al. (2010)) and the Spectral and Photometric IMaging Reciever (SPIRE Griffin et al. (2010)). PACS observed at 70, 100 and 160μm, making it ideal to measure the peak of the FIR emission for galaxies at $z < 1$, which is typically around 100μm. In contrast SPIRE observed at 250, 350 and 500 μm and therefore better suited for detecting galaxies at higher redshift. SPIRE is able to observe all three bands simultaneously while PACS can only observe in two bands at the same time. The detectors for each of the SPIRE bands are composed of an array of 139, 88 and 43 bolometers arranged in an hexagonal pattern for the 250, 350 and 500μm respectively. Each detector has light directed to it through a feedhorn, which prevents stray light from impacting the detector. The bolometers consist of a silicon nitride absorber and a thermometer of germanium. In addition, each detector is equipped with several dark bolometers to provide some measure of the thermal noise and temperature drift (Valtchanov et al., 2014).

To construct FIR maps the individual datastreams from each bolometer are combined (these datastreams are referred to as timelines). The *Herschel* maps used in this thesis were created with a FWHM of 18.15, 25.15 and 36.3 arcsec and pixels sizes of 6, 10, 14 arcsec for the SPIRE maps at 250, 350 and 500μm respectively. Meanwhile the PACS maps have a FWHM of 5.6, 6.8 and 11.3 arcsec and pixel sizes of 3.2, 3.2 and 6.4 arcsec for observations at 70, 100 and 160μm respectively. Maps from both instruments are affected by instrumental noise, which is mostly Gaussian, and confusion noise. Confusion noise is noise caused by low flux background sources with a high density. While background noise can be reduced by observing the same location for a longer time confusion noise is unaffected Nguyen et al. (2010).

Herschel has observed $\sim$ 1200 square degrees outside of the galactic plane. This data was collected and homogenised as part of the Herschel Extragalactic Legacy Project (HELP) as well as collating multiwavelength catalogues, from the UV to NIR. HELP covers multiple fields of different depths and sizes, with the largest being *Herschel*-stripe82 (which covers $363.4deg^2$) to smaller deeper fields such as SPIRE-NEP ($0.6deg^2$).

1.4.3 FIR source detection

Detecting sources in SPIRE images has a number of additional challenges not present in optical images, for which a large number of source detection algorithms and software exist, such as *SEXTRACTOR* (Bertin, 1996). Simplistically these algorithms typically work by first finding peaks of emission and then assigning any nearby flux to one source. This is not ideal for SPIRE images as the source density per beam is typically much greater than one. This leads to significant source confusion and means that multiple fainter sources would be absorbed by other brighter nearby sources. To counteract these problems a number of algorithms have been developed over the years to detect sources in the images, I will briefly describe some of these here. SUSSEXtractor (Savage and Oliver, 2007) first convolves the map with a filter (either the PSF for shallow images or a filter that is narrower than the beam for deep images). Then peaks are located by comparing each pixel to its neighbours. When a peak is located then the location of the source is found by using the surrounding pixels. Alternatively DESPHOT (Roseboom et al., 2010) works by first knowing the position of sources. This prior based approach models the SPIRE map as a combination of sources convolved with the PSF and background noise. If we know where sources are, either from other multiwavelength catalogues or from other FIR source detection algorithms like SUSSEXtractor we can use DESPHOT to measure the contribution of those sources to the map. This is done by turning on sources one by one and finding the flux for each of those sources that produces the best match to the map. Once the best fit has been achieved then additional sources are added to the prior one by one. To prevent overfitting each additional source turned on adds a penalty to the likelihood of that model. This is implemented using the least absolute and shrinkage and selection method (LASSO).

The most recent source detection method is XID+ (Hurley et al., 2017) and is used extensively in this work. I will describe its algorithm in more detail in Ch 3 as part of my work on the FIRC and again in Ch 4 where I adapt it to run on LOFAR images.

1.5 Radio Observations

As discussed above radio emission can trace SF in galaxies regardless of whether the SF is obscured by dust or not. Therefore radio observations would be ideal for measuring the SFR of galaxies. With radio emission being at even longer wavelengths than the FIR radio telescopes need even larger diameters to achieve comparable resolutions to optical and NIR telescopes. However, unlike FIR radiation radio emission isn't absorbed by the atmosphere so radio telescopes can be built on the ground, allowing for very large telescopes(currently the largest operating single dish radio telescope is the five hundred meter aperture spherical radio telescope FAST in China Li and Pan (2016)). In addition, radio telescopes have a simpler design than modern optical telescopes, instead of a difficult to manufacture mirror that focuses the light onto a CCD camera radio telescopes focus radio emission with a simple metal surface that, at long wavelengths, is not strongly affected by small imperfections. Combined this allows for the construction of very large radio telescopes that can reach arcsecond resolution but a single radio telescope would need a diameter of over 1km to reach sub arcsecond resolution.

However, radio observations have one advantage that other wavelengths do not. By combining observations from multiple telescopes the effective diameter of the telescope becomes the distance between the two individual radio telescopes. With baselines of thousands of kilometers radio telescopes can easily reach sub arcsecond resolutions. The principle behind this technique can be seen when considering a plane wave from a point source. The plane wave will travel a different distance to each of the telescopes and depending on the distance between the telescopes and the frequency observed the two signals will either be in or out of phase. By introducing an artificial delay τ to one of the telescope's signal you can steer the phase center of the intereferometer and by observing the combined signal determine the position of the source with great accuracy (figure 1.4). In addition, typically interferometers are made up of dozens of telescopes, with each pair acting as its own separate baseline that can observe independent of the others. This creates some new problems as each baseline is sensitive to sources of a certain resolution and will not detect large scale structures that are much larger than its resolution. Combining this information from multiple baselines is complex and requires performing an inverse fourier transformation that scales with the number of pixels in the image squared multiplied by the number of baselines. So is computationally difficult. Approximations can be made to

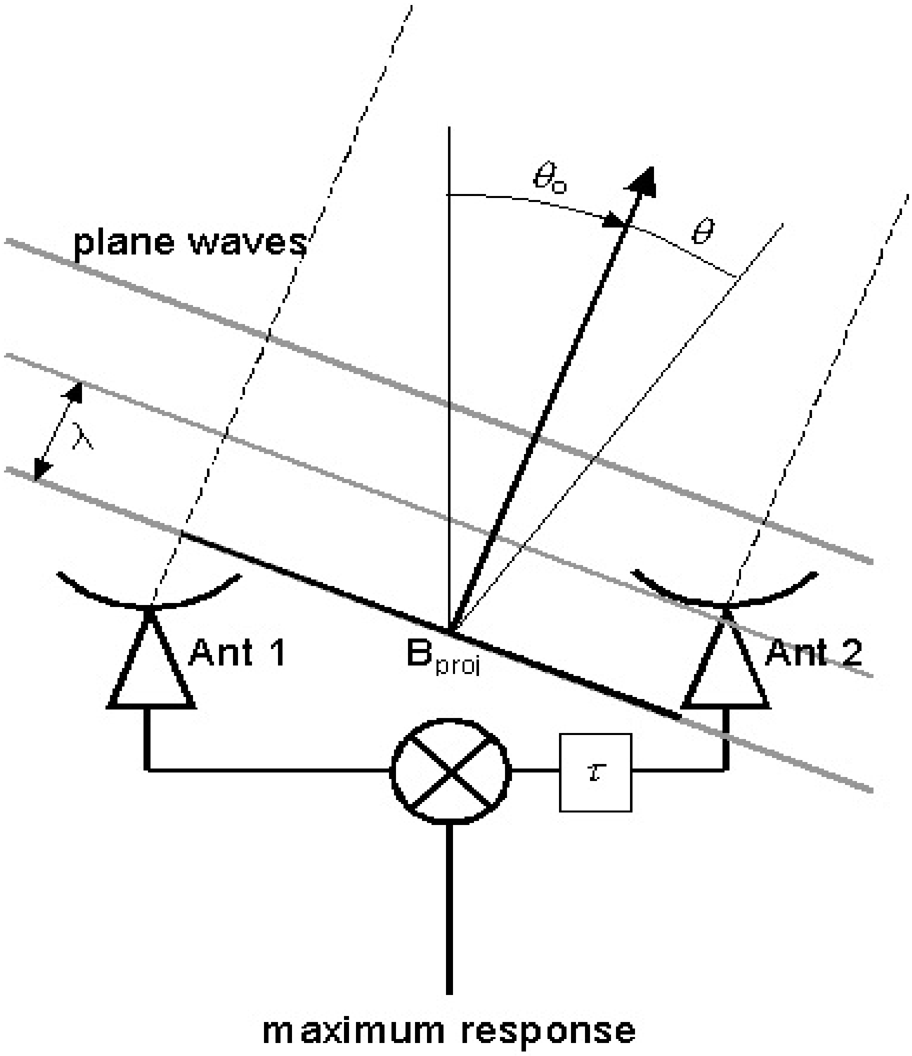

Figure 1.4: Interferometer setup when a delay τ is introduced to one of the antenna to artificially steer the telescope phase centre. Credit: Prof Dale E. Gary at NJIT https://web.njit.edu/ gary/728/Lecture6.html

speed up this process but these introduce errors that need to be accounted for when using the final image for science. For more details on how radio interferometers work see Wilson et al. (1997).

1.6 Summary

In this chapter I presented the main sources of emission that are relevant to this thesis, SF, dust and radio. I also briefly mentioned how AGN can confuse emission from these sources and make determining SFRs difficult. I then described how FIR and radio observations are made and gave a brief description of the *Herschel* space telescope and how sources are detected in its images.

Chapter 2 contains a detailed description of the likelihood ratio technique for cross-matching multiwavlength catalogues. I then present the crossmatching I did in Lockman Hole to match the LOFAR radio catalogue to the multiwavelength catalogue in the field. This work contributed to Kondapally et al. (2021) which presented the optical cross-matches to the LOFAR radio catalogues in *Bootes*, ELAIS-N1 and Lockman Hole.

My paper of the FIRC makes up Chapter 3 which present work I did to measure the FIRC at low frequencies. This work tested whether the FIRC evolves with redshift or stellar mass by constructing multiple mass complete samples.

Chapter 4 presents my current work on expanding the Bayesian flux measurement software XID+ to run on radio images. It contains tests run to compare the results that XID+ obtains compared to those from PyBDSF and how well it recovers the flux of fake injected sources. Finally I present the results when run across the entirety of ELAIS-N1 on a sample of galaxies whose predicted radio flux, from the FIRC, is above the 3σ level.

Chapter 2

Crossmatching

This chapter discusses several different methods of crossmatching including the theoretical underpinnings as well as their relative strengths and weaknesses. The later sections of the chapter present work done as part of Kondapally et al. (2021) to crossmatch the LoTSS deep fields catalog in Lockman-hole to the multiwavelength catalog, created as part of the LoTSS deep field project, using likelihood ratios (LR).

2.1 Likelihood Ratio

The likelihood ratio is used to cross match sources in a more statistically robust method than just using nearest neighbour matching. It works by working out the probability that a nearby source is a true counterpart (based on the sources properties) compared to the probability that it is a nearby, but unrelated, background object. This method can be used to crossmatch optical and NIR surveys Williams et al. (2018) and is of particular use when crossmatching optical catalogs with longer wavelengths catalogs, such as FIR, sub mm and radio (Smith et al., 2011; Fleuren et al., 2012; Mcalpine et al., 2012). The ratio that a given source, from catalogue B, is a true counterpart of an object, from catalogue A, compared to a background object is calculated using the following equation from Sutherland and Saunders (1992)

$$LR = \frac{q(\mathbf{p})f(r)}{n(\mathbf{p})} \tag{2.1}$$

where $f(r)$ is the probability that a given source, from catalogue A and potential counterpart, from catalogue B, will be separated by a distance r. $n(\mathbf{p})$ is the probability that a given source with properties $\mathbf{p}$ is an unrelated background object. Finally $q(\mathbf{p})$ is the probability that a true counterpart will have properties $\mathbf{p}$. Properties $\mathbf{p}$ can be any property of the potential counterpart such as magnitude, colour and source type (eg star, galaxy or AGN).

$n(\mathbf{p})$ is simple to calculate, as it is just the multidimensional distribution of $\mathbf{p}$, which can be measured from the data directly over a large representative area. However, $f(r)$ and $q(\mathbf{p})$ can be more difficult to estimate. To estimate $f(r)$ the positional uncertainties of both the sources and potential counterparts needs to be known. For radio surveys this can be challenging as each radio source can have differing positional uncertainties based on the direction from the source (due to the resolved nature of some radio galaxies). In addition, to the positional uncertainty of a given source there are additional astrometric errors that need to be accounted for.

2.1.1 Estimating q(p)

The final term in the LR is the most complicated to calculate. Ciliegi et al. (2003) estimated $q(\mathbf{p})$ using the following method when $\mathbf{p}$ only contained the magnitude of the galaxy in one band

1. First measure the magnitude distribution of all potential crossmatches from B nearby to the sources from A, $total(m)$. The search radius used can be chosen by the user so that it will incorporate the majority of true counterparts.

2. Subtract the background distribution $n(m)$ from $total(m)$ to get $real(m)$.

3. Normalise $real(m)$ such that $q(m) = \frac{real(m)}{\Sigma real(m_i)} Q_0$ where Q_0 is the fraction of sources in A that have a true crossmatch in B.

Using this method estimating $total(m)$ and $real(m)$ is simple (once the search radius has been chosen). However, estimating Q_0 is still a complicated process. Merely dividing $real(m)$ by the number of sources in catalogue A will tend to overestimate Q_0 due to source clustering and genuine multi-counterparts to sources in catalogue A. To avoid this multicounting problem Fleuren et al. (2012) decided to estimate $1 - Q_0$, the fraction of sources in catalogue A without a counterpart in catalogue B, I will refer to these sources as blanks. Blanks could be sources whose counterpart is fainter than the detection limit of catalogue B or outside of the chosen search radius or they could be spurious sources in catalogue A (i.e the source is actually an artifact and therefore has no counterpart). To calculate the true number of blanks first the number of observed blanks, out to a search radius r, is counted. This then needs to be corrected by the number of sources in catalogue A that have am unrelated source from catalogue B within r, I shall refer to these sources as false matches. To estimate the number of false matches I create N random sources, where N is the number of sources in catalogue A, at random positions and then see how many of them are blanks at radius r. I can then calculate the true number of blanks in catalogue A using equation 2.2

$$\bar{A}_t = \bar{A} + \bar{A}_t \frac{R}{N} \equiv \bar{A}_t = \frac{\bar{A}}{1 - \frac{R}{N}} = \frac{\bar{A}}{\bar{R}/N}, \tag{2.2}$$

where A and R are the number of sources without a counterpart within r from catalogue B, for sources in catalog A and the random sources respectively. A bar refers to the number of blanks instead of matches and $_t$ refers to the true number of blanks as opposed to the observed number. By dividing by N I get $\bar{A}_t/N = \bar{A}/\bar{R}$ which is equivalent to $1 - Q_0$ and $\bar{A}/\bar{R}$ can be easily measured. However, this definition of Q_0 is dependent on the search radius r used and I would prefer to find an independent measure. To find this I start by considering why a true blank could exist. Either its true counterpart lies outside the search radius r or its true counterpart is below the survey's sensitivity. The former probability can be calculated from the positional error distribution $f(r)$ while the latter is $1 - Q_0$. Then, assuming the two probabilities are independent, and using $P(AorB) = P(A) + P(B) - P(AandB)$ I can model the dependence of true blanks on the search radius as

$$(1 - Q_0) + (1 - F(r)) - (1 - Q_0)(1 - F(r)) = 1 - Q_0 F(r) \tag{2.3}$$

$$F(r) = \int_0^r P(r')dr' \tag{2.4}$$

$$P(r) = 2\pi r f(r) \tag{2.5}$$

As long as f(r) is known for your survey you can fit the dependence of the ratio of measured blanks from catalogue A to blanks from random positions on the search radius r to equation 2.3 to find a value of Q_0 that is independent of r.

This method for estimating $q(\mathbf{p})$ is accurate when $\mathbf{p}$ only contains the magnitude of the counterparts. However, if the colour of a counterpart is included in $\mathbf{p}$ then a modification to this method is needed. Firstly Q_0 becomes colour dependent $Q_0(c)$ where c is the colour of the counterpart. I cannot simply estimate $Q_0(c)$ by dividing the counterparts into colour bins and then estimating the number of blanks solely based on counterparts in these colour bins. This is due to the clustering of counterparts (whether galaxies or stars). Imagine a scenario where the true counterpart (in colour bin c_1) has a physically associated galaxy (this could be a result of galaxy clustering) in a separate colour bin (c_2) both within search radius r. Those two galaxies will both contribute to the $Q_0(c)$

in both colour bins as there is a physical association between all three galaxies in a way that comparing to random positions will not correct for. Instead an iterative approach was developed by Nisbet (2018) to calculate $Q_0(c)$ and $q(\mathbf{p})$ when $\mathbf{p}$ contains a source's colour. This approach is summarised below

1. To begin a first pass of crossmatches is chosen. This first set of matches could be as simple as a nearest neighbour crossmatch. However, the better the first set of matches the fewer iterations are needed to converge on a set of best crossmatches.

2. The initial set of crossmatches is used to measure $Q_0(c)$ with the sources being divided into appropriate colour bins. Then $q(\mathbf{p})$ is calculated using the new $Q_0(c)$ and dividing the set of crossmatches into appropriate colour and magnitude bins.

3. Then, using the new $q(\mathbf{p})$ LR are measured for all potential crossmatches, usually taken as all sources within some search radius.

4. These LR are used to select new crossmatches. These matches are used to remeasure $Q_0(c)$ and the steps are repeated until the matches don't change.

2.1.2 Selecting LR threshold

Once the LR of all potential counterparts has been measured you would be forgiven for thinking that you simply select the highest LR match for every source. However, some best crossmatches will have a LR much less than one while some can be much greater than one. This is because the LR is not normalised so does not represent a true probability and instead just expresses the relative likelihood of a crossmatch compared to another. These two different cases should not be considered equally. Especially considered that if $Q_0 < 1$ I expect that not all the sources in our catalogue will have a crossmatch. So I need to determine a threshold which a LR must be above to be considered a true crossmatch. The simplest method would be to select the $Q_0 * 100$ percentile of the LR distribution and set this as the threshold. However this depends on the measure of Q_0 being accurate, which may not always be true. Using the method outlined above requires an accurate measure of f(r). Normally f(r) is assumed to be Gaussian however, there are normally small deviations from this that can cause Q_0 to be slightly off. It should be noted that this inaccuracy will only affect the ordering of the LR for a given source's potential crossmatches for a small number of sources. Alternatively, Best et al. (2003) compute the reliability and completeness of the crossmatches for a given threshold T using the following equations

$$Completeness(T) = 1 - \frac{1}{Q_0 N} \sum_{LR_i < T} \frac{Q_0 LR_i}{Q_0 LR_i + (1 - Q_0)} \tag{2.6}$$

$$Reliability(T) = 1 - \frac{1}{Q_0 N} \sum_{LR_i < T} \frac{1 - Q_0}{Q_0 LR_i + (1 - Q_0)} \tag{2.7}$$

where N is the number of sources being crossmatched. Using these measures for completeness and reliability you can use whatever criteria you deem suitable to select an appropriate threshold.

2.2 Lockman Hole datasets

Here I detail the crossmatching procedure used to match the multiwavelength catalogue from Kondapally et al. (2021) to the LOFAR source catalogue in Lockman Hole. Lockman Hole is area of the sky, approximately 15deg^2, first discovered by Jay Lockman. Located at RA 15h 45m and Dec +58^o Lockman Hole is a region of extragalactic sky (not along the galactic plane) that is relatively free of neutral hydrogen. This enables easier detection of UV as there is less absorption by the neutral hydrogen at 121.6nm. First I will describe the observations and instruments used for the multiwavelength and radio catalogue as well as the procedure used to create the catalogues. Finally I will describe how the LR technique was applied to the LOFAR datasets.

2.2.1 Multiwavelength Catalogue

In Lockman Hole (LH) there are multiple UV, optical and NIR surveys that cover different regions of LH. To create a uniform multiwavelength catalogue that is suitable for SED fitting and covers a wide range of wavelengths several surveys were combined. Optical data comes from two main surveys: the *Spitzer* Adaption of the Red-sequence Cluster Survey (SpARCS; Wilson et al. (1997); Muzzin et al. (2009)) and the Red Cluster Sequence Lensing Survey (RCSLens; Hildebrandt et al. (2016)), both of which were taken using the MegaCam instrument on the Canadian France Hawaii Telescope (CFHT). SPARCS observed in the broadband u, g, r, z bands while RCSLens observed in the g, r, i, z bands with the former observing 13.3deg^2 and the latter observing 16deg^2. However, the coverage of RCSLens is not contiguous in all bands.

UV data was taken from the DR6 and DR7 of the Deep Imaging Survey (DIS) taken with the Galaxy Evolution Explorer (GALEX) space telescope (Martin et al., 2005; Morrissey et al., 2007). Observations from GALEX cover the Near UV (NUV) and Far UV (FUV) which cover the wavelength range $135 - 280nm$.

NIR data in the J and K band was taken from the UK Infrared Deep Sky Survey (UKIDSS) Deep Extragalactic Survey (DXS) DR10 (Lawrence et al., 2007). The observations were made using the WFCAM instrument (Casali et al., 2007) on the UK Infrared Telescope (UKIRT) in Hawaii. The photometric system is described in Hewett et al. (2006).

Finally data in the MIR at 3.6, 4.5, 5.8 and 8.0μm were taken from the IRAC instrument (Fazio et al., 2004) on board the *Spitzer* space telescope (Werner, 2004). There are two *Spitzer* surveys that cover part of LH: the SWIRE survey (Lonsdale et al., 2003) and the *Spitzer* Extragalactic Representative Volume Survey (SERVS; Mauduit et al. (2012)). The SWIRE survey covers $\approx 11\mathrm{deg}^2$ in all four MIR bands while SERVS only covers half the area and in the two shorter bands, though SERVS does reach a greater depth than SWIRE.

In order to have a uniform wavelength coverage across the entire multiwavelength catalogue only the overlapping region of the SPARCS r-band and the SWIRE survey was used in LH (giving an area of $10.73deg^2$).

Rather than merge the individual catalogs from each survey it was decided to create new forced photometry catalogues from χ^2 images (Szalay et al., 1999). χ^2 images are created by combining images from multiple bands. This combines the signal from multiple bands allowing the detection of galaxies whose signal in individual bands isn't above 5σ but when combined will be. This is done by computing the standard χ^2 statistic for each pixel after the images have been added together. These χ^2 images were created using SWARP (Bertin et al., 2002), which works by creating a combined error weighted image from the images in the individual bands. To do this the individual images are regridded to the same pixel scale (a scale of 0.2" was used). Using a χ^2 image avoids the complications that can arise from catalogue merging procedures, such as source mismatching or difficulties in matching catalogues of different resolutions. The other advantage of a uniform forced photometry catalogue is for photometric redshift measurements and SED fitting. If sources were undetected in multiple bands then when SED fitting these bands can either be treated as a non detection, and therefore not used for fitting to that galaxy, or treated as a upper limit. Both options lead to a loss of information that can affect photometric redshift measurements and SED fitting. Finally each catalogue will have its own procedure for flux measurements and aperture corrections. This inhomogeneity can also lead to inaccurate colours. These problems can be overcome by performing source detection on χ^2 images constructed from a series of pixel matched images and then measuring fluxes from forced apertures.

The details of this procedure are described in full in Kondapally et al. (2021) and I summarise the relevant points here. The pixel matched images are created with a pixel scale of 0.2" with no attempt at PSF homogenisation. Source detection was carried out using SEXTRACTOR Bertin (1996) on two χ^2 images, one constructed from the 3.6 and 4.5μm bands and the other from the SPARCS-ugrz, RCSLens-i and UKIDSS-DXS-JK bands. Two images were created, rather than combining all the bands from the optical to IR into one image, as the difference in resolution between the optical and IRAC bands is very large. Matching these bands into one image would end up losing information from the the shortest or longest wavelengths as the image are pixel matched. In addition galaxies that are bright in the NIR may be undetected at optical wavelengths and vice versa, making it worthwhile to identify galaxies in each seperately. Once sources were identified in each image then forced aperture measurements were taken with apertures of $1-7$" (in 1" steps) and 10" in the bands that make up each respective χ^2 image, giving two separate catalogues, one in the optical to NIR and the other in the MIR. Aperture corrections were calculated using the curve of growth estimated from the aperture fluxes and assuming that all the flux was detected in the largest aperture. These two catalogues were then merged using a nearest neighbour crossmatch with a search radius of 1.5" and any *Spitzer* source without a counterpart within this search radius is classified as a *Spitzer* only source.

2.2.2 LOFAR data

The LOw Frequency ARrray (LOFAR) is a radio telescope based in Europe and designed and constructed by ASTRON designed to operate at 10-240MHz (30-1.2m). LOFAR is made up of multiple observing stations spread across Europe with the majority in the Netherlands (38 stations) making up the short baselines and other stations in Germany (six stations), Poland (three stations), France, Ireland, Latvia, Sweden, and the United Kingdom (one station each). Each station consists of a interferometric array of dipole antennae that are capable of observing the entire sky giving LOFAR a wide field of view (FOV) $7-8deg$. The signals from each dipole are combined in each station into a phased array and these arrays can then be combined. The large FOV combined with the ability to observe multiple parts of the sky simultaneously makes LOFAR an excellent telescope for surveys. LOFAR generates $\approx 13T\text{bits}s^{-1}$ across all stations. This is a huge amount of data to process let alone transport to the central processing centre in Groningen. The majority of this data is signal from the entire sky and the majority of this data is thrown away and all that is kept is the signal from near the phase center. The technological challenges that LOFAR needs to overcome is part of its role as a pathfinder for the Square Kilometer Array (SKA). A more detailed description of the LOFAR array and the computing infrastructure used to support it can be found in Van Haarlem et al. (2013).

A typical 8 hour LOFAR observation with the High-Band antennae (HBA) will have a depth of 0.1mJy with the resolution depending on the configuration used, though only one configuration is used for the observations used in this work (it is worth noting that LOFAR has the potential for very long baseline intereferometry, VLBI, which is not used in this thesis). However, these low frequency observations have a number of problems that need to be overcome to reach this depth that are not encountered at GHz frequencies. Firstly the Ionosphere distorts radio emission that passes through it, causing a direction dependent (DD) phase delay that affects each station differently. In addition because of the large field of view (FOV) the visibilties from each station also suffer from these DD phase delays. The second problem is caused by the Ionosphere varying with time, causing the visibilities to vary with time due to this variation as well as observing different parts of the sky as the earth rotates. All of these effects need to be properly accounted for to properly model the night sky and produce radio images that are of scientific quality. Higher frequency observations are less effected by ionosphere distortions and can be safely ignored. In addition, the design of GHz radio telescopes have a smaller FOV so any ionosphere distortions have less variability across the image. You can see from Figure 2.1 that the dirty beam has significant side lobes that can extend for arcminutes to degrees (depending on the configuration used for the observations). So if I only applied traditional radio calibration techniques, that do not account for DD Ionosphere effects, there would be significant artifacts in the LOFAR images from bright sources. These artifacts can significantly raise the rms of the image and highlight the importance of accounting for DD effects.

Accounting for the DD effects is a complex process which required the development of a new direction dependent facet calibration in order to generate radio images from LOFAR HBA data. This calibration method was developed by van Weeren et al. (2016) and then later streamlined by Tasse et al. (2018). I briefly summarise the calibration method here

1. First observations of calibrator sources are made before and after the observing

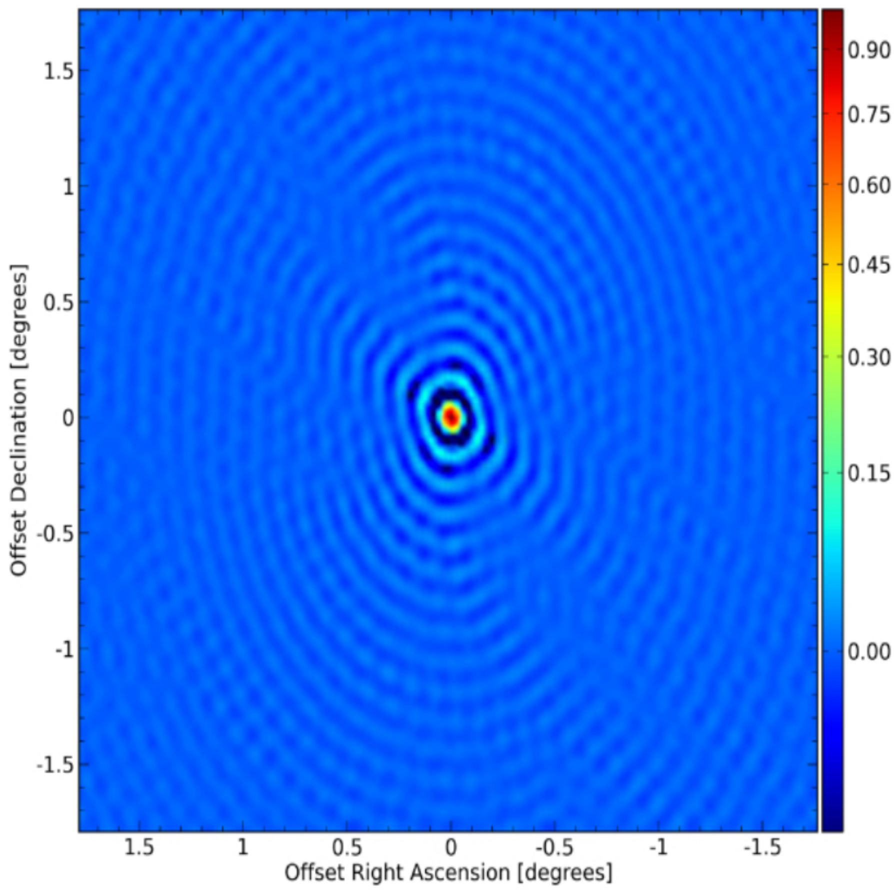

Figure 2.1: The theoretical synthesised beam based on the position of the 24 core LOFAR stations. Credit: Van Haarlem et al. (2013)

period so that any slow varying effects, such as the ionosphere varying with Earth's night-day cycle, can be accounted for.

2. The image is divided up into facets with each facet being centered on a bright calibrator source

3. Then for each facet the sources from all other facets are removed from the image and the facet is calibrated using the central bright source, whose shape and brightness are already well established from previous observations, to measure the direction dependent effects.

4. The direction dependent correction are applied across the entire facet and then the facet is imaged.

The LOFAR data used in this work is collected from the High-Band antennae (HBA) in Lockman Hole in the frequency range 120.2-168.9MHz. There were 12 pointings of 8 hours centered on 161.75deg and 58.083deg (ra, dec) giving a total integration time of

$\approx$ 100 hours. The images were reduced by first creating a DD+DI self calibrated sky model from one 8 hour pointing and this model was then used to calibrate the remaining pointings.

The noise of these images was estimated by taking the minimum flux of multiple cutouts, with varying sizes, with random position across the image. As the noise in the image should be normally distributed it can be shown that there is a relation between the distribution of minimum values drawn from the randomly placed cutouts and the standard deviation of the image, see Tasse et al. (2021). In principle a similar relation exists for any similar property of the cutout such as the median or max. However, the image is made up of contributions from the noise, artifacts from image calibration and genuine sources. I want our estimate of the noise to contain information on the noise and artifacts only so the minimum is used to estimate the noise as sources will affect the upper end of the flux distribution in the cutouts. This methods gives an average rms of $\approx 23\mu Jy\ beam^{-1}$.

Source extraction was done on this image by using the Python Blob Detector and Source Finder (PyBDSF; Mohan and Rafferty (2015)) which has the advantage of estimating the noise locally rather than on the whole image. This is needed because the noise in the image varies depending on the distance to the centre of the pointing as well as the proximity of other bright sources. PyBDSF does this by using a sliding box of size 40x40 beam widths, except around bright source where the box is decreased to 15x15 beams so that the increased noise in these regions is correctly measured. PyBDSF then looks for peaks of emission that are greater than 5σ and fits the observed emission with a Gaussian whose major and minor axis and orientation can vary. In addition, PyBDSF will fit multiple Gaussians if required to fit the emission. Then these Gaussians are potentially grouped into one source depending on whether they are sufficiently separated by distance or by pixels containing no significant emission.

2.3 Applying the LR method

Here I explain how the LR method was applied to the LOFAR radio catalogue to cross-match it with the multiwavelength catalogue in Lockman Hole. The LR method is unsuitable for large complex radio sources or radio sources with multiple components, such as radio AGN with jets. Therefore to select radio sources suitable for the LR I restrict our radio catalogue to sources whose major axis is less than 10". The LR was computed using magnitudes in the r-band and at 4.5μm as well as the $r - 4.5$ colour. In this application of the LR method both $n(\mathbf{p})$ and $q(\mathbf{p})$ becomes $n(m, c)$ and $q(m, c)$ respectively (we also need to compute $n(m)$ and $q(m)$ to create initial matches as is described below). Here I will explain how the three terms in the equation 2.1 are computed.

2.3.1 Estimating f(r)

$f(r)$ is the probability that a counterpart of the radio source has some separation r. Strictly speaking this probability is also dependent on the uncertainty of the separation, making it $f(r, \sigma)$. Here σ is dependent on several factors: The uncertainty of the radio source position along the direction between the radio source and counterpart, the positional uncertainty of the counterpart and the uncertainty from any astrometry errors between the two surveys. The error along the direction between the radio source and counterpart is important to calculate because of the asymmetric nature of radio sources, caused by extended emission and non symmetric beams.

We use the following equation to estimate $f(r)$ for each potential radio crossmatch pair

$$f(r) = \frac{1}{2\pi\sigma_{min}\sigma_{maj}} \exp\left(\frac{-r^2}{2\sigma_{dir}^2}\right) \tag{2.8}$$

r is the offset between the source and counterpart while σ_{maj} and σ_{min} are the positional uncertainties of the radio source along its major and minor axis respectively. σ_{dir} is the combined positional error of the source and counterpart along the direction between them. The error in the direction between the radio source and its counterpart is a combination of three separate sources of error, that need to be added in quadrature. Firstly I need the positional error of the radio source along the major and minor axis. Each PyBDSF source has a measure of the FWHM of the major and minor axis as well as the position angle. Using the relation between the FWHM and the error from Condon (1997) I calculate the error on the major/minor axis as $\sigma = \delta_{FWHM}/(8ln2)^{1/2}$. However, this formula does not account for correlated noise in the image and assumes that the source has a high SNR. To account for this I use the results from Condon (1997) and Röttgering and Bremer (1997) for the NRAO VLA Sky Survey and the Westerbork Northern Sky Survey respectively where they found a factor of $1.3 \approx 1.5$ difference between the theoretical and measured uncertainty. Here I used a factor of $\sqrt{2}$. Secondly there is the positional uncertainty of the potential counterpart. This is taken as 0.35" (Williams et al., 2018; Kondapally et al., 2021) and is usually negligible compared to the positional uncertainty of the radio source. Finally the astrometric error between the two surveys is needed. This is estimated using the method of Nisbet (2018). In short they looked at the distribution of the separation of the radio galaxies in ELAIS-N1 from its most likely i-band counterpart. By fitting a Gaussian to this distribution they were able to measure a mean offset of 0.38” caused by astrometry errors. However, when this value was used for their crossmatching they found that incorrect matches were found for some of the brightest radio sources. These sources, due to their high brightness, had very low positional uncertainties. Which in turn causes their $f(r)$ term to shrink rapidly as r increased. This causes the LR method to prefer closer counterparts for these bright radio sources that upon visual inspection clearly had different counterparts. They tried increasing the astrometric error until visual inspection showed that the majority of these bright sources now had the correct counterpart. This astrometric error was found to be 0.6”. By adding these three errors together in quadrature I can estimate σ_{dir} for all potential crossmatches.

2.3.2 Estimating n(m) and n(m,c)

$n(m)$ (and by extension $n(m,c)$) is the probability that a potential counterpart, with magnitude m and colour c, is an unrelated background and is normalised per unit area. This is easy to estimate simply by measuring the magnitude distribution of all the optical sources in the multiwavelength catalogue in a representative area. I did not calculate $n(m)$ across the full multiwavelength catalogue so that our distribution is not affected by edge effects. In addition the magnitude distribution is smoothed with a Gaussian kernel with width 0.5mag. This was done to smooth the distribution at high and low magnitudes where binning can result in sharp changes in $n(m)$ that can bias the LR of these sources. $n(m,c)$ was calculated by dividing sources into colour bins and measuring the magnitude distribution within each bin, using the same Gaussian kernal to smooth the distribution.

2.3.3 Estimating q(m) and q(m,c)

Both $q(m)$ and $q(m,c)$ are the probability that a source with given magnitude and colour is a genuine counterpart. As discussed in Section 2.1.1 estimating $q(m,c)$ requires a first pass set of crossmatches. While I could have used a simple nearest neighbour crossmatch for this first pass I instead opted to use the results of a magnitude only crossmatch as this reduces the number of iterations needed to converge the colour and magnitude crossmatch.

Estimating $q(m)$ initially requires a measure of Q_0 (the fraction of radio sources with a true counterpart) where I used the method from Fleuren et al. (2012) to measure Q_0 in the r-band and at 4.5μm. Firstly we will search around all radio sources whose major axis is less than 10” within a representative area of Lockman Hole (this is a large rectangular

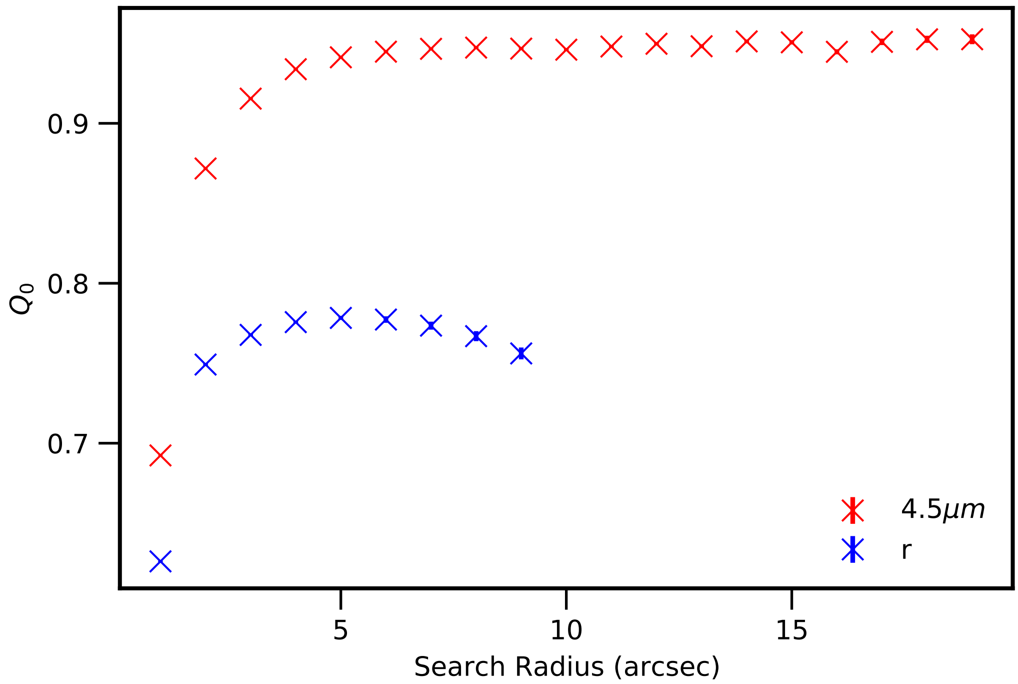

Figure 2.2: Estimate of Q_0 in the r-band and at 4.5μm depending on the search radius around the radio and random sources.

area in the centre of Lockman Hole). The search radius started at 1" and was increased in increments of one arcsecond and the number of sources with an optical/MIR source (depending on the band being examined) within the search radius counted. This is used to measure the number of real blanks (see equ 2.2). The limit on size (major axis less than 10") was introduced to avoid biasing our measure of the number of real blanks by included large extended sources whose true counterpart may be from the automatically measured radio position, which can be inaccurate for radio AGN. Similarly we used a representative area in Lockman hole to avoid overestimating the number of real blanks by avoiding the edge of the optical/MIR images, where the sources density is lower due to edge effects. This process was repeated with a number of fake sources, equal to the number of real sources used, at random positions within the same representative area. This gives us the number of random blanks (see equ 2.2). From this we are able to measure Q_0 for each of our search radii using equation 2.2. I then took Q_0 to be the average Q_0 between 3-6" search radius (Figure 2.2) as the final search radius that would be used was 10" and I want to ensure that our estimate of Q_0 is unbiased by low values for smaller search radii. I found Q_0 to be 0.78 and 0.95 for the r-band and 4.5μm respectively. With Q_0 measured I was able to compute $q(m)$ in both bands and then smooth it with a Gaussian kernal with width 0.5mag (see figure 2.3). This smoothing was done to ensure that LR for bright or faint sources were not unstable and ensure that the interpolation, for an individual sources magnitude, did not change drastically for small changes in magnitude. The LR for each source was calculated in the r-band and at 4.5μm and then compared to the LR threshold to determine whether the source was a crossmatch. The threshold was taken as the $Q_0 * 100$ percentile of the LRs in each band. If a source had more than one crossmatch, whose LR was above the threshold, then its counterpart was taken to be the match with the highest LR in either band. This gave us the first pass crossmatches that could be fed into the estimation of $q(m, c)$.

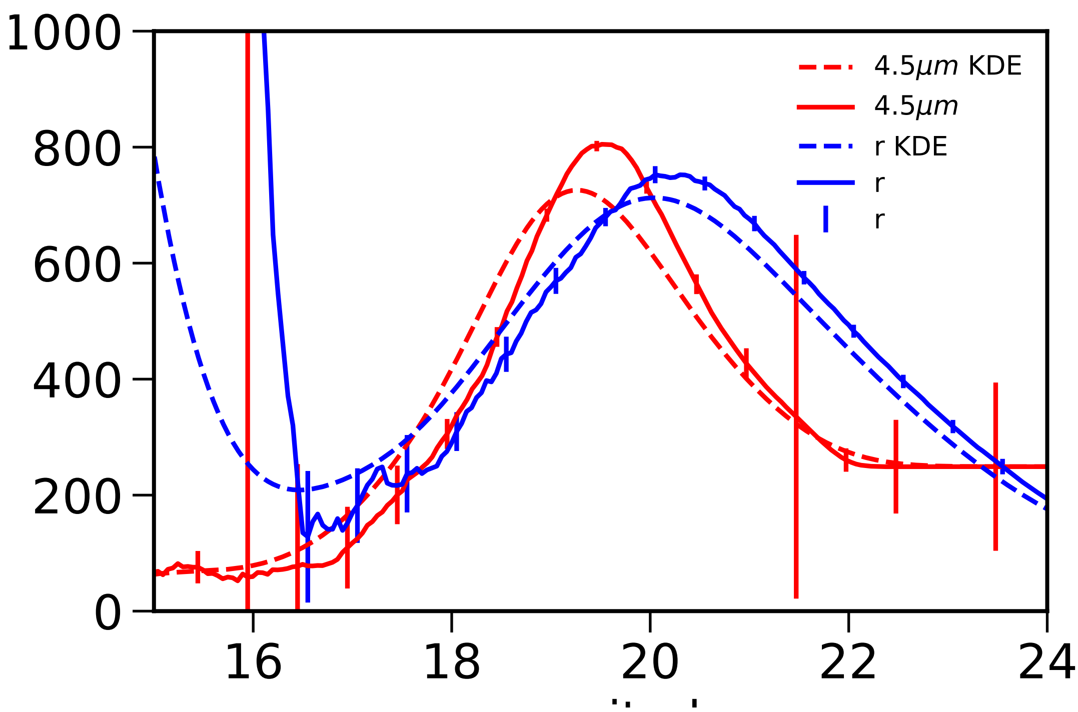

Figure 2.3: q(m)/n(m) for the r-band and 4.5μm in Lockman Hole. The solid lines is when n(m) and q(m) were measured using a cumulative distribution and the dashed line is when the magnitude distribution was first smoothed with a Gaussian kernel with width 0.5mag.

These first pass crossmatches were divided into colour bins of width 0.25mag (r-4.5) to provide an initial estimate of $Q_0(c)$ which is calculated as the number of sources in the colour bin divided by the total number of sources. In addition to these colour bins there were three additional bins for sources that were only detected in the r-band or at 4.5μm or in neither with $S/N > 3$. This final catagory is needed because of the nature of χ^2 image detection method which can result in sources being low S/N in the r-band

Colour bin	$Q_0(c)$	N
c ≤ -0.5	0.0013	34
$-0.5 \leq$ c ≤ -0.25	0.0012	33
$-0.25 \leq$ c ≤ 0.0	0.0041	111
$0.0 \leq$ c ≤ 0.25	0.0086	231
$0.25 \leq$ c ≤ 0.5	0.0154	415
$0.5 \leq$ c ≤ 0.75	0.022	594
$0.75 \leq$ c ≤ 1.0	0.0302	813
$1.0 \leq$ c ≤ 1.25	0.0393	1058
$1.25 \leq$ c ≤ 1.5	0.044	1186
$1.5 \leq$ c ≤ 1.75	0.0457	1231
$2.0 \leq$ c ≤ 2.25	0.045	1212
$1.75 \leq$ c ≤ 2.0	0.0491	1323
$2.25 \leq$ c ≤ 2.5	0.0486	1311
$2.5 \leq$ c ≤ 2.75	0.0481	1297
$2.75 \leq$ c ≤ 3.0	0.0498	1343
$3.0 \leq$ c ≤ 3.25	0.0484	1304
$3.25 \leq$ c ≤ 3.5	0.0493	1329
$3.5 \leq$ c ≤ 3.75	0.0496	1336
$3.75 \leq$ c ≤ 4.0	0.0463	1248
$4.0 \leq$ c	0.1359	3661
Optical-only	0.0068	182
4.5-only	0.1771	4773
No-magnitude	0.0061	166

Table 2.1: $Q_0(c)$ values in each r-4.5μm bin as well as the number of sources in each bin.

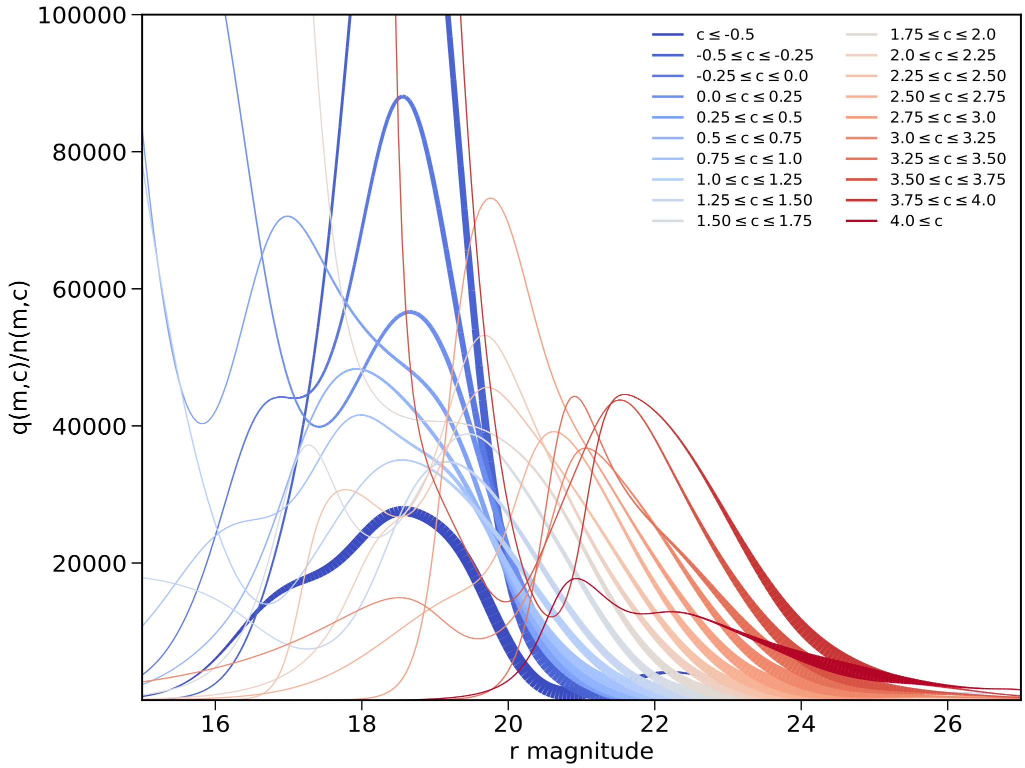

Figure 2.4: q(m,c)/n(m,c) distribution in Lockman Hole across all colour bins (r-4.5μm). The ratio was smoothed with a Gaussian kernal with width 0.5mag and the thickness of the lines show the number of galaxies within that magnitude bin.

and at 4.5μm but bright in other bands. From here calculating $q(m, c)$ is merely a case of following the methodology outlined in Section 2.1.1, which are again smoothed with a Gaussian kernal with width 0.5mag (Figure 2.4). In addition, a minimum value of $Q_0(c)$ was set at 0.001 in each bin. Table 2.3.3 shows the $Q_0(c)$ values, as well as the number of sources in each r-4.5μm colour bin. This prevents a negative feedback loop where low $Q_0(c)$ values, in low population colour bins, cause low $q(m, c)$ values, which in turn cause sources in these colour bins to not be selected as crossmatches. This again drives down $Q_0(c)$ in those bins, making $q(m, c)$ even lower and so on. LR were then measured for all potential counterparts within 10" and were considered potential real crossmatches if their LR was above the threshold where the completeness and reliability crossover (Figure 2.5). The iterative process to estimate $q(m, c)$ was repeated five times and then there were no changes in each source's best crossmatch.

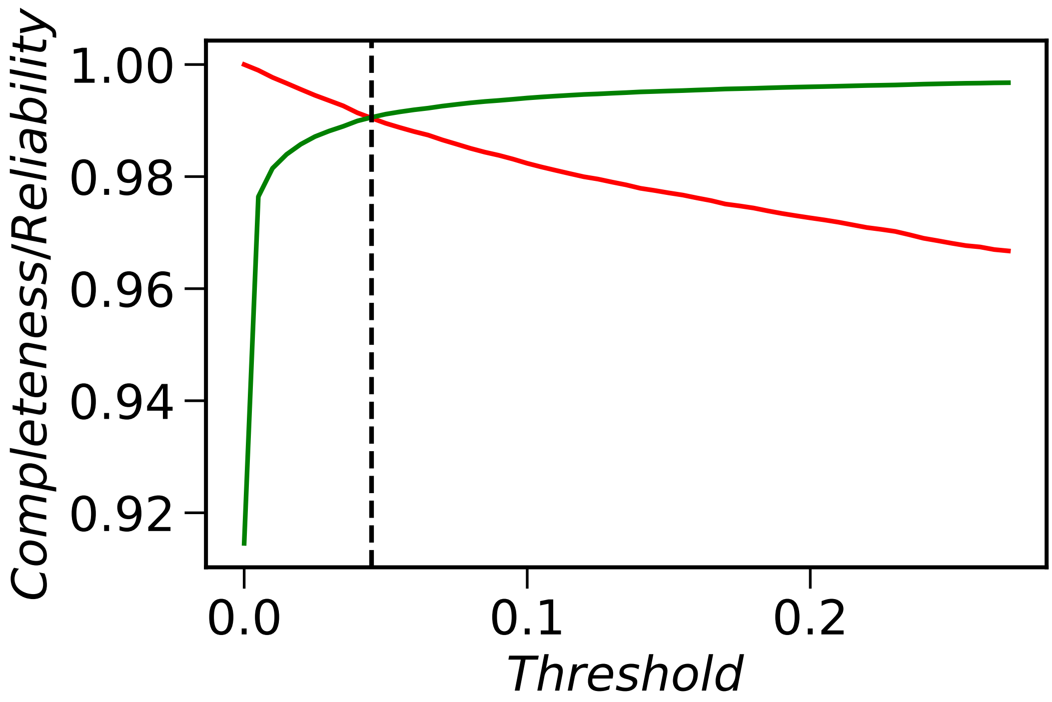

Figure 2.5: Completeness and reliability curves used to calculate the LR threshold, above which a match can be considered genuine. This threshold is taken as the crossover point between the completeness and reliability and is marked by a dotted black line.

2.3.4 Unsuitable Sources

Once the LR was run I am then better able to determine which sources I could trust the LR identification. Along with the limit on major axis the two other criteria considered were whether the radio source was composed of multiple Gaussians and whether the source was clustered. Clustered sources were excluded unless the source was very compact (very point source like) and had a LR identified crossmatch with a high LR. Sources made up of multiple Gaussians had the individual components crossmatched using the LR method and if the components agreed on the counterpart then the LR crossmatch was taken. Additionally if the combined source had a high LR then its LR crossmatch was trusted. Sources whose LR crossmatch was not trusted I sent to the LOFAR galaxy zoo (LGZ). More details on this can be found in Kondapally et al. (2021).

2.3.5 LR Results and Interpretation

In total 79.7% of radio sources had a crossmatch from the LR ratio. From Figure 2.4 I can see that the LR is preferentially selecting faint red galaxies or, relatively bright, blue sources as counterparts. This would agree with our expectations for radio galaxy optical properties as these galaxies are either likely to be AGN (redder and more likely at higher redshift, such as $z > 1$) or star forming galaxies (bluer). If we look at the radio properties of the crossmatched galaxies we can see further evidence for this view. Figure 2.6 shows that galaxies with a higher L_{150} are predominately crossmatched with redder galaxies. These galaxies are likely AGN hosts due to their relatively high mid IR emission that is typically produced by the dusty torus surrounding the SMBH. This matches expectations that AGN make up the majority of high radio luminosity galaxies as was found by comparing the luminosity function for AGN and SF galaxies (Sabater et al., 2020). We also observe that redder galaxies are more likely to be crossmatched to radio galaxies at higher redshift. At z=1 the faintest galaxy that LOFAR can detect in LH has a luminosity of $10^{23.8}$W. Galaxies this bright are likely to be hosting AGN, which would explain the fact that redder galaxies are observed at higher redshift (see fig 2.7).

These results are further supported by the results from the SIMBA simulation (Thomas et al., 2021) which predict that the high end of the radio luminosity function is dominated by AGN at z<2. Additional, the Tiered Radio Extragalactic Continuum Simulation (T-RECS) found similar results (Bonaldi et al., 2019) with both agreeing that the crossover, where SF galaxies are more numerous then AGN, occurs at $\simeq 10^{22.5}$W Hz^{-1} at 1.4GHz ($\approx 10^{23.2}$W at 150MHz with a spectral index of -0.6). This crossover point increases at higher redshifts, increasing to 10^{23}W at z=1. This could explain the flattening in colour we see at high and low luminosities as our galaxy population becomes dominated by AGN at high luminosities and SF galaxies at low luminosities. The change over between these two regimes occurs between 10^{23}W and 10^{24}W, which covers the crossover between the AGN and SF dominated regions in the radio luminosity function according to both the SIMBA and T-RECS simulations.

In conclusion, we can see that adding colour into the LR allows for a more accurate crossmatching process. The agreement between the colour of our crossmatches and the results from simulations supports this. In the future additional colours could be added into the LR method to help identify galaxies that are radio galaxies but whose host properties aren't captured by the bands used in this work. In addition with the advent of large scale spectroscopic surveys such as the Wide Area Vista Extragalactic Survey (WAVES) spectral line intensities and ratios could also be included with this methodology to better identify radio counterparts.

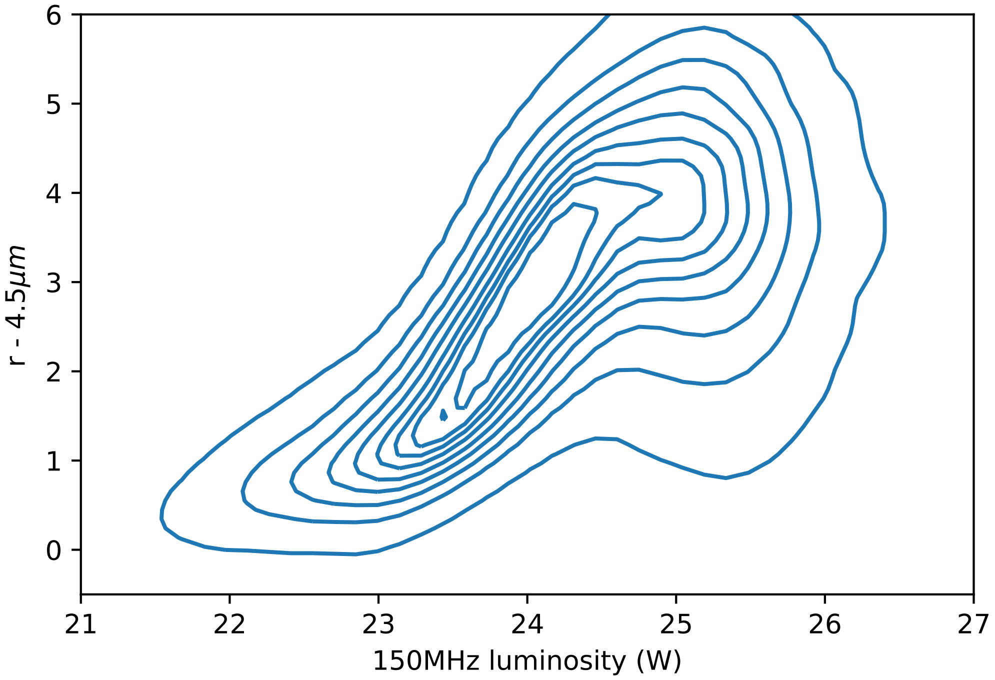

Figure 2.6: Distribution of radio galaxies counterparts in the luminosity r-4.5μm plane smoothed with a Gaussian kernel

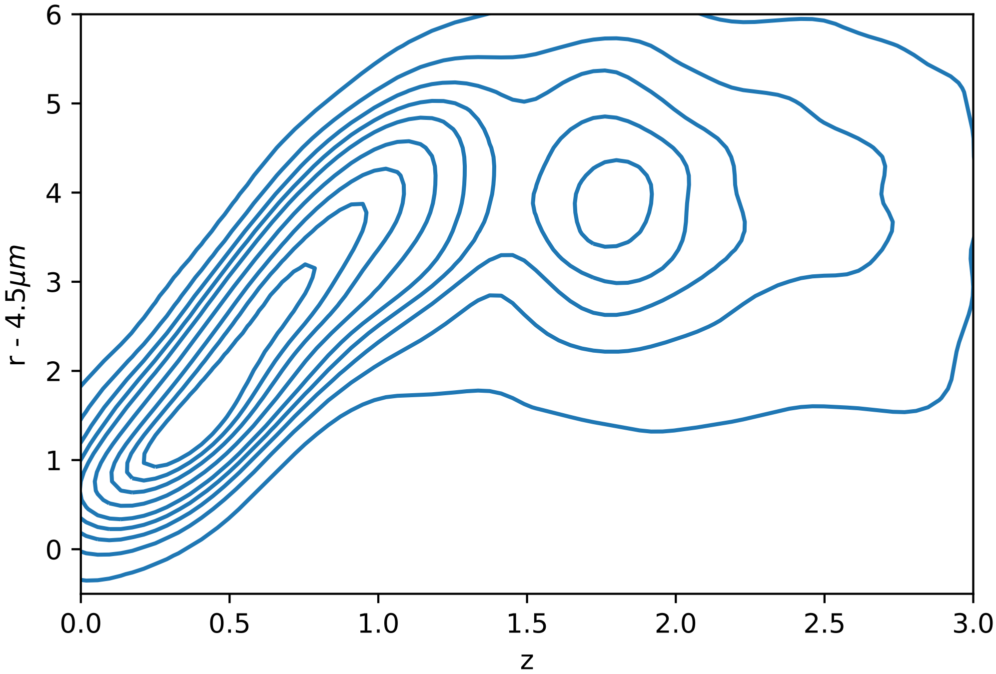

Figure 2.7: Distribution of radio galaxies counterparts in the redshift r-4.5μm smoothed with a Gaussian kernel

Chapter 3

Mass dependence of the FIRC at 150MHz

This chapter contains the paper I submitted to Astronomy and Astrophysics on the mass dependence of the far infrared radio correlation at 150MHz. I have excluded the acknowledgements and included the appendices at the end of the chapter. Some changes have been made to the paper to better fit the thesis format

3.1 Introduction

It has long been known that radio emission from normal galaxies is mostly from synchrotron radiation produced by electrons in the interstellar medium (ISM) that are accelerated by supernovae remnants (Condon, 1992). Emission in the infrared (IR) is produced by dust heated by ultra-violet (UV) and optical radiation, which is then re-emitted in the IR (Casey et al., 2014). As both supernovae and UV radiation are produced by massive stars with short lifetimes, they are both tracers of recent star formation (SF). This provides the theoretical underpinning of the well-known far-infrared radio correlation (FIRC) which was first observed by van der Kruit (1971) and later by Condon (1992),Helou and Bicay (2002),Yun et al. (2002), who found a tight correlation between radio and total infrared (TIR $8 - 1000\mu$m) luminosity in local galaxies. Since then, the FIRC has been observed across a wide range of luminosities and redshifts (Murphy, 2009; Sargent et al., 2010; Delhaize et al., 2017; Calistro Rivera et al., 2017). This relatively tight correlation has been used as a boundary to identify radio-loud active galactic nuclei (AGN; Del Moro et al. (2013); Calistro Rivera et al. (2017)) and as a tool to calibrate the star formation rate (SFR)–radio luminosity relation (Davies et al., 2017; Gurkan et al., 2018). Radio surveys can play a unique role in studying SF in galaxies as they are not affected by dust extinction, and can cover very wide areas of the sky with high angular resolution. A well calibrated SFR–radio luminosity relation is therefore of vital importance for full exploitation of the next-generation surveys with Square Kilometre Array (SKA) precursors (ASKAP and MeerKAT), as well as for the LOFAR all-Sky Survey (LoTSS; Shimwell et al. (2019)), whose second data release will cover several thousand square degrees. Understanding whether the FIRC varies with the properties of galaxies, such as redshift or stellar mass, can provide useful insight for creating a SFR–radio luminosity relation.

The FIRC is thought to originate from SF and is broadly explained by the 'calorimeter' theory developed by Voelk (1989), which proposes that cosmic rays (CRs) accelerated by supernovae shocks lose all or most of their energy as synchrotron emission while they spiral in the galactic magnetic field. The majority of UV emission from SF regions is reprocessed by dust and emitted in the FIR, from where the supernovae also originate. However, this model begins to break down when considering smaller galaxies with a lower mass, as you would expect more CRs to escape the galaxy before they have radiated most of their energy. Similarly, galaxies with a low dust mass would emit a higher amount of UV radiation as less is reprocessed, which could lead to a break in the FIRC. More complicated models have been developed to try and explain these discrepancies, such as the conspiracy model by Bell (2003). The 'conspiracy' is that the 'missing' FIR and radio emission counterbalance each other. While this preserves the FIRC, it affects its ability to calibrate the SFR–radio luminosity relation. This theory was expanded by Lacki et al. (2010) to examine the range of galactic parameters that would support a linear FIRC. These authors investigated how the radio spectrum is modified by a number of different parameters including gas density, the initial energy of CRs injected into the ISM, and the escape time of the CRs. The authors also modelled the effect of CR protons produced by supernovae and their decay products, and found that the majority of galaxies (with $\rho_{gas} > 0.01$g cm^{-3}) are UV and CR calorimeters and that below this the FIRC is maintained by the standard 'conspiracy'. However, starburst galaxies have a more complicated relationship. Their radio emission is reduced by CRs losing the majority of their energy through inverse Compton scattering and bremsstrahlung radiation. This is counteracted by the emission from secondary CR electrons produced by the decay of CR protons. These findings are supported by those of Magnelli et al. (2015) who found no change in the FIRC with specific star formation rate (sSFR).

Whether or not the FIRC is redshift dependent is still a point of contention. Some theoretical works predict redshift evolution caused by inverse Compton scattering of cosmic rays with the warmer cosmic microwave background (CMB; Murphy (2009)), leading to higher flux ratios (q_{TIR} defined as the FIR luminosity divided by the radio luminosity, to calculate q_{TIR}; see Eq. 3.4). Others suggest the FIRC should remain unchanged up to $z \simeq 1.5$ (Lacki et al., 2010). Observational discrepancies exist as well, with some studies finding that the median q_{TIR} decreases with redshift (Delhaize et al., 2017; Calistro Rivera et al., 2017) whilst others have found no significant evolution with redshift (Sargent et al., 2010; Smith et al., 2014; Delvecchio et al., 2021). This topic is further complicated by potential evolution in the FIRC with luminosity (either radio or IR). If the median FIRC is different for more luminous galaxies, then when observing at higher redshift, where there is a bias towards more luminous galaxies, an apparent redshift evolution would be observed where none exists (unless steps are taken to account for this in sample selection). Using InfraRed Astronomical Satellite (IRAS) data and DR1 of the LoTSS, Wang et al. (2019) found the FIRC to be sublinear at 150MHz for the most IR-luminous galaxies (their sample had a median redshift of $z \sim 0.05$), lending evidence to this theory. Similarly, Heesen et al. (2019) also found a sublinear relation between radio and SFR (which is correlated with IR luminosity) for spatially resolved galaxies in the local Universe. In addition, the degeneracy between redshift and luminosity evolution could result in a degeneracy between redshift and other galactic parameters, such as stellar mass. Resolving these degeneracies requires a sample of galaxies for which the selection effects are firmly understood with respect to all these parameters. Then, the evolution of the FIRC with respect to each parameter could be studied in isolation.

Recent studies found evidence that the FIRC is mass dependent, i.e. that for a fixed IR luminosity, a galaxy with a higher stellar mass will have a greater radio luminosity. Using deep COSMOS data at 1.4GHz, Delvecchio et al. (2021) found that q_{TIR} is linearly proportional to M_* over a wide range of redshifts and stellar masses ($0.1 < z < 4$ and $8.5 < log(M_*) < 11.5$). Due to the small area of COSMOS (< 2.0 deg^2), the low-redshift measurements made by these latter authors have a large uncertainty. In particular, the high-mass, low-redshift galaxies (z¡0.4) have a higher normalisation than the higher redshift ($z > 0.4$) galaxies. In addition, using the LoTSS deep field data in ELAIS-N1, Smith et al. (2021) found that the radio luminosity–SFR relation is mass dependent, that is, for a given radio luminosity a higher mass galaxy will have a lower SFR than a galaxy with a lower stellar mass.

Smith et al. (2014) and Read et al. (2018) showed that, as dust temperature increases, the FIRC decreases for monochromatic fluxes (fluxes were measured at 100, 160, 250, 350, and 500 μm). In addition, Molnár et al. (2018) showed that, for a sample of star-forming galaxies, the FIRC decreases more sharply with redshift for spheroid-dominated galaxies compared to spiral galaxies. This discrepancy could be attributed to possible low-level AGN activity that is boosting the radio emission but is undetected at other wavelengths. This is qualitatively supported by Sabater et al. (2020) who showed, using a mass-selected sample, that all massive galaxies have low radio emission from AGN activity. In addition, the recent discovery that the FIRC is mass dependent can help to explain these findings, as for a given stellar mass a spheroidal galaxy will usually have a higher mass.

The majority of existing studies of the FIRC have been undertaken at 1.4GHz (Terzian (1972); Bell (2003); Sargent et al. (2010); Delhaize et al. (2017); Delvecchio et al. (2021) to name a few), whereas there are relatively few studies of the FIRC at lower frequencies. Low-frequency (150MHz) observations have the advantage that they are not affected by contamination from thermal emission from gas ionised by nearby massive stars. This emission is more relevant at higher frequencies, and while both synchrotron and thermal emission mechanisms are linked to massive stars, the interplay between these two mechanisms is not known. Using wide-area LOFAR data combined with SDSS, Gurkan et al. (2018) found the radio–SFR relation was best fitted by a broken power law at 150MHz, also finding that for a given SFR there is a mass dependence on the radio luminosity. A further discovery by Gurkan et al. (2018) was that galaxies not classified as star forming had a greater radio luminosity than would be predicted from their SFR, implying low-level AGN activity. Read et al. (2018), Smith et al. (2021) expanded on this latter study, finding that the FIRC varies explicitly with stellar mass and redshift. A redshift evolution was also found by Calistro Rivera et al. (2017) using a radio-selected sample from LOFAR data at 150MHz in Boötes.

This work expands on previous studies at 150MHz by using new, deep LOFAR observations in ELAIS-N1 (with an rms noise of 20μJy) that overlap with deep optical data, covering 7.15deg^2 in total, (Sabater et al., 2021) and new deblended *Herschel* fluxes provided through the *Herschel* Extragalactic Legacy Project (HELP; Hurley et al. (2017); Vaccari and Consortium (2015)). Here, we therefore cover three times the area of the Jansky Very Large Array (JVLA) survey in COSMOS (Smolčić et al., 2017) while reaching a similar depth (assuming a spectral index of -0.7) allowing us to probe brighter radio and FIR luminosities, which are rarer (Gruppioni et al., 2013; Sabater et al., 2020). In addition, making use of the XID+ tool (Hurley et al., 2017) to obtain more accurate deblended fluxes for the FIR allows us to push to fainter galaxies in the FIR. Finally, new, aperture-matched optical and photometric redshifts, produced as part of the LoTSS deep fields data release (Kondapally et al., 2021; Duncan et al., 2021), allow us to create multiple mass-complete samples out to a redshift of one and investigate whether or not the presence of low-level AGN activity biases the FIRC by observing the relation with stellar mass. In Sect. 3.2 we discuss the optical, radio, and FIR datasets used and the physical parameters that are estimated from them. In Sect. 3.3 we discuss how these datasets are cross-matched to form a joint catalogue and give details on how FIR fluxes were measured for each radio galaxy in the three deep fields (Boötes, ELAIS-N1 and Lockman). Section 3.4 details how our mass complete sample was constructed in ELAIS-N1 and how AGN were removed from this sample. In Section 3.5 we present our measurement of the FIRC and validate our methods by comparing with the simulated infrared dusty extragalactic sky (SIDES) simulation (Béthermin et al., 2017). In Section 3.6 we compare our results with previous measurements of the FIRC and discuss the implications of the FIRC dependence on stellar mass. In addition, we examine the non-linearity of the FIRC at 150MHz and investigate the dispersion around the FIRC. Throughout this work, we assume a ΛCDM cosmology with $\Omega_m = 0.3$, $\Omega_\Lambda = 0.7$, and $\mathrm{H_o} = 70\mathrm{km\ s^{-1}Mpc^{-1}}$.

3.2 Data

Here we present an outline of the datasets and data products used for this work.

3.2.1 150 MHz radio data

As part of the LOFAR all Sky Survey (Shimwell et al., 2017), deep radio observations have been taken in selected fields (Boötes, ELAIS-N1, and Lockman Hole). A full description of the method used to produce the radio image and source catalogue can be found in Tasse et al. (2021) for Boötes and Lockman-Hole and Sabater et al. (2021) for ELAIS-N1. The radio coverage extends well beyond the optical and FIR datasets, and so only a subset of the radio sources can be used. The overlapping area and the properties of the radio catalogues are summarised in Table 3.1. All radio observations have an angular resolution of 6".

3.2.2 Optical and near-infrared

To create a homogeneous catalogue from the UV to near-infrared (NIR), Kondapally et al. (2021) produced new photometric catalogues in the ELAIS-N1 and Lockman-Hole

Table 3.1: Description of the radio data available in each of the LoTSS deep fields

Field	Overlap area	150MHz rms depth	No. 150MHz Sources	SPIRE limit 250, 350, 500μm	PACS limit 100, 160μm	MIPS limit 24μm
	[deg^2]	[μJy]		[mJy]	[mJy]	[μJy]
Boötes	9.50	30	18766	5, 5, 10	12.5, 17.5	20
ELAIS N-1	7.15	20	31059	4, 4, 6	12.5, 17.5	20
Lockman	10.73	23	29784	4, 4, 6	12.5, 17.5	20

Overlap area is the area of the radio observations that overlaps with the ancillary multi-band (Kondapally et al., 2021) data. Depth is the average rms noise in the overlap region (Mandal et al., 2021). The SPIRE, PACS, and MIPS limit is the faintest a source can be and still have a reliable flux measurement from XID+.

(Brown et al. (2008) have already created a homogenous catalogue in Boötes). In ELAIS-N1 and Lockman Hole, this was done by first generating pixel-matched mosaics from a range of deep, wide-area optical, NIR, and mid-infrared (MIR) surveys. Sources were then detected using deep χ^2 detection images (Szalay et al. 1999), which incorporated multi-band information with photometry extracted using SExtractor (Bertin, 1996) in UV to MIR bands at various apertures. The full details of the catalogue-generation process are described in Kondapally et al. (2021). In Boötes, the existing I-band and 4.5-μm catalogues of Brown et al. (2007, 2008) were cross-matched to generate the multi-wavelength catalogue.

3.2.3 Far-infrared

The FIR data used in this project are from three different instruments: Spectral and Photometric Imaging Receiver (SPIRE, Griffin et al. (2010)) and Photodetector Array Camera and Spectrometer (PACS, Poglitsch et al. (2010)) taken from the *Herschel* Multi-Tiered Extragalactic Survey (HerMes) project (Oliver et al., 2012) as well as the Multi-band Imaging Photometer for Spitzer (MIPS Rieke et al. (2004)), taken from the *Spitzer* mission. These images have been collected and homogenised as part of the HELP (*Herschel* Extragalactic Legacy Project) project. All FIR fluxes were measured using XID+ (Hurley et al., 2017). XID+ is a Bayesian probabilistic deblending tool that measures the contribution of galaxies detected at shorter wavelengths (with higher resolutions) to the FIR images. This is done by modelling the observed maps as a combination of flux from every source, as well as the contribution from instrumental and confusion noise (Σ_{int} and

Σ_{conf}). Using Bayes theorem (Eq. 3.1), XID+ explores the flux posterior for every galaxy in the prior list ($\mathbf{s_i}$) with Hamiltonian Monte Carlo (HMC, Safarzadeh et al. (2014)),

$$P(\mathbf{s_i}, \Sigma_{int}, \Sigma_{conf}|d) \propto P(\mathbf{s_i}, \Sigma_{int}, \Sigma_{conf})P(d|\mathbf{s_i}, \Sigma_{int}, \Sigma_{conf}), \tag{3.1}$$

where d is the map, $\mathbf{s_i}$ is the flux of the sources in the prior list, Σ_{int} is the instrumental noise and Σ_{conf} is the confusion noise. There are several advantages of using XID+ to measure the flux posterior for sources from a prior list instead of cross-matching blind FIR catalogues to optical catalogues. Firstly, it allows multiple galaxies to be detected within a single beam, including sources whose pixel S/N is below 3σ. In addition, the full posterior allows us to accurately measure flux errors.

The prior list from the HELP XID+ run is constructed from galaxies detected at optical wavelengths, which are less affected by confusion. Fluxes for each galaxy are taken as the 50th percentile of the flux posterior and the 84th and 16th percentiles are taken as the upper and lower errors, respectively. To ensure that the measured fluxes are not dominated by the prior, we can look at the faintest sources. If a galaxy included in the prior list does not contribute to the FIR maps, then its flux posterior will be dominated by a convolution of the prior and the flux distribution of the map (a Gaussian skewed towards zero). These faint sources would all have a high skew (defined here as the 84th-50th percentile divided by the 50th-16th percentile as opposed to measuring the skew of Gaussian fit to the posterior). By looking at the skew as a function of flux we can find the flux at which the majority of galaxies become skewed (see Figure 3.1) by eye. The flux posterior of galaxies whose flux is below these cutoffs are dominated by the uniform prior, as the map is providing little to no information. As the posterior flux is dominated by the uniform flux prior and noise level of the map, the posterior of these sources has not been informed by the data and so XID+ flags these sources. These flags are included in the FIR flux catalogues.

The FIR fluxes that are available from HELP are at 24 (from Spitzer MIPS observations), 100, 160, 250, 350, and 500μm (from *Herschel* PACS and SPIRE respectively, Pilbratt et al. 2010) which required two different prior lists for XID+, one for 24μm and one for the longer wavelengths (due to the differences in resolution between MIPS and PACS + SPIRE). The prior list for 24μm was constructed from a subset of the HELP masterlist. This was created by merging optical, NIR, and MIR catalogues that overlap with the *Herschel* observations, the details of which can be found in Shirley et al. (2019). This is necessary because if the 24μm prior list were instead comprised of the entire HELP masterlist then XID+ would find a large degeneracy in the galaxy fluxes due to the high source density relative to the MIPS resolution. To remove this degeneracy, we exclude sources from the prior list that are expected to have a negligible 24μm flux density. To this end, a number of cuts were applied to the merged catalogue to select sources that have significant emission at 24μm. The prior list used for deblending the MIPS observations was constructed by only including objects detected by *Spitzer* (3.6-8.0μm) and at shorter wavelengths. These cuts select objects most likely to be bright at 24μm while removing artifacts from *Spitzer*. The PACS and SPIRE prior list was constructed by only considering objects from the 24μm prior list whose 24μm flux density was greater than the cutoff flux (Figure 3.1; this is the same 24μm flux density cut used to define the PACS and SPIRE prior list) as there is a correlation between flux at 24μm and flux measured from PACS and SPIRE. A uniform flux prior was used for MIPS, PACS, and SPIRE.

For each galaxy, we can also examine the goodness of fit of the flux posterior. By looking at the flux distribution of a pixel, we can evaluate how likely we are to draw the measured pixel flux. If on average the pixels to which a given source is contributing are more than 2σ away from the true value then we flag that source as having an unreliable flux. This can be caused by missing a source from our prior list that is contributing to the map or because the included source does not contribute to the map.

Additional FIR bands were available from MIPS (70 and 160 μm) and PACS (70 μm) as well as 850μm from SCUBA-2. However, the additional data from PACS and MIPS are of very low sensitivity and would therefore add very little value. The SCUBA-2 data typically probe higher redshift galaxies while LOFAR predominantly observes lower redshift star-forming galaxies. In addition, there are only several thousand galaxies detected in the SCUBA-2 Cosmology Legacy Survey (S2CLS; Geach et al. (2017) survey in Lockman-Hole and these can be cross-matched to the LOFAR catalogue by a simple nearest neighbour cross-match. This was done by Ramasawmy et al. (2021) and found only tens of matches, and so it has not been included in the data release.

3.2.4 Physical parameters and SED fitting

Photometric redshifts were measured for the full multi-wavelength catalogues using the method outlined in Duncan et al. (2021), which is briefly summarised here. By combining Gaussian processes and template fitting using a hierarchical Bayesian framework, photometric redshifts were estimated from multi-band photometry spanning from the near-ultraviolet (NUV) to NIR. The Gaussian processes were trained on galaxies with a spectroscopically confirmed redshift.

SEDs were computed for each radio source with a multi-wavelength cross-match using five different SED fitting codes: BAGPIPES (Carnall et al., 2019), MAGPHYS (Da Cunha et al., 2008), AGNFITTER (Calistro Rivera et al., 2016), and CIGALE using two different AGN models: namely those of Fritz et al. (2006) and Stalevski et al. (2016). A full comparison of the results of each of the SED-fitting codes is presented by (Best et al. (2021); in prep). Here we give a brief description. Good agreement was found between all the codes for the stellar mass, SFR, and dust luminosity, with some small scatter, but no systematic offsets. The codes differ in their treatment of AGN; both BAGPIPES and MAGPHYS do not contain any AGN components in their models whereas AGNFITTER and CIGALE do. As a general rule, when there is no significant AGN activity in a galaxy, MAGPHYS and BAGPIPES obtain better fits than either AGNFITTER or CIGALE as with fewer parameters they are able to better explore their parameter space. On the other hand, MAGPHYS and BAGPIPES do not provide good fits for the majority of AGN, which are better fit by CIGALE and AGNFITTER. A comparison of the results of the different codes therefore allows identification of sources with AGN features; a full description of the AGN identification method is presented in section 3.4.2.

3.3 Cross-matching

3.3.1 Radio to multi-wavelength

The radio sources were cross-matched to the multi-wavelength catalogue using a combination of likelihood ratio (LR) and manual cross-matching as described in Kondapally et al. (2021). Likelihood ratios are calculated using the formula from (Sutherland and Saunders, 1992):

$$LR = \frac{q(m,c)f(r)}{n(m,c)}, \tag{3.2}$$

where $q(m,c)$ is the combined magnitude colour distribution of the true radio counterparts, $n(m,c)$ is the normalised magnitude colour distribution of all multi-wavelength sources, and $f(r)$ is the probability of the separation between the radio and multi-wavelength source.

Manual cross-matching was carried out for sources that were deemed unsuitable for LR cross-matching and were then visually inspected using the LOFAR galaxy zoo platform. Unsuitable sources included extended sources, sources with multiple Gaussian components, and clustered sources. Members of the LOFAR consortium inspected the optical/NIR

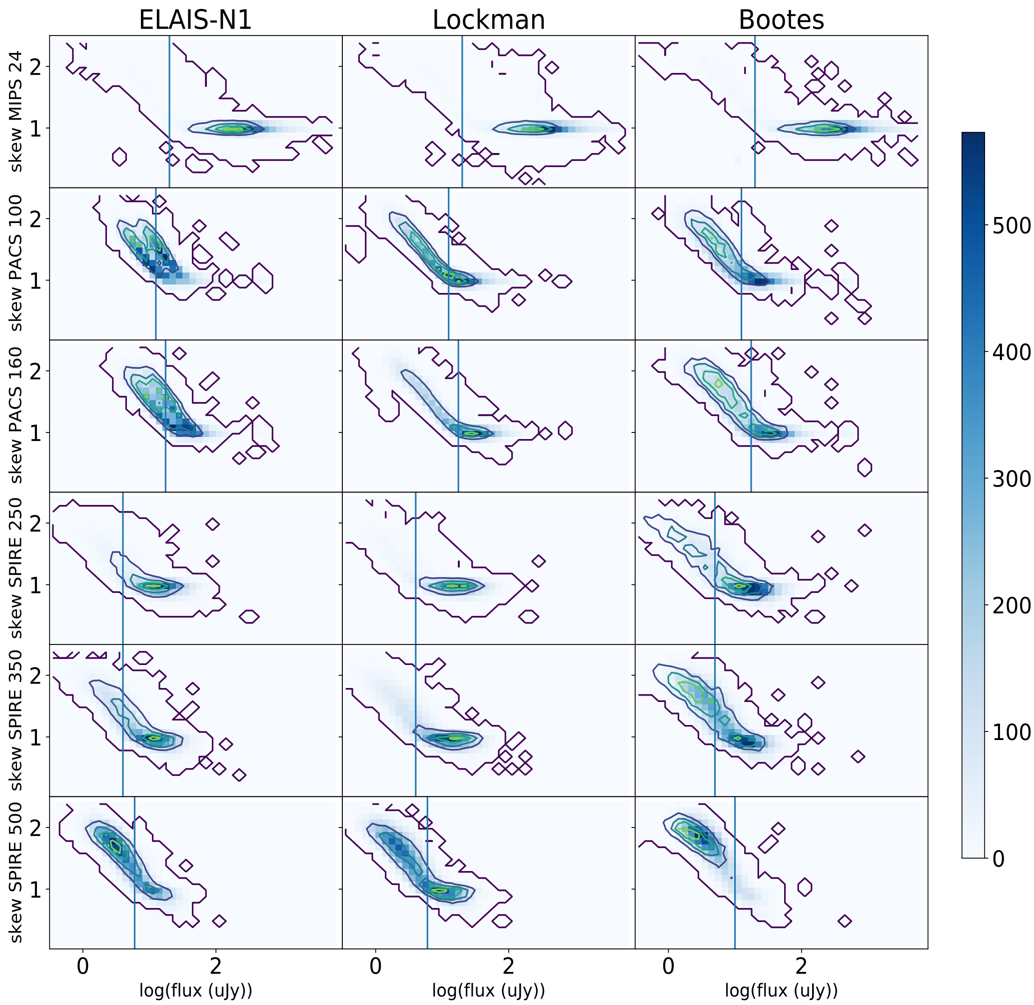

Figure 3.1: Skew of the XID+ fluxes for all MIPS, PACS, and SPIRE bands in the three LOFAR deep fields. The contours show the density of the LOFAR sources whose multi-wavelength counterpart was originally undetected in the FIR. The histogram beneath the contours shows the distribution of all FIR sources in the LOFAR catalogues with higher populated histograms having a yellower colour and less populated bins being bluer. The vertical lines show the flux below which a source's posterior is dominated by the prior.

postage stamps around the radio source overlaid with the radio contours and made their best interpretation in regards to the true multi-wavelength counterpart. Each radio galaxy was inspected by five different members and then if a consensus had been reached on the galaxy counterpart(s) then this was taken. If no clear consensus had been reached, then either the galaxy would not be assigned a counterpart, or it would be sent to an expert workflow where it was inspected in more detail. This choice depended on the reason for no consensus being reached and is discussed in full in Kondapally et al. (2021).

3.3.2 Far-infrared cross-matching

We used the following procedure to measure the FIR flux from the radio sources. First we cross-matched the LOFAR multi-wavelength counterparts with the HELP prior list using a search radius of 0.5", which corresponds to the positional uncertainty of the *Spitzer* IRAC sources. If there is a source from the HELP prior list within 0.5" then the FIR fluxes measured for that source were assigned to the radio counterpart. If the radio source has no multi-wavelength counterpart or there is no HELP prior list source within 0.5" then XID+ is rerun around each of these sources using the same prior list as HELP but with the addition of the radio source (using the position of the multi-wavelength counterpart if there is one, otherwise the radio position is used) and a uniform flux prior is used. For the HELP XID+ run, the FIR maps were divided into tiles of equal area based on the HEALPIX tiling system, which were individually run through XID+. As the XID+ run for LOFAR uses circular regions (with a radius of 60"), because we did not need to rerun XID+ across the entire deep fields, we compared the fluxes we measured for the non-radio-galaxy counterparts to their fluxes measured in HELP. The results can be seen in Figure 3.2 and show good agreement between the two measurements within their measured uncertainty (i.e. $\approx 60\%$ of sources agree within one σ). The results are symmetric about the $x = y$ line apart from a subset of sources that are brighter in HELP than in the LOFAR run. These sources are all close to the new radio galaxy that was added to the prior list. We would expect them to be fainter in the LOFAR run as the flux in the map is being assigned to the radio source. In total we have FIR fluxes for 79,609 galaxies with detections at 150MHz across the three deep fields.

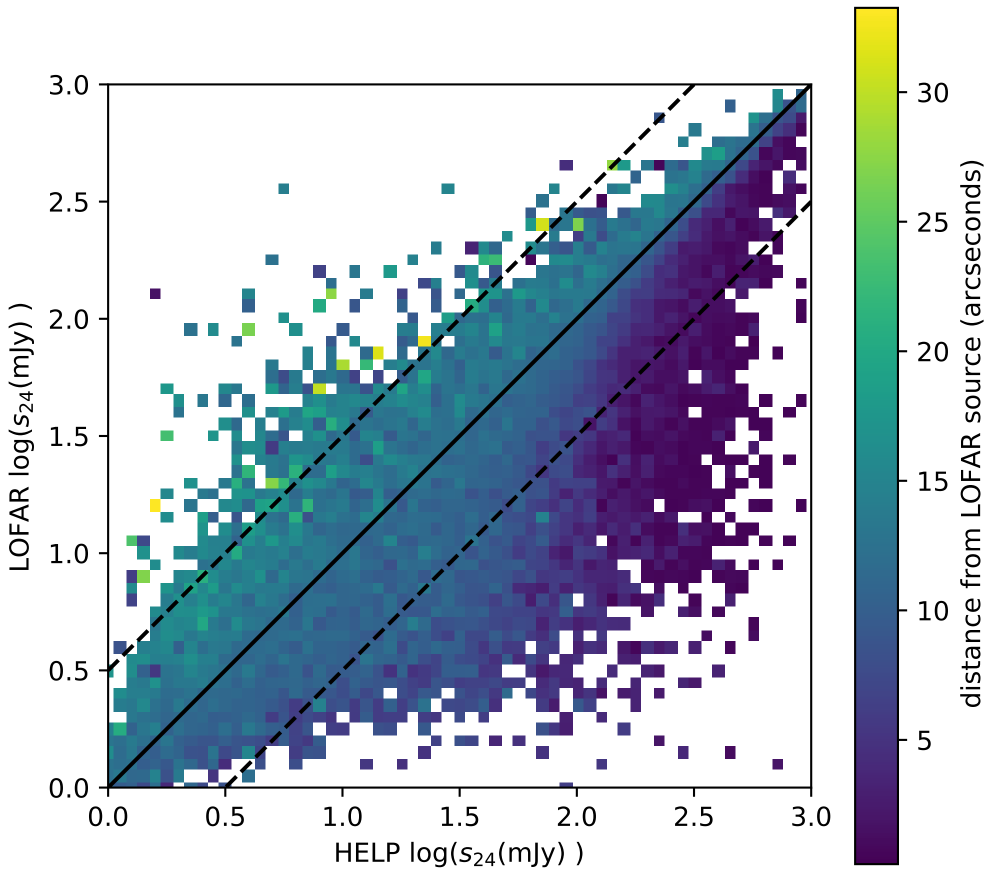

Figure 3.2: Comparison between the flux measured with XID+ using the HELP and LOFAR prior lists. The colour shows the average distance from the LOFAR source for all sources in that bin (and hence the centre of the rerun region). We note the asymmetry about the x=y line on the right hand side of the plot where sources are brighter with the HELP prior compared to the LOFAR prior. This discrepancy is caused by the inclusion of the radio source in the LOFAR prior that causes sources in the HELP prior to have less flux assigned to them. The flux measurement from the LOFAR prior list is consistent with the measurement using the HELP prior list.

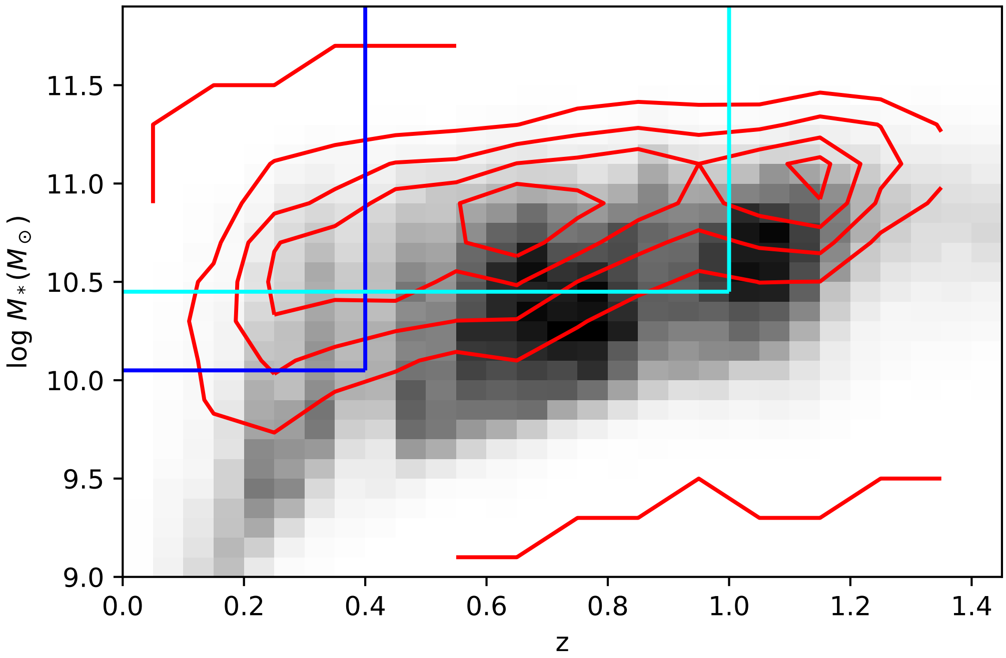

Figure 3.3: Stellar mass–redshift distribution of the Smith et al. (2021) SED fits. The red contours show the distribution for galaxies with a detection at 150MHz and the grey histogram shows the distribution for the galaxies without a detection at 150MHz. The dark blue lines show the region selected for our mass sample and the light blue lines show the region selected for our redshift sample.

3.4 Sample creation

3.4.1 Mass selection

To investigate how the FIRC depends on redshift and stellar mass we need to construct mass-complete samples, and we use the MAGPHYS SED fits from Smith et al. (2021) in ELAIS-N1 to construct these. Smith et al. (2021) used MAGPHYS to measure the SED for galaxies in the LOFAR catalogues with a 3.6μm flux density $> 10\mu$Jy and estimated the completeness in stellar mass as a function of redshift using the method from Pozzetti et al. (2010). We created two samples using this information one with $z < 1.0$ and $M_* > 10^{10.45}$, and the other with $z < 0.4$ and $M_* > 10^{10.05}$ to investigate the dependence of the FIRC on redshift and stellar mass, respectively (Figure 3.3). We shall refer to these samples as the redshift sample and the mass sample and the limits were chosen to be 95% complete at 3.6μm (Duncan et al., 2021).

MAGPHYS uses energy balance to match UV/optical and FIR templates so that the energy attenuated by dust in the UV/optical is equal to the energy radiated in the FIR. This energy balance allows an estimate of the TIR luminosity even when there are no individual FIR flux measurements, which ensures that all galaxies in our sample have a TIR luminosity measurement (Appendix 3.16 shows the distribution of galaxies with less than one detection in SPIRE and PACS). The effect of using the energy balance approach when a galaxy has no individual detections from PACS or SPIRE is validated in Appendix 3.16 to ensure that no systematic bias is introduced from the SED fitting. In addition, Małek et al. (2019) tested the use of energy balance in measuring TIR luminosities by measuring the TIR luminosity for galaxies when their FIR fluxes were included and excluded and found the results to be in good agreement. This analysis was carried out using CIGALE rather than *magphys* but the energy balance principle used in both SED fitters is the same and gives us confidence that there is no systematic bias in the TIR luminosity measurements for galaxies with no PACS or SPIRE fluxes.

Not all galaxies have a radio detection and therefore an upper limit on the radio flux is calculated (detailed in next paragraph). We then impose a cut on specific star formation rate (sSFR, SFR/M_*) to select star-forming galaxies. For a galaxy to be considered as star forming, it must be no more than 0.6 dex below the main sequence (MS). We calculate the expected value of the main sequence (MS) for each galaxy using Eq. A1 from Sargent et al. (2014) depending on its stellar mass and redshift. We use 0.6 dex as this corresponds to two standard deviations away from the MS (the effects of changing the offset from 0.6 dex are discussed in section 3.6.1). This cut removes passive galaxies from our sample while not excluding starburst galaxies. Lacki et al. (2010) showed that starburst galaxies should theoretically lie along the FIRC and Magnelli et al. (2015) found this to be true in COSMOS. Therefore, we do not apply a cut above the SF main sequence. Table 3.2 shows how the different cuts reduce the number of galaxies in our sample (we also remove AGN from our sample and this is discussed in section 3.4.2).

For galaxies with a radio detection, we calculated their rest-frame luminosity at 150MHz using

$$L_{\nu 1} = \frac{4\pi D_L^2}{(1+z)^{(\alpha+1)}} \frac{\nu_1}{\nu_2} S_{\nu 2}, \tag{3.3}$$

Where $L_{\nu 1}$ is the luminosity at the restframe frequency (or frequency you are converting to in the case of converting between different frequencies), D_L is the luminosity distance, α is the spectral index between the frequencies ν_1 and ν_2 and S_{nu2} is the observed flux (or the flux at the frequency you are converting from). To calculate the luminosity at 150MHz we used ν_1 as 150MHz and ν_2 as the observed frequency, calculated using the galaxies

Table 3.2: Number of galaxies in our sample after each cut is made

	z, M_*	sSFR	AGN
Mass sample detections ($z < 0.4$, $M_* > 10^{10.05}$)	3464	2417	2353
Mass sample limits ($z < 0.4$, $M_* > 10^{10.05}$)	10447	1798	
Redshift sample detections ($z < 1.0$, $M_* > 10^{10.45}$)	10046	7190	6856
Redshift sample limits ($z < 1.0$, $M_* > 10^{10.45}$)	41763	9784	

Each column shows the number of galaxies in our sample after each successive cut is made. The cuts are made in z, M_* plane, sSFR, and to remove AGN. The two rows for each sample show the detections at 150MHz and limits at 150MHz. There is no number in the AGN column for the limits because AGN are excluded automatically based on their MAGPHYS chi2 flag which identifies bad fits, making it impossible to identify which of those galaxies are AGN.

redshift. We take the spectral index to be -0.60 which is the spectral index measured between 150MHz and 325MHz in Calistro Rivera et al. (2017) which is appropriate to use for our sample of z<1 galaxies as the highest rest frame frequency in our sample is 300Hz. For the sources with no radio detection, we calculate a limit on their radio luminosity by taking the flux at 150MHz to be 5σ, where σ is the rms noise in the pixel that contains the galaxy. This assumes that the undetected radio sources are spatially unresolved, which is valid due to the large angular resolution (6”) and is consistent with the threshold used to detect radio sources with PYBDSF (Tasse et al., 2021; Sabater et al., 2021).

3.4.2 AGN identification

The FIRC is believed to originate from radio and FIR emission linked to SF. The removal of AGN is essential for accurate measurement of this relation and its scatter. AGN can contribute to a galaxy’s SED in the IR and radio and thus could contaminate the FIRC.

Galaxies in our sample were identified as AGN if they were flagged as AGN in Duncan et al. (2021) —which includes AGN identified using their NIR colours following the criteria in Donley et al. (2012)—, had bright x-ray counterparts, were spectroscopically identified as AGN, or are part of the Million Quasar Catalog (Flesch, 2019). In addition, Best et al. (2021) identified AGN in radio-detected sources (at 150MHz) using the four different SED fits described in 3.2.4 as well as looking for evidence of excess radio emission based on the SFR–radio relation or extended radio emission. Finally, as part of selecting galaxies with a reliable MAGPHYS SED we excluded fits that had a poor χ^2 (see Smith et al. (2012)

for more details). Smith et al. (2021) found that 94% of galaxies flagged as AGN in Best et al. (2021) are also flagged by this method, and so we can be confident that AGN have been removed even if they are undetected in the radio.

3.5 Far-infrared radio correlation

We parameterise the FIRC using q_{TIR} (the log ratio of the TIR to radio luminosity), defined as

$$q_{TIR} = \log\left(\frac{L_{TIR}}{3.75\times10^{12}\mathrm{Hz}}\right) - \log\left(\frac{L_{150\mathrm{MHz}}}{\mathrm{WHz}^{-1}}\right), \tag{3.4}$$

noting that L_{TIR} is divided by the central frequency of 3.75×10^{12} to ensure that q_{TIR} is dimensionless, and calculate q_{TIR} for every galaxy in our sample. If a galaxy has an upper limit on its radio luminosity, then we calculate a lower limit of q_{TIR} for that galaxy. We can then measure the median q_{TIR} of our sample of galaxies using a survival analysis to account for the lower limits in q_{TIR}. The survival analysis works by redistributing the lower limits assuming they follow the same underlying distribution, without making any assumptions as to the form of this distribution. This is implemented using the LIFELINES PYTHON package (Davidson-Pilon et al., 2021), which uses the Kaplan Meier estimator (Kaplan E. L. and Meier Poul, 1958), which in turn has had multiple applications within astronomy (Schmitt, 1985). The median q_{TIR} of our sample was measured by bootstrapping the survival analysis. This was done by repeating the measurement of the median using survival analysis 1000 times on a random 90% of our sample and the median measured for each of these samples. The median q_{TIR} was taken as the mean of the distribution of medians from our bootstrapped samples and the error was taken as the standard deviation of the samples.

In the following sections, we describe how we validated our methodology by adding radio emission to the simulated IR dusty extragalactic sky (SIDES; Béthermin et al. (2017)) simulation using a simple model. We then describe how the FIRC varies with different physical parameters.

3.5.1 SIDES FIRC simulation

To validate our methodology, we created a simulation of our samples using the SIDES simulation (Béthermin et al., 2017). SIDES simulates galaxies by generating their stellar mass from stellar mass functions. These galaxies are then matched to dark matter halos by abundance matching. Galaxies are then assigned to be either star forming or quiescent with the probability of a galaxy being star forming depending on its stellar mass and redshift. The FIR properties of the galaxies are then calculated based on their SFR; if a galaxy is quiescent then it has no FIR emission. It should be noted that AGN are not included in the SIDES simulation.

To ensure that our sample selection does not introduce any significant bias, we selected a mass-complete sample from the SIDES simulation using the same selection criteria as those used to create our real mass sample (i.e. $M_* > 10^{10.05}$ and $z < 0.4$) and removed galaxies based on their sSFR using the method described in section 3.4.1. As the SIDES simulation does not include radio emission we created a simple model to add emission at 150MHz to the SIDES galaxies that have $\log(M_*) > 10.05$ and $z < 0.4$. This was done by first giving each galaxy a q_{TIR} value drawn from a Gaussian distribution with mean 1.8 and standard deviation 0.35. These parameters were chosen to provide a reasonable match to the q_{TIR} distribution of the mass-complete sample. It should be noted that the distributions do not completely match and it is clear that the real q_{TIR} distribution is not Gaussian. However, for the purposes of validating our method we do not need to perfectly reproduce our data. As we are measuring the median q we are unaffected by the small number of galaxies with low q values. As every galaxy has a q_{TIR} value assigned to it, we can compute its radio luminosity and flux at 150MHz and then determine whether or not it would be included in our radio catalogue (i.e. if $S_{150MHz} > 0.1$mJy). If a galaxy would not have been detected then we computed the upper limit of its radio luminosity using Eq. 3.3 and taking the upper limit on its flux to be 0.1mJy (0.1mJy is the average 5σ rms noise) and then recalculated its q_{TIR} using Eq. 3.4. We then performed a survival analysis on the simulated galaxies to measure the median of the 'observed' q_{TIR} distribution, taking lower limits of q_{TIR} into account, and found it to agree with the true median within the measured uncertainty (Figure 3.4).

We then modified our simple model to incorporate an evolution of q_{TIR} with stellar mass. To do this, we set the mean of the Gaussian distribution used to draw q_{TIR} to a function of stellar mass, $\mu = N(1 + M_*)^\gamma$.

To investigate whether q_{TIR} evolves with stellar mass, we divided our simulated galaxies into ten stellar mass bins such that the bins had an equal number of galaxies in them. The median q_{TIR} in each bin was then measured using a survival analysis. We can then fit a power law of the form,

$$q_{TIR} = N(1 + M_*)^\gamma, \tag{3.5}$$

with N and γ as free parameters. To measure the value of the free parameters, we bootstrapped our data by taking a random 90% of our data and fitting the power law to it using the method outlined above. We then took the value of the free parameters to be the median of the 1000 individual values measured, with an uncertainty equal to the standard deviation of the individual values. Using this method we were able to recover the intrinsic (measured by using all the radio luminosities rather than a combination of radio luminosities and upper limits for those with $s_{150MHz} > 0.1$mJy) parameters of the power law within 1σ (figures 3.5 and 3.6). Therefore, if q_{TIR} evolves with stellar mass in our LOFAR sample we are confident that we could recover the power-law parameters for that evolution.

Additionally, we are able to check whether a dependence of the FIRC on stellar mass would cause an observed evolution of the FIRC with redshift. We measured the evolution of q_{TIR} with redshift for a simulated sample of galaxies whose q_{TIR} varies with stellar mass. We found no observed evolution of q_{TIR} with redshift in this scenario. This gives us confidence that if we observe evolution of q_{TIR} with redshift in our redshift sample, then the evolution is genuine and not an artifact of any observed variation with stellar mass.

Finally, we investigated the case where we have more galaxies with upper limits on their radio luminosity than measurements. To change this, we artificially raised the flux limit (0.5mJy for the mass sample and 0.25 for the redshift sample, which gives a ratio of detections to upper limits of $\simeq 0.5$) above which a galaxy is detectable at 150MHz, and remeasured the evolution of q_{TIR} with stellar mass and redshift. We found that having significantly more lower limits on q than direct detections does not cause a significant bias in our results. Even in the lowest mass bin, or highest redshift bin, respectively, where the ratio of detections to upper limits is less than 0.5. These simulations give us confidence that we can correctly measure the underlying parameters that describe the evolution of q_{TIR} with both stellar mass and redshift.

3.5.2 FIRC with stellar mass and redshift

For our redshift sample we measured the median $q = 1.879 \pm 0.002$ (Figure 3.7) with typical uncertainties on individual measurements of q of $0.1 - 0.2$dex. We investigated the evolution of q_{TIR} with redshift within our redshift sample using the method outlined in the previous section. By fitting a power law to measure the redshift evolution we can compare with the results of Delhaize et al. (2017) and Calistro Rivera et al. (2017). The fit parameters can be seen in Table 3.3 (we also fit a linear function). The results can be seen in Figure 3.8 where we show how the median q_{TIR} of our sample changes with

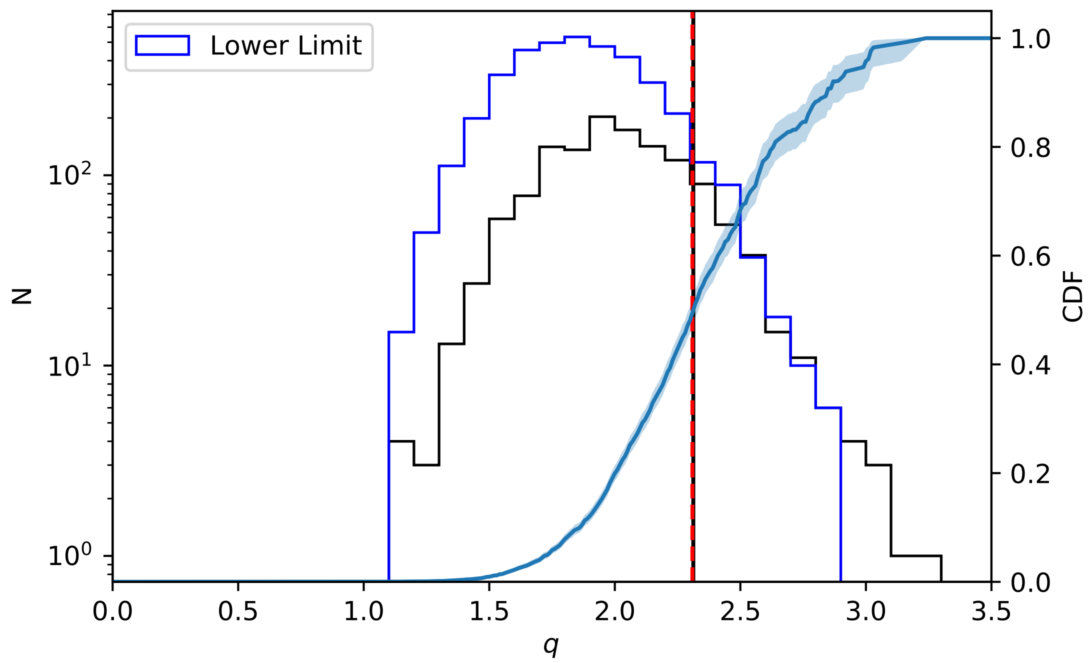

Figure 3.4: Distribution of q_{TIR} values from the SIDES simulation for galaxies with $M_* > 10^{10.45}$ and z<1. The blue histogram is for lower limits of q_{TIR} and the black histogram is for direct detections. The black vertical line (behind the dashed red line) marks the median of the sample, as measured using survival analysis and the red dashed vertical line shows the true median. The slight overestimation of the median is caused by the greater number of lower limits compared to direct detections. The blue line is the CDF of the entire sample, measured using survival analysis.

redshift. The orange line shows our measured relation which shows a much shallower evolution compared to that foubd by Calistro Rivera et al. (2017) and Delhaize et al. (2017) (red and green lines, respectively). We also investigated the evolution of q_{TIR} with stellar mass. This was done by repeating the above methodology with our mass sample to investigate how q_{TIR} depends on stellar mass and the results can be seen in Figure 3.9.

Finally, we investigated the joint evolution of the FIRC with redshift and stellar mass using a sample of galaxies with $z < 0.4$ and $M_* > 10^{10.45}$ (giving 1171 galaxies detected at 150MHz and 281 galaxies with upper limits on their flux at 150MHz). The sample was split into four redshift bins with an equal number of galaxies in each bin and then each redshift bin is split into four stellar mass bins that all have an equal number of galaxies in them. We then fit the combined evolution using the method described above and find an evolution of the form $q_{TIR}(z, M_*) = (1.98 \pm 0.02)(1+z)^{0.02\pm0.04} + (-0.22 \pm 0.03)\log(M_*) - 10.45$.

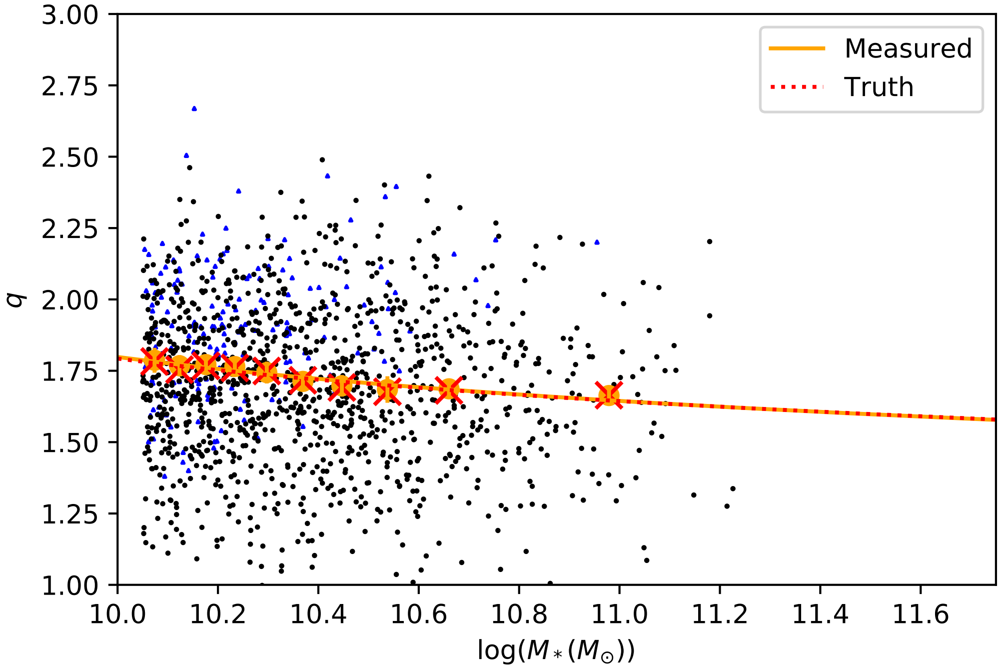

Figure 3.5: Evolution of q_{TIR} with M_* for the SIDES simulation ($\mathrm{M}_* > 10^{10.05}$ and z<0.4) when q_{TIR} is drawn from a Gaussian distribution whose mean is M_* dependent. The orange points are the measured medians in their bins and the orange line is the fit to the medians. The red crosses and line are the true medians and fit; the red line is beneath the orange line.

To further validate our results, we remeasured the median q_{TIR} in our stellar mass bins using two alternative methods. Firstly, we employed the method from Smith et al. (2021). Briefly, in this method the PDF of the stellar mass versus q_{TIR} plane is constructed by sampling from the radio flux posterior and TIR luminosity posterior of an individual galaxy. These posteriors, for galaxies detected at 150MHz, are taken to be Gaussian distributions with mean equal to the measured value (for the TIR luminosity we used to 50th percentile output from *magphys*) and standard deviation equal to the error on that mean. For each posterior sample, we can calculate its radio luminosity and therefore its q_{TIR}. The 150MHz flux posterior for galaxies undetected at 150MHz is taken to be a Gaussian with mean equal to the flux in the pixel where the galaxy is located, and standard deviation equal to the error of the flux in that pixel. Samples with a negative 150MHz luminosity are set to the arbitrary limit of $10^{17}\mathrm{WHz}^{-1}$, and similarly, negative TIR luminosities are set to $10^6 L_\odot$. The samples are then summed in the stellar mass versus q_{TIR} plane to measure the combined PDF. Within each of our stellar mass bins

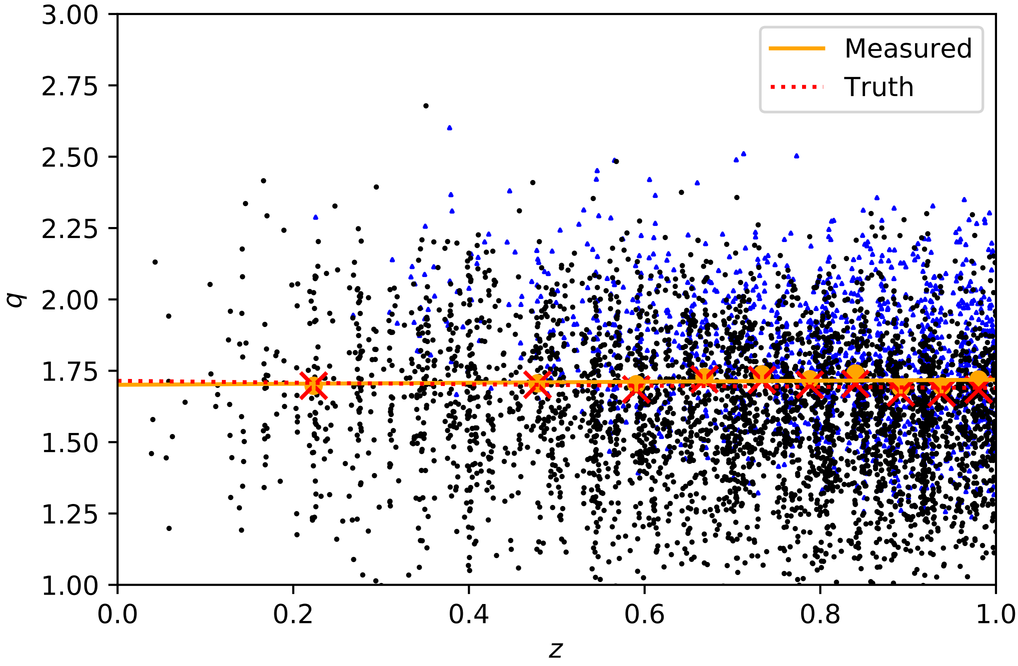

Figure 3.6: Evolution of q_{TIR} with redshift for the SIDES simulation ($\mathrm{M}_* > 10^{10.45}$ and $z < 1.0$) when q_{TIR} is drawn from a Gaussian distribution whose mean is M_* dependent. The orange points are the measured medians in their bins and the orange line is the fit to the medians. The red crosses and line are the true medians and fit.

we can then measure the median q_{TIR} from the combined PDF and compare it to the median q_{TIR} measured using survival analysis (Figure 3.9). The second method employed is stacking. Instead of measuring the upper limit of the flux at 150MHz of each undetected radio galaxy, we measured the average flux at 150MHz for all galaxies within the same stellar mass bin. This was done for all galaxies regardless of whether they were detected or not as the vast majority of our sample is unresolved at 150MHz, and so the pixel flux is equal to the total flux. This was done by taking the mean of the fluxes in the pixels in which the undetected galaxies (undetected at 150MHz) were located (we tested using the median flux instead of the mean and found the answers to be within one standard deviation of each other). This mean flux was converted into a radio luminosity using the mean redshift of those galaxies. The mean q_{TIR} was similarly calculated using the mean TIR luminosity and the results can be seen in Figure 3.9. We note that our crude stacking method does not account for any bias caused by clustering. Therefore, our stacked radio luminosities are likely higher than the true value, which would cause the median q_{TIR} to be lower than the true value and could explain why stacking produces a systematically

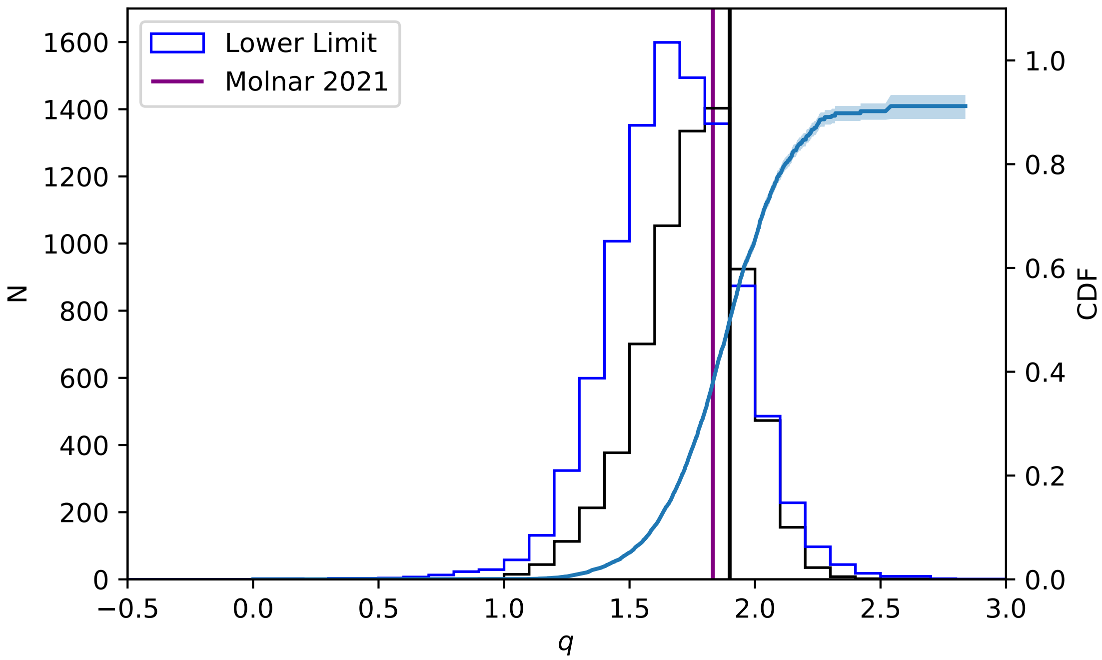

Figure 3.7: Distribution of q_{TIR} values for the redshift sample with M$_*$ > $10^{10.2}$ and z¡1. The black histogram is the q_{TIR} distribution for galaxies that are detected at 150MHz. The blue histogram is the distribution of lower limits of q_{TIR} for galaxies that have an upper limit at 150MHz and therefore their q_{TIR} is a lower limit. The vertical line marks the median of the sample, as measured using survival analysis and the purple line shows the median $q_{TIR}$from Molnár et al. (2021), measured at 1.4GHz and converted to 150MHz using $\alpha = -0.78$.

lower q_{TIR}. The good agreement between all three methods give us further confidence that our method (survival analysis) is able to accurately measure the true evolution of our samples.

Taking the error of our fit parameters as the standard deviation of our bootstrapped parameter distribution will cause us to underestimate the error due to the correlations between the bootstrapped samples. The standard deviation of the bootstrapped distribution is the standard error of the true distribution so the true standard deviation is equal to the standard deviation of the samples multiplied by a factor of root N where N is the number of samples. From Figure 3.11 we can see how the error change when this factor of $\sqrt{N}$ is applied. While the size of the error increases giving a relation of $q(M_*) = 1.98 \pm 0.02 - 0.15 \pm 0.04 M_*$ this increase in the uncertainty doesn't change the conclusions we reach in the discussion.

Table 3.3: Fit parameters for different samples

Sample	Function	Assumptions	Power Law Params		Linear Fit Params	
			γ	N	β_1	β_0
$z < 0.4, M_* > 10^{10.05}$	$q(M_* - 10^{10.05})$	$\alpha_{150}^{325} = -0.60$	-0.16 ± 0.01	1.99 ± 0.01	-0.22 ± 0.01	2.00 ± 0.0
$z < 1.0, M_* > 10^{10.45}$	$q(z)$	$\alpha_{150}^{325} = -0.60$	-0.04 ± 0.01	1.94 ± 0.01	-0.06 ± 0.01	1.93 ± 0.0
Delvecchio 2020	$q(M_* - 10^{10})$	$\nu = 1.4GHz$			-0.12 ± 0.02	2.59 ± 0.0
Rivera 2017	q(z)		-0.22 ± 0.05	1.72 ± 0.04		

The sample column shows the sample considered and where it originates from. The Function column the variables which q_{TIR} is a function of. The Assumptions column lists any extra details the reader should know about the fit, such as the frequency of the observations and the spectral index used. The slope and normalisation of the power law fit are shown in the γ and the N columns respectively while the slope and intercept of the linear fit are shown in β_1 and β_0.

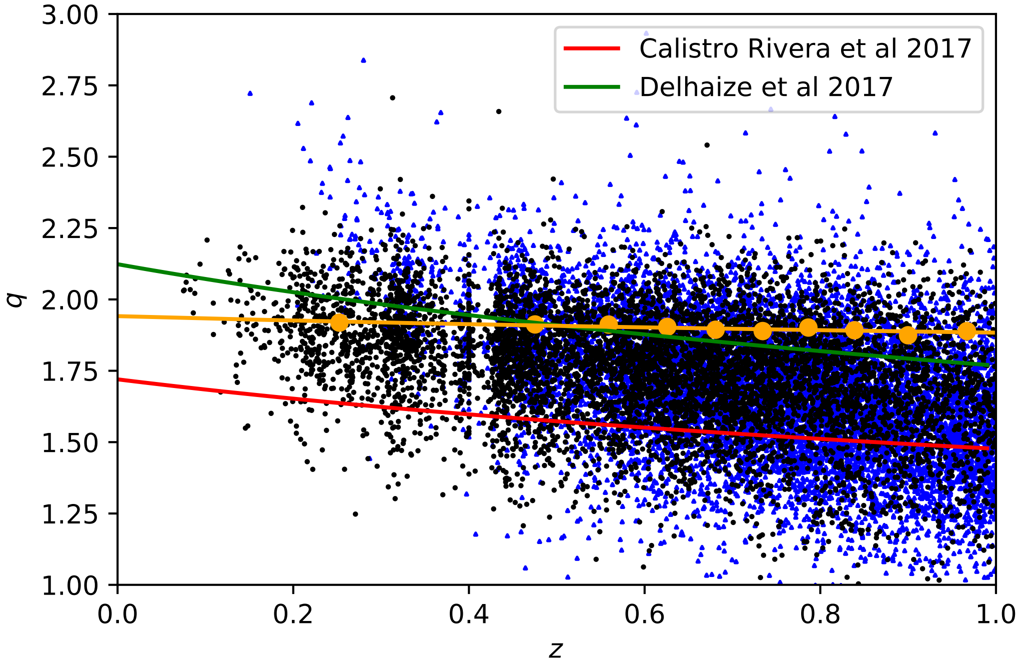

Figure 3.8: Variation of the FIRC at 150MHz with redshift for the redshift sample. The black points are direct detections in the radio and the blue points are undetected in the radio and are therefore lower limits in q. The orange points are the median q_{TIR} measured using survival analysis in each redshift bin and the orange line is the power law fit to those points. The red line is the fit from Calistro Rivera et al. (2017) and the green line is the fit from Delhaize et al. (2017) converted to 150MHz with a spectral index of -0.78.

3.5.3 FIRC non-linearity

There has been little research done into whether the FIRC is non-linear at 150MHz. Wang et al. (2019) found a sublinear relation between radio luminosity for a sample of low-redshift galaxies with high IR luminosities. To test whether the slope of the FIRC is 1, we binned the galaxies from our redshift sample (as this has more galaxies in it) into ten dust luminosity bins, spaced so that there is an equal number of galaxies in each bin. In each bin, we found the median q_{TIR} using the method detailed in Sect. 3.5.2 and converted that median q_{TIR} to a radio luminosity using Eq. 3.4 and taking L_{TIR} to be at the centre of the bin. We then fit a linear relation to these data points of the form $L_{TIR} = \beta_1 L_{150MHz} + \beta_0$ and found $\beta_1 = 0.90 \pm 0.01$, $\beta_0 = -9.8 \pm 0.3$ (Figure 3.12). This shows a statistically significant deviation from a linear FIRC. However, due to the variation of q_{TIR} with mass, it is difficult to disentangle the two relations and say whether the variation with mass causes the non-linearity or vice versa, as our sample is not complete in L_{TIR} (we consider

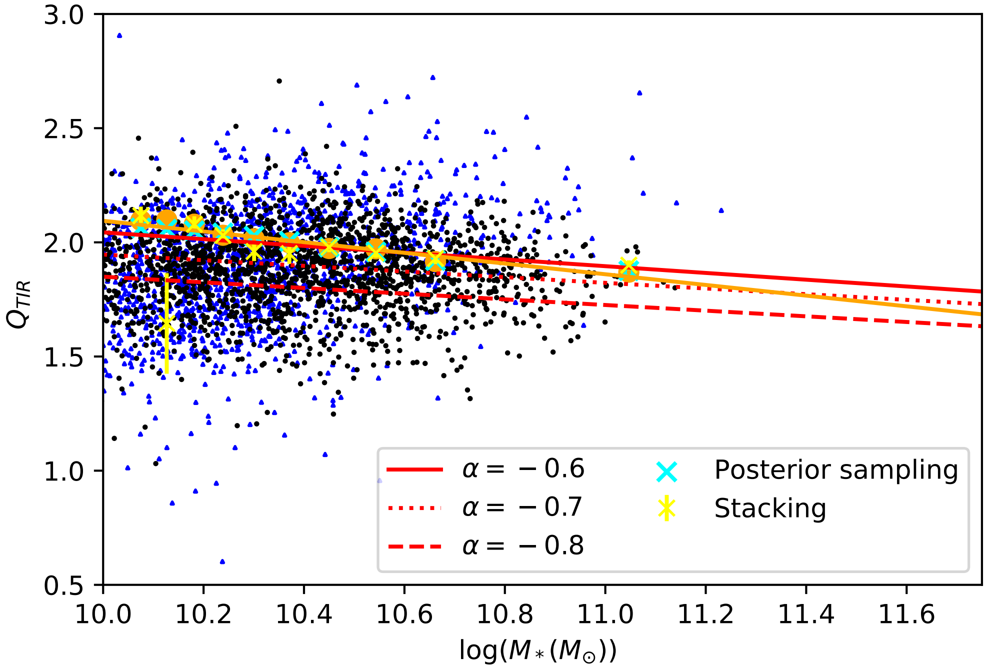

Figure 3.9: Variation of the FIRC at 150MHz with stellar mass for our mass sample. The blue points are upper limits of radio luminosity (lower limit on q) and the black points are for direct detections. The orange points are the median q_{TIR} measured using survival analysis in each stellar mass bin and the orange line is the linear fit to those points. The light blue crosses are the median q_{TIR} within each bin measured using the method described in Smith et al. (2021), while the yellow points are the median q_{TIR}s measured with stacking. The red lines are the linear fit from Eq. 6 of Delvecchio et al. (2021) at the median redshift of our sample converted to 150MHz with three spectral indices (see legend).

this in more detail below). Smith et al. (2021) found a non-linear relation between SFR and L_{150} (Eq. 1 in their paper) with slope 0.945 ± 0.07 (when substituting SFR with L_{TIR} and converted to the same form as our relation). While the slopes are $> 5\sigma$ apart, the difference can be attributed to the assumption that $L_{TIR} \propto SFR$. Any slight deviations from this assumption would cause a difference in the slopes between our work and that of Smith et al. (2021). In addition, we find a shallower slope than that observed by Wang et al. (2019) who found a slope of 0.77. However, their sample was constructed from IRAS-detected galaxies across the *Hobby-Eberly* Telescope Dark Energy Experiment (HETDEX) region ($\sim$400deg^2) that by construction will be bright in the IR and have a median redshift of $\sim$0.05. It is hard to match their sample selection as we have few galaxies with such a

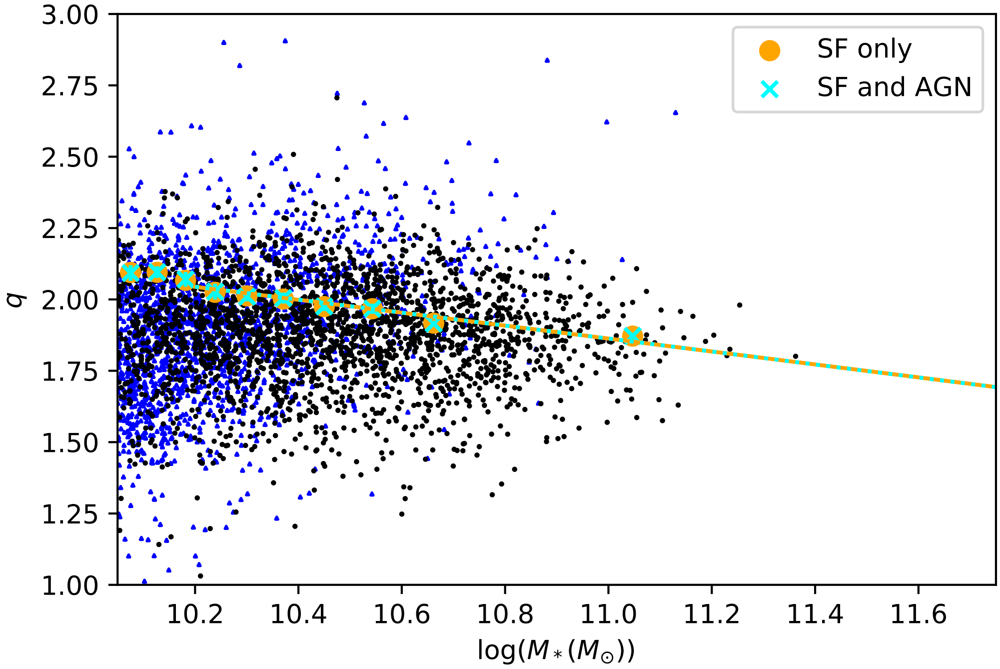

Figure 3.10: Variation of the FIRC at 150MHz with stellar mass for our mass sample. The blue points are upper limits of radio luminosity (lower limit on q) and the black points are for direct detections. The orange points are the median q_{TIR} within each stellar mass bin measured using the survival analysis on only SF galaxies, and the orange line is a linear fit to these medians. The light blue crosses and line are the same but when AGN are included in the sample. We note how the blue crosses overlap with the orange points.

low redshift because of the smaller area covered by the LoTSS observations in ELAIS-N1.

3.6 Discussion

Here we present our results in the context of past studies (section 3.6.1), how our sample selection and assumptions affect the observed variation of q_{TIR} with stellar mass (section 3.6.2), whether or not the FIRC being non-linear at 150MHz is consistent with the main sequence (section 3.5.3), and the causes for the dispersion around the FIRC (section 3.6.4).

3.6.1 Comparison with past measurements

Our results have a similar normalisation to those of Delhaize et al. (2017) (study done in COSMOS at 3GHz) but show a shallower evolution, which is likely caused by the observed evolution in stellar mass that results in galaxies with lower stellar masses having higher

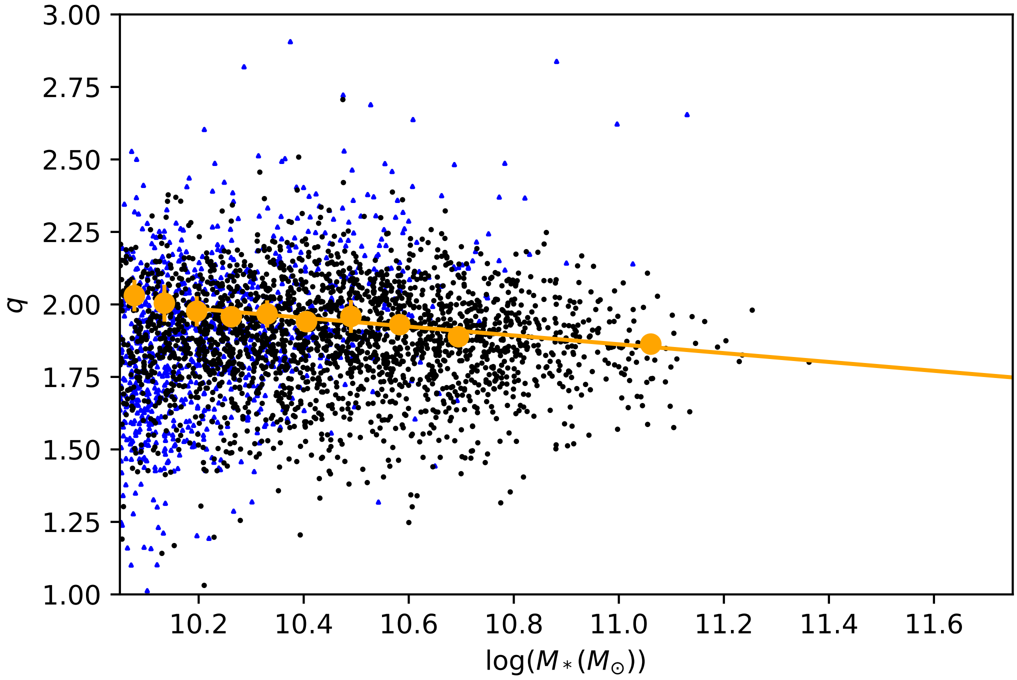

Figure 3.11: Variation of the FIRC at 150MHz with stellar mass for our mass sample. The blue points are upper limits of radio luminosity (lower limit on q) and the black points are for direct detections. The orange points are the median q_{TIR} within each stellar mass bin measured using the survival analysis on only SF galaxies, and the orange line is a linear fit to these medians. The errors have be corrected by a factor of $\sqrt{1000}$ to account for the correlations between the bootstrapped samples.

q_{TIR}. The sample used by Delhaize et al. (2017) did not have a cut in stellar mass, and so they would expect to see higher q_{TIR} values at low redshift, where low-mass galaxies are observable and conversely lower q_{TIR} at high redshift. This would explain their apparently stronger evolution with redshift. Similarly, Calistro Rivera et al. (2017) did not use a mass-complete sample. This similarly biased their results towards lower q_{TIR} values and explains the majority of the differences between our results and theirs. We can directly confirm this by modifying our sample to match the selections used in Calistro Rivera et al. (2017). To do so, we only included galaxies with a peak flux at 150MHz > 0.6mJy and then reran the analysis described in section 3.5.2, with $\alpha_{150}^{1400} = -0.63$; the results are shown in Figure 3.13. Using a radio-selected sample brings us into much better agreement with Calistro Rivera et al. (2017). In conclusion, the evolution in redshift observed in most other studies appears to be a result of their incomplete sample selection with respect to stellar mass.

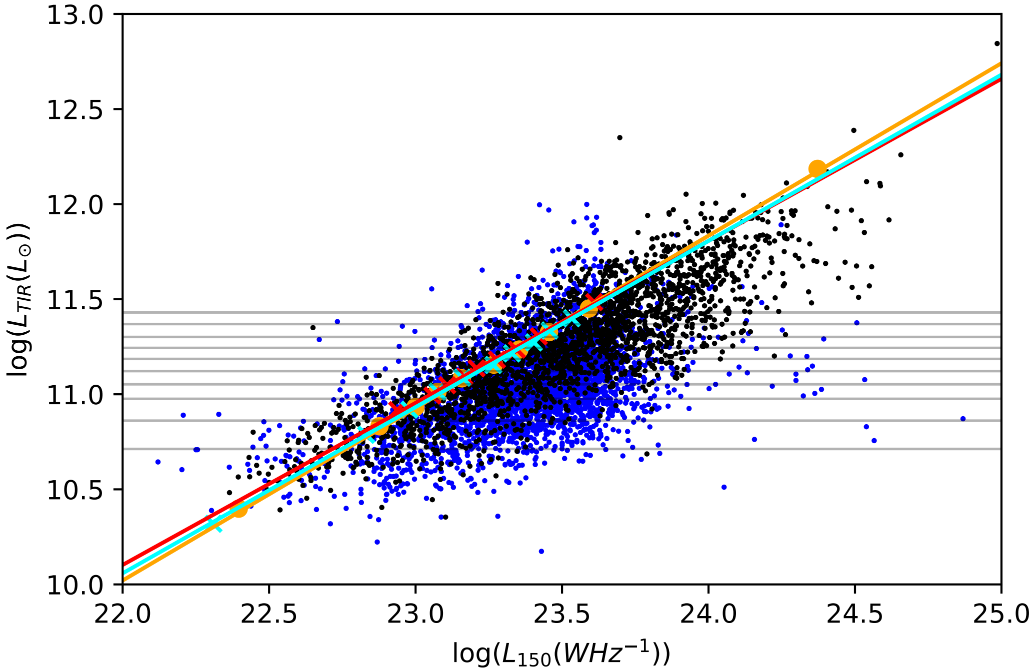

Figure 3.12: Total-infrared luminosity ($8 - 1000\mu$m) measured using MAGPHYS vs. radio luminosity at 150MHz for all galaxies. The horizontal lines show the bins that the galaxies were divided into such that each bin contains an equal number of galaxies. The orange points are the median q_{TIR} measured using survival analysis in each L_{TIR} bin and the orange line is the linear fit to those points (we note that the orange points are often behind the cyan and red crosses). Blue data points are upper limits on radio luminosity and black points are direct detections at 150MHz. The red line is the linear relation we would expect if our galaxies followed the main sequence measured by Schreiber et al. (2015) and the light blue line is that expected if they followed the main sequence measured by Leslie et al. (2020).

This contrasts with the results of Delvecchio et al. (2021) (Figure 3.9), who used a mass-complete sample measured at 3GHZ and then corrected to 1.4GHZ with $\alpha^{3}_{1.4} = -0.75$, showing relatively little evolution with redshift but a clear dependency on stellar mass. These authors found good agreement between their sample and the results of Delhaize et al. (2017) when considering high-redshift galaxies. These are dominated by high-mass galaxies, and so the sample used in Delhaize et al. (2017) is close to the mass-complete one used in Delvecchio et al. (2021). Meanwhile, we found a steeper relation between q_{TIR} and stellar mass and a higher normalisation than Delvecchio et al. (2021). Our tests with the SIDES simulation showed that our use of the survival analysis is able to accurately recover the true relation of our sample. So, unless some of the underlying assumptions used in our work are incorrect (such as choice of spectral index, which is examined in the following section) then we are confident that the differences are caused by the different frequencies used in our works. We expect to have a different ratio of thermal to synchrotron emission at the respective frequencies of our study and that of Delvecchio et al. (2021), and these differences could result in a different normalisation and slope.

Finally, Figure 3.7 shows a reasonable agreement between the median q_{TIR} of our redshift sample and that of Molnár et al. (2021). Their sample was constructed from low-redshift SDSS galaxies at 1.4GHz, and so some differences are expected. We converted their median to 150MHz using a spectral index of -0.73 and a higher spectral index would also explain the difference (see the following section for a more in-depth discussion on the choice of spectral index).

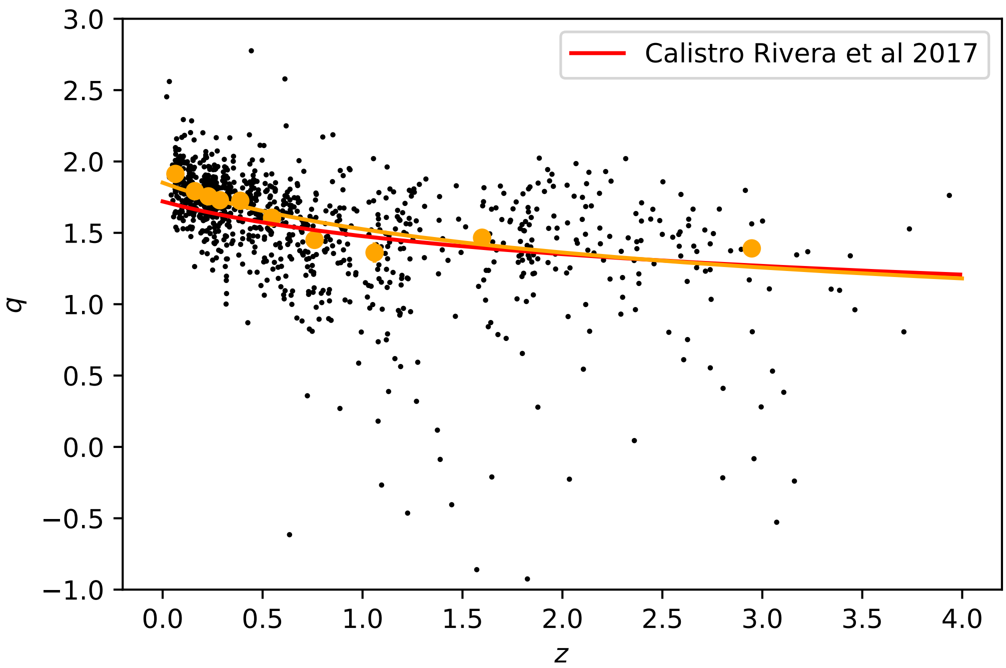

Figure 3.13: Evolution of q_{TIR} with redshift only using radio sources with peak flux > 0.6mJy to mirror the sample selection of Calistro Rivera et al. (2017). We note the improved agreement between our fit (orange line) and the fit from Calistro Rivera et al. (2017) (red line) compared to using a mass-complete sample (Figure 3.8)

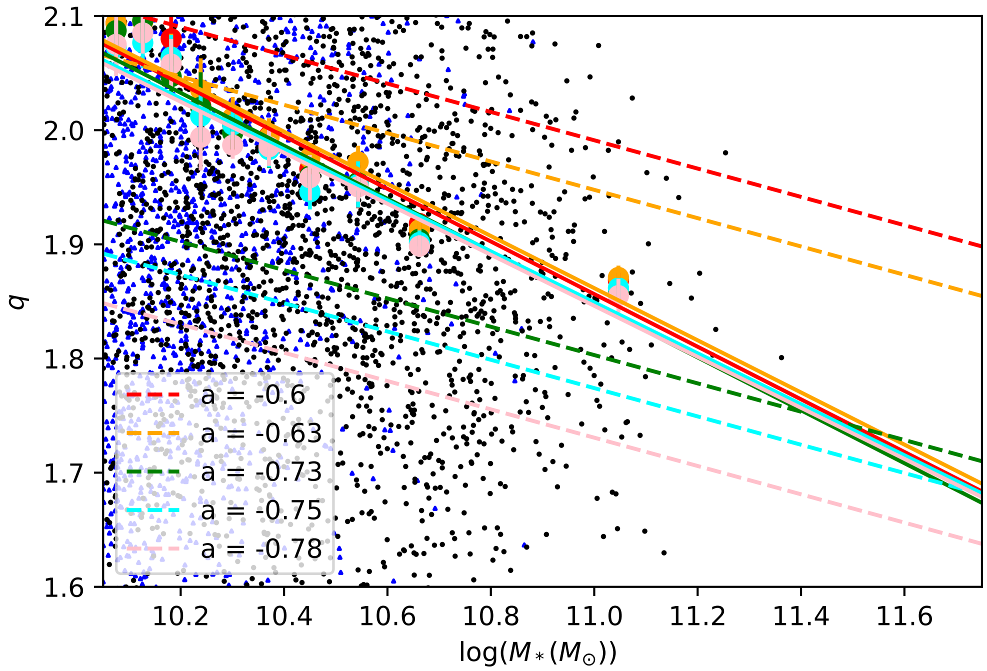

Figure 3.14: Effect of different spectral indices on the linear fit of the FIRC with stellar mass and how our fits compare to those of Delvecchio et al. (2021). The solid lines show our relation depending on the choice of spectral index (see legend) and the dashed line shows the fit from Delvecchio et al. (2021) when converted to 150MHz with the same spectral index. The black points show galaxies that are detected at 150MHz and the blue points show galaxies that have upper limits on there flux at 150MHz. The large coloured points show the median q in each stellar mass bin depending on the chosen spectral index used.

3.6.2 Mass evolution robustness

Our results are based on several choices and assumptions made during our analysis and sample selection. Here we examine how changing those assumptions affects our results, focusing on: choice of spectral index, different FIR versus radio depths, removal of AGN, and selection of SF galaxies.

We used the spectral index measured in Calistro Rivera et al. (2017) of $\alpha_{150}^{325} = -0.60 \pm 0.05$, the mean of a Gaussian fitted to the observed distribution. Alternatively, we could have taken the mean of the distribution itself (-0.63), but Figure 3.14 shows that the choice of spectral index makes little difference to the normalisation of our measured relation and no difference to the slope (solid lines). This is due to the small redshift range that our stellar mass sample was constructed in ($z < 0.4$), meaning that any correction to the rest

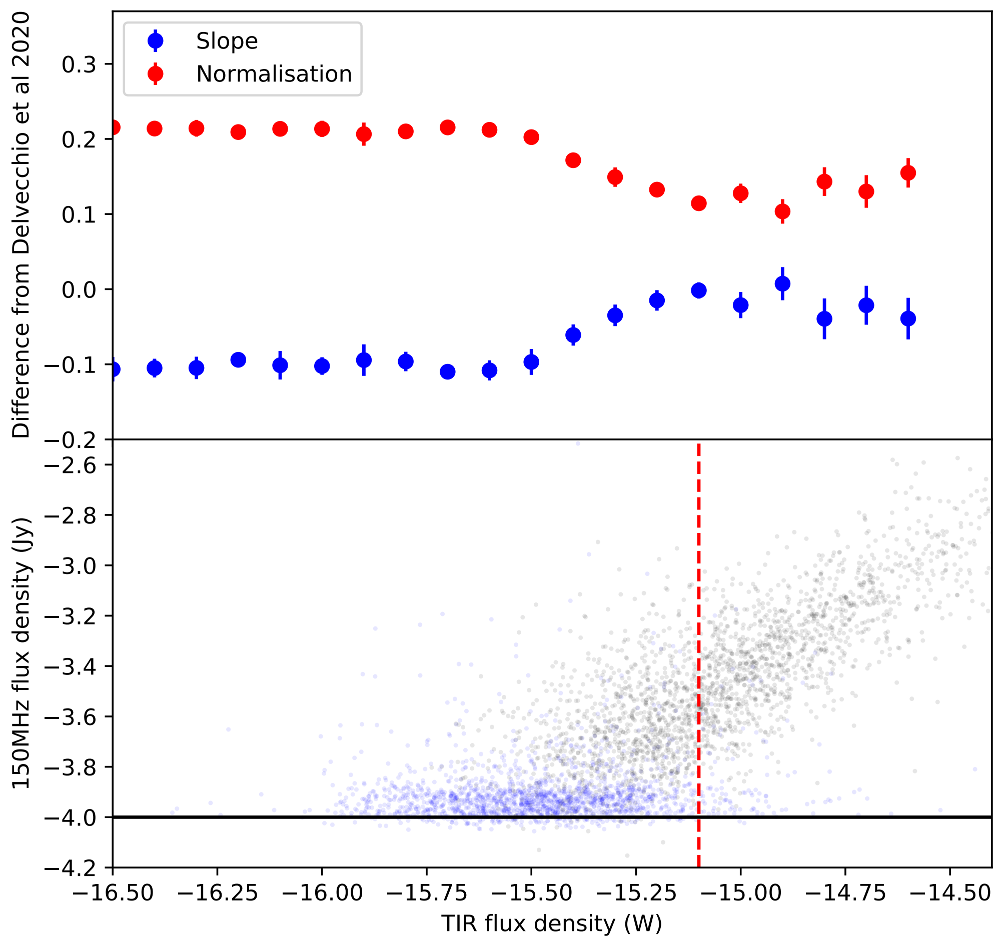

Figure 3.15: Top: Difference of linear fit parameters compared to Delvecchio et al. (2021) depending on the limit applied to the TIR flux. The red and blue points show the normalisation and slope of the linear fit, respectively, for all galaxies with a TIR flux density to the right of the point. It can be seen that imposing increasingly strict cuts on the TIR flux density does not cause any significant bias in our results and does not explain the difference between our fit and that of Delvecchio et al. (2021) until the TIR flux cut starts to significantly cut into our radio-detected galaxies. Bottom: TIR flux density calculated by dividing the TIR luminosity by $4\pi D_L^2$, against flux density at 150MHz. The black points are galaxies that are detected at 150MHz and the blue points are galaxies with an upper limit at 150MHz. It can be seen that the limit at 150MHz ($\sim 100\mu$Jy) has a greater effect on our sample than the limits of the TIR flux.

frame frequency will be minor even at $z = 0.4$. However, when comparing to Delvecchio et al. (2021), the choice of α_{150}^{1400} has a big impact on the difference in normalisation between our results. We used $\alpha_{150}^{1400} = -0.78$ as it is the mean of the α_{150}^{1400} distribution measured in Calistro Rivera et al. (2017). These latter authors also fit a Gaussian to the spectral index distribution with a mean of -0.73. Regardless, even if we use the higher spectral index we still find that their $q_{1.4} = 2.53$ becomes $q_{150} = 1.82$ which is still 0.2 dex below our results and can only explain 0.07 dex of the difference. Alternatively, Calistro Rivera et al. (2017) show α_{150}^{1400} as a function of redshift and find a large variation at low redshift, with results varying between -0.85 and -0.59 for z<0.5. Taking the highest spectral index would put our results and those of Delvecchio et al. (2021) in good agreement (shown in Figure 3.9). In addition, we investigated whether the different choices of spectral index used to convert to rest frame frequencies of 150MHz and 1.4GHz respectively could account for the difference. We converted their relation back to the observed frequency of 3GHz using their assumed spectral index of -0.75 and then reconverted to 1.4GHz. The subsequent conversion from 1.4GHz to 150MHz and converting our results from the observed frame to 150MHz were all done with the same spectral index and the results can be seen in Figure 3.14. This shows that the choice of spectral index only has a minor effect on the normalisation of our fit, which is to be expected due to the low redshift of our stellar mass sample. However, if the spectral index is closer to -0.6 then our normalisation would be in better agreement with that of Delvecchio et al. (2021). Overall, we are confident that varying α_{150}^{325} within reasonable values has little to no impact on our measured relations but the choice of α_{150}^{1400} does greatly affect comparisons with work done at higher frequencies.

Next we consider the difference in FIR versus radio depth. Our sample is created from an IRAC-selected sample and then limited to a mass-complete sample of star-forming galaxies. As the measurements of IR luminosity are done using MAGPHYS and an energy balance, there are many galaxies with a TIR luminosity measurement that are not detected in any individual FIR bands. This makes our sample deeper in the IR than the radio, in contrast to the sample used by Delvecchio et al. (2021) whose radio data were deeper than their IR data. We investigated whether this difference in depths could explain the measured discrepancy between our results. This was done by imposing a cut on the IR flux (calculated dividing the IR luminosity by $4\pi d_L^2$) and then increasing this cut over a range of 2.0 dex. The greatest change in normalisation was ~ 0.1dex, obtained by imposing a harsh cut in our sample (Figure 3.15) that has no physical motivation. In addition, such a harsh cut in TIR flux would likely be introducing significant bias towards lower q_{TIR}

values. Finally, it is worth emphasising that the maximum effect this can have on the normalisation of our linear fit is to decrease it by ~ 0.1dex which still leaves us with a significant disagreement with Delvecchio et al. (2021) when taking the nominal value of $\alpha_{150}^{1400} = 0.73$.

We consider the impact that removing AGN has on our results. We remeasured the evolution of q_{TIR} with stellar mass but with AGN host galaxies included in the sample (all AGN were re-added to the sample) to see how they affect our results (Figure 3.10). We can see that the inclusion of AGN does not significantly affect our results. This is due to the fact that we are fitting to the median q_{TIR} within each redshift or stellar mass bin and so we are not as affected by outliers or the relatively low fraction of AGN within our sample ($< 10\%$). The galaxies with the lowest q_{TIR}values are potentially unidentified radio-loud AGN or galaxies with a low dust mass (and therefore the TIR luminosity does not map the full SFR).

Finally, we investigated the impact of how we remove passive galaxies from our sample. Both our mass sample and redshift sample define a passive galaxy as one that is more than 0.6 dex below the main sequence. This offset below the main sequence was chosen to match $\simeq 2\sigma$ where σ is the dispersion in the main sequence. However, choosing to set the offset between 0.3 and 0.9 dex would be equally justified. We investigated the effect that changing this offset has on our results and found that the slope and normalisation of the linear fit to $q_{TIR}(M_*)$ vary by 0.02 and 0.01 respectively. The change in normalisation is the same as our uncertainty on the normalisation and the variation in slope is only marginally greater than our uncertainty. While varying our SF galaxy criteria does have a minor impact on the measured relation, the impact is similar to the random error of our measured distributions.

3.6.3 Main-sequence prediction of FIRC

The SFR of a galaxy is known to be correlated with its mass and this MS has been observed many times (Schreiber et al., 2015; Leslie et al., 2020). For a given galaxy in our redshift sample, we know its radio luminosity (or upper limit), mass, and redshift, and so we are able to calculate its predicted SFR using the MS relations measured in Schreiber et al. (2015) and Leslie et al. (2020) and therefore its TIR luminosity using the relation from Kennicutt, Jr. (1998). We can then bin our galaxies on their predicted TIR luminosity so that there is an equal number of galaxies in each bin. In each bin, we can compute the median q_{TIR} using a survival analysis and see how we would expect the slope of the

FIRC to vary based purely on predictions from the MS relations. We can see from Figure 3.12 that the predicted non-linearity is in agreement with our observed non-linearity. This could imply that the physics causing the observed non-linearity is the same that causes the MS. This in turn could help calibrate the SFR–radio luminosity relation. However, if the relation between SFR and stellar mass, which in turn causes a change in TIR luminosity, results in a change in the relation between radio and TIR luminosity, we would expect the radio luminosity to be similarly affected, but this does not seem to be the case. Resolving such issues is beyond the scope of this work. However, we hope to address such topics in the near future.

3.6.4 FIRC dispersion

A little-explored property of the FIRC is the cause for the dispersion. While the FIRC is surprisingly linear, with the standard deviation being 0.2, q_{TIR} values still span a range of 1.5 dex when considering only the detected galaxies. Understanding what affects the deviation of a galaxy from the median q_{TIR} can provide some insight into the underlying physics behind the FIRC. For high-mass galaxies, stellar mass does affect the median q_{TIR}, and it could also affect the dispersion. These galaxies are most likely to have low-level AGN emission (Sabater et al., 2020) and a large low-mass stellar population. Either of these could boost the radio or FIR emission of the galaxy through mechanisms that are unrelated to SF. Other parameters that could affect where a galaxy lies on the FIRC are SFR and sSFR, as the mechanisms governing the FIRC may begin breaking down for starburst galaxies (though this was not observed by Magnelli et al. (2015) or predicted by Lacki et al. (2010)). Finally, the steepness of the radio spectrum is indicative of how recent the SF in a galaxy has occurred and may cause a galaxy to lie off the FIRC as the FIR and radio may be less sensitive to SF that has occurred more or less recently.

In order to investigate for this effect, we also included proxies for the angular and physical size of the galaxy. These were taken as the ratio of the total radio flux divided by the peak radio flux and as the difference in magnitude in the r band between 1-2, 1-3, and 1-6". These proxies for angular size were converted to a measure of physical size by multiplying them by the distance to the galaxy. Finally, a proxy for gas surface density was created by dividing SFR by physical size as this is one of the key parameters used in Lacki et al. (2010). All of these parameters were fed into a neural network to predict the difference between a galaxy's q_{TIR} value and the median q_{TIR} (Δq). We found that the neural network had no significant ability to predict Δq when compared to the intrinsic scatter of the Δq distribution.

The lack of predictive power of the neural network could be caused by several factors. Firstly, the parameters that govern the radio and FIR emission, such as magnetic field strength, are difficult to directly measure. Without a way to proxy these measurements, it is difficult to constrain exactly the q_{TIR} value that a given galaxy should have. In addition, the measurements of SFR from MAGPHYS measure the combined SFR detected in the UV, optical, and FIR. If the measured SFR is imperfect because of the dust geometry of the galaxy, then the galaxy may lie off the FIRC.

Further work is required to explain the scatter in the FIRC. We are unable to accurately assess the error in L_{TIR} caused by unusual dust geometry. In addition, we have no measure of the radio spectral index, which may explain a portion of the scatter.

If some of the SFR is unobscured, either due to lower-than-expected dust mass or the geometry of the galaxy, then the galaxy may not lie on the FIRC and we would be unable to measure this from the features we provided to the neural network.

3.7 Conclusions

In this work, we measured FIR fluxes for all radio sources in the LoTSS deep fields. These fluxes were then used to derive the FIRC at 150MHz using data from LoTSS (Shimwell et al., 2019) and *Herschel* (Oliver et al., 2012) used in combination with a mass-complete sample (Kondapally et al., 2021; Duncan et al., 2021) of star-forming galaxies to measure the FIRC. The TIR luminosity is measured using MAGPHYS (Da Cunha et al., 2008), which uses energy balance to infer the IR luminosity when FIR fluxes are not measured, enabling IR luminosity measurements for all galaxies in our sample. To account for non-detections in the radio and FIR we use survival analysis and upper limits on the radio flux for galaxies that are undetected at 150MHz. We investigate the evolution of q_{TIR} with redshift and stellar mass and compare to the recent results from Delvecchio et al. (2021) using the JVLA. Our main results are listed below.

1. We measured fluxes at 24, 100, 160, 250, 350, and 500μm for 79609 galaxies across the LoTSS deep fields. In addition, we provide flags to identify sources whose flux is unreliable. The flags are based on the goodness of fit of the flux posterior to the map and whether it is dominated by the prior. The fluxes are available in the LOFAR deep fields data release (column descriptions can be found at https://github.com/H-E-L-P/dmu_products/tree/master/dmu26).

2. We validated our methods by creating a simple model based on galaxies created as part of the SIDES simulation (Béthermin et al., 2017). Radio luminosities were added to star-forming galaxies by generating q_{TIR} values from a Gaussian distribution, whose mean evolved as a power law that mimicked the observed distribution from our mass-complete sample. We determined whether a galaxy would be detected in the radio or not. We found that we were able to recover the true distribution parameters (the true mean and power-law parameters) from the simple model when we had more detected galaxies then undetected galaxies (at 150MHz).

3. The FIRC was measured at 150MHz with a mass-complete sample of star-forming galaxies. We also examined the evolution of q_{TIR} with redshift and stellar mass, finding a power-law relation for both, of the form $q(z) = 1.94 \pm 0.01(1+z)^{-0.04\pm0.01}$. Similarly the evolution with stellar mass was found to have a linear relation, of the form $q(M_*) = (2.00 \pm 0.01) + (-0.22 \pm 0.02)(\log(M_*) - 10.05)$.

4. Comparing with previous results we found a significant difference between our evolution with stellar mass and that of Delvecchio et al. (2021). Neither our different treatment of AGN nor the different radio versus FIR depths can explain the difference. However, our choice of spectral index from Calistro Rivera et al. (2017) could affect our result as we used the median $\alpha_{150}^{1400} = -0.78$ instead of $\alpha_{150}^{1400} = -0.59$ which was observed at low redshift. More work is needed to better understand the radio spectra in order to know whether or not using a higher spectral index would explain the discrepancy between our results. We also observe a significant difference between our redshift evolution and that of Calistro Rivera et al. (2017). However, this can be explained by our different sample selections.

5. We investigated the non-linearity of the FIRC at 150MHz and found that $L_{TIR}(M_*) = (0.90 \pm 0.01)L_{150} - 9.8 \pm 0.3$. This relation is in good agreement with that found by Smith et al. (2021) in the SFR–radio luminosity plane and Molnár et al. (2021) at 1.4GHz. In addition, the non-linearity observed agrees with predictions from the MS (Schreiber et al., 2015; Leslie et al., 2020). Future work is needed to explore whether both relations originate from the same physical processes.

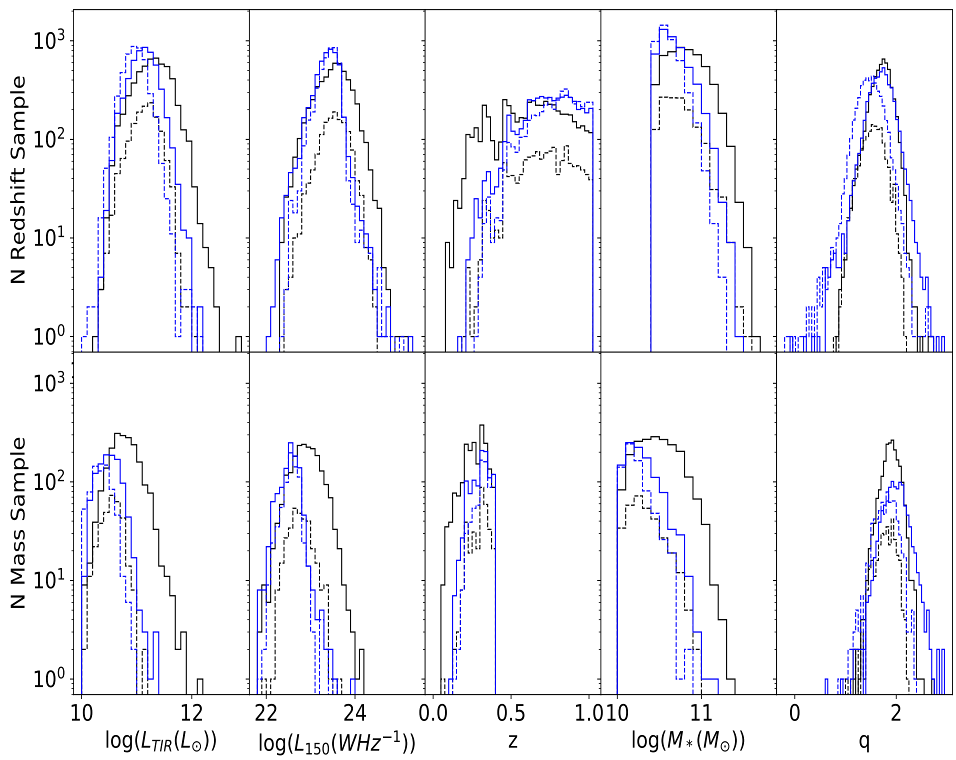

Figure 3.16: How galaxies are distributed, split by their observed fluxes and which sample they are in. The black line shows how the galaxies that are detected at 150MHz are distributed and the blue line is for galaxies undetected at 150MHz. If the line is dotted then it shows galaxies that have one unflagged (see section 3.2.3) flux from PACS or SPIRE and if solid then it has more than one unflagged flux from PACS or SPIRE. We can see that in no part of parameter space are we dominated by galaxies that have one or less unflagged flux in PACS or SPIRE.

3.8 Appendix

3.8.1 Energy Balance Assumption

Using the SED fits from Smith et al. (2021) we are relying on the energy balance approach used by *magphys* when there are no PACS or SPIRE fluxes to help constrain the FIR. Firstly, Figure 3.16 shows that in no part of parameter space are we dominated by galaxies that are dependent on the energy balance, so the affect of any systematic bias, if any exist, would be minimal. As a second check we can compare the νL_ν at 24μm with the SFR measured from *magphys*. νL_ν at 24μm is a tracer of SF Rieke et al. (2004) so by

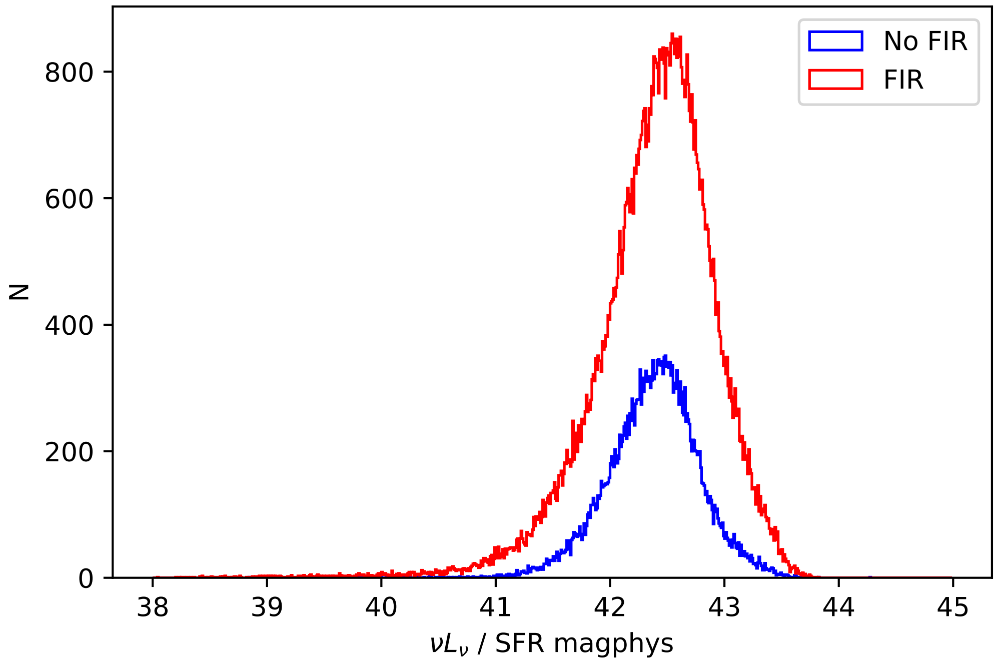

Figure 3.17: Comparison of νL_ν/SFR measured from *magphys* for the 3.6μm selected sample in ELAIS-N1. The blue histogram shows the results for galaxies with one or less unflagged flux from PACS or SPIRE while the red histogram shows the results for galaxies with more than one unflagged flux from PACS or SPIRE.

comparing their ratio for different sub samples we can see whether there are any significant deviations in this ratio between the subsamples. To calculate νL_ν at 24μm we k corrected the measured L_ν using the red galaxy template from Berta et al. (2013). Figure 3.17 shows the comparison between galaxies with one or less detection from PACS or SPIRE compared to galaxies with more than one detection. We can see that the peak of both distributions are within $\simeq$ 0.2dex of each other, lending further evidence that relying on the energy balance from *magphys* does not cause a bias in measurements of SFR (and hence TIR luminosity as the two are tightly correlated). The small offset is likely caused by faulty choice of SED template for the k correction. The subsample with few FIR detections are more likely to be fainter galaxies or at higher redshift and a different template may be needed to accurately measure their νL_ν at 24μm.

Chapter 4

FIRC as a prior for measuring 150MHz and FIR fluxes

In this thesis I have shown how radio catalogues can be crossmatched to optical/NIR catalogues (Chapter 2) and then how this can be used to improve the prior for XID+ (Chapter 3). However, this method presents a couple of problems:

- Galaxies within our sample for the FIRC (Section 3.4.1) that are undetected in the radio, forcing us to rely on upper limits of the radio luminosity that do not utilise the data available to us from the radio image.
- Biases from XID+ measurements of FIR fluxes towards splitting the flux equally between sources.

Our use of survival analysis in Chapter 3 was necessitated by lacking any measurement of the flux from galaxies within our sample that were not included in the LOFAR catalogue. While our simulations showed that survival analysis was able to recover the true evolution parameters of our sample I also found that the correct answer was recovered when our upper limits on a galaxy's flux were calculated from random pixels, rather than the pixel the galaxy was located in. This indicates that survival analysis is making use of the error distribution of the LOFAR map rather than flux from each individual galaxy (even if the flux doesn't have a SNR above 5). Similar results were found when treating the individual pixels as Gaussian posteriors with the final results being independent of the pixels used. What would be ideal is to model the flux from our undetected galaxies using the PSF of the LOFAR map while modeling the background. This would avoid negative fluxes, which were possible when treating the flux posterior as a Gaussian whose mean and standard deviation were determined by the pixel value and error.

In cases where two sources in our prior list for XID+ were within the same pixel the solution becomes degenerate, with XID+ preferring to split the flux between the sources rather than assign the majority to one source. With the current data available to XID+ this is the best it can do. However, I know that TIR luminosity and radio luminosity are correlated so this information could be used to break the degeneracy in the FIR fluxes.

In this chapter I will discuss how expanding XID+ to run on the FIR and radio maps simultaneously can be used to measure the FIRC and provide better constraints on the individual galaxy's FIR and radio fluxes. I will start by describing how XID+ works in detail. Next I will show the work I have done to extend XID+ to run on the LOFAR map. Finally I will discuss the expanded hierarchical model needed by XID+ to measure the FIRC, FIR and radio fluxes.

4.1 XID+

XID+ has been discussed in this work already and a brief description of how it works can be found in Section 3.2.3. Here I will describe in detail how the model XID+ uses is constructed as well as how the parameters for the model are measured.

4.1.1 Bayes Theorem

Bayes theorem is a probability law discovered by the Reverend Thomas Bayes in 1763 that is used to calculate the probability of an event happening given the occurrence of a separate event. This can be generalised to calculate the probability of a model (θ), where θ represents the model itself as well as the parameters that make it up, given a vector of data ($\mathbf{D}$)

$$P(\theta|\mathbf{D}) = \frac{P(\mathbf{D}|\theta)P(\theta)}{P(\mathbf{D})}, \tag{4.1}$$

where $P(\theta|\mathbf{D})$ is the posterior probability, $P(\mathbf{D}|\theta)$ is the likelihood of our data occurring given our model, $P(\theta)$ is the prior probability of our model and model parameters and $P(\mathbf{D})$ is the evidence. The prior is the probability of our model occurring. In this case the model refers to both the general form of the model as well as the parameters that make up the model, such as the mean and standard deviation. By form of the model we refer to the equations used to describe the data. For example if we measured the heights of 10,000 men we could model this as a Gaussian or log normal distribution. Our prior could be uniform if we have no preference between the two distributions or could be used to prefer a Gaussian distribution over a log normal. Our prior may explicitly state the allowed values for the model's parameters (we may know that the mean is positive) as well as implicitly state that the probability of certain models is zero (we may implicitly state that our data is represented by a normal distribution only by not considering other distributions). The evidence is normally not calculated as with a fixed dataset $P(\mathbf{D})$ is constant and we can simplify Bayes Rule to

$$P(\theta|\mathbf{D}) \propto P(\mathbf{D}|\theta)P(\theta) \tag{4.2}$$

so that to find the ideal model and model parameters we only need to compare the likelihood multiplied by the prior. Finally the likelihood is calculated by selecting parameters for our model, in the example of a normal distribution this would be the mean and standard deviation, and then compare our observed data to the predicted results. We repeat this process, selecting different parameter values each time, until the difference between the observed data and the model predictions is minimised (how the model parameters are selected is discussed in the next section).

4.1.2 Posterior Sampling

We have seen that Bayes theorem gives us a way to find the probability distribution of a model and model parameters to explain our data. However, to do this we need to evaluate our likelihood at different parameters values to effectively explore the posterior of our model parameters. To do this there are several methods we can use. The simplest method is to simply create a grid of parameters and evaluate the likelihood at each of the grid points. However, this method becomes computationally impossible when dealing with complex models with a large number of parameters. Instead we can use Markov Chain Monte Carlo (MCMC). The principle behind this is that a number of walkers are initiated at some random part of the parameter space. Each walker then takes a step in parameter space in a random direction and evaluates the likelihood at its location. It then decides whether to remain at this new point or to return to the old point. How this decision is made varies depending on the exact MCMC algorithm used. For example the Metropolis algorithm makes this decision based on the ratio of L_{new}/L_{old}, where L is the Likelihood. If $L_{new}/L_{old} > 1$ then the new location is accepted and if $L_{new}/L_{old} < 1$ then the probability of accepting the step is inversely proportional to the ratio. A key parameter of the Metropolis algorithm is the step size. If the step size is too large then depending on the shape of the posterior some details may be missed. If too small then sampling the posterior will take too long. At the end of the MCMC algorithm the chains are combined to create a map of the posterior (the likelihood multiplied by the prior)

An alternative MCMC algorithm is Hamiltonian Monte Carlo (HMC). This works on the same principle as described above, however, it has a few key differences. The first is that HMC uses the likelihood and the gradient of the likelihood to decide on the direction to move each chain. It also uses the gradient to help adjust the step size. This allows the algorithm to quickly move to regions of interest in the posterior.

It is worth noting that not all MCMC algorithms use the gradient of the likelihood. For example, emcee uses the position of all the other walkers to update the position for an individual walker.

4.1.3 XID+ model

XID+ is a Bayesian probabilistic deblending software designed to measure the FIR flux from sources (Hurley et al., 2017). This is done by modelling the FIR maps as a combination of flux from sources, instrumental and confusion noise using the following model

$$\mathbf{d} = \sum_{i=0}^{N} \mathbf{P} f_i + N(0, \sigma_{instrumental}) + N(B, \sigma_{confusion}), \tag{4.3}$$

where $\mathbf{d}$ is the map, N is the number of sources, $\mathbf{P}$ is the PSF of the telescope, f_i is the flux of the ith source and σ is the instrumental and confusion noise. In practice the PSF is gridded into a higher resolution grid than the map (for SPIRE images a 1 arcsecond grid is used) and then the contribution of each source to the nearby pixels is calculated by interpolating this PSF grid. In the map the noise in nearby pixels is correlated, however, modelling this effect would require calculating the entire $m \times m$ matrix (where m is the size of the map in pixels). This would significantly increase the computational time so instead the noise is treated as constant across the map.

4.2 XID+ radio extension

Here I will set out how the LOFAR images are created and how XID+ needs to be modified to function on these images.

4.2.1 LOFAR image creation

To extend XID+ to work on the LOFAR image we need to understand the differences between the LOFAR image and the FIR images that it was designed on. Creating the LOFAR image from all the signals received by the LOFAR antennae across all LOFAR stations is a complicated process that is unnecessary to fully understand. What we need to know is what makes up the finished image that XID+ will be running on. Once the LOFAR

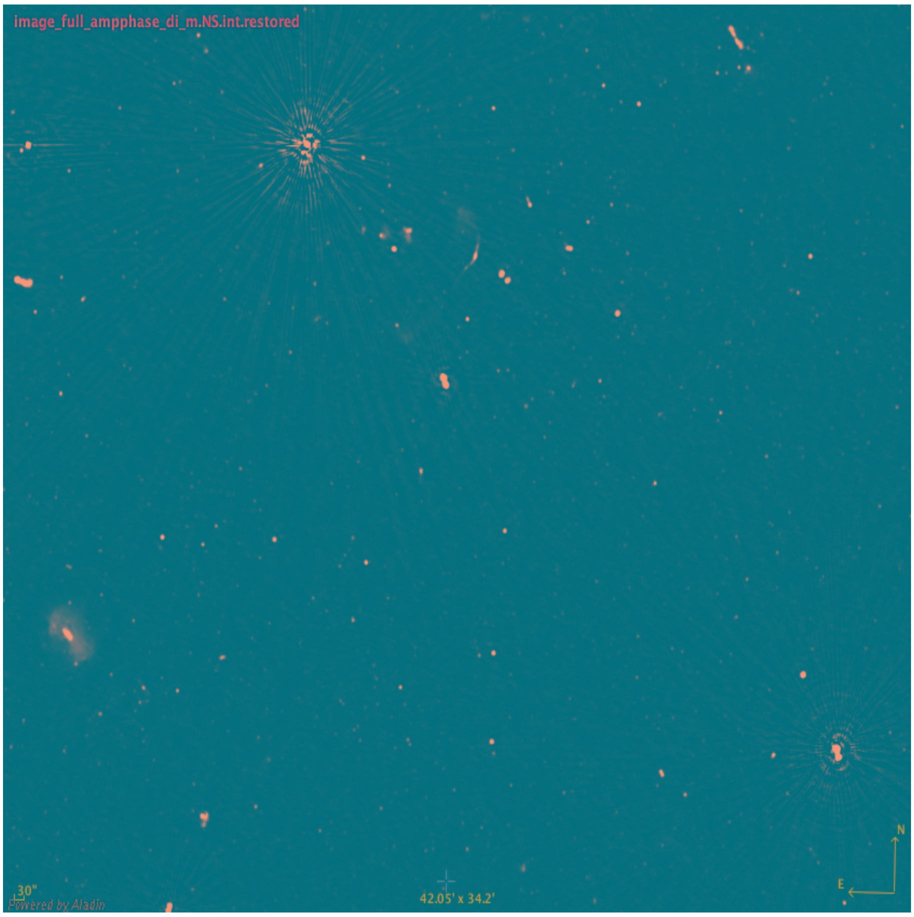

Figure 4.1: Cutout of the ELAIS-N1 LoTSS deep field image. Note the artifacts around the bright sources caused by slight inaccuracies when modelling the sky to create the image.

image is calibrated (Tasse et al., 2021) sources are deconvolved using CLEAN (HöGBOM, 1974). This deconvolution algorithm assumes that the image is built from multiple point sources that are convolved with the dirty beam. By looking for the brightest pixel in the image we can assign a source to that pixel of some brightness (typically 10% of the pixel's flux) and subtract its flux from the map, once it has been convolved with the dirty beam. This process is repeated until no pixel above a chosen threshold remain. Then all the removed sources are convolved with the ideal beam (normally chosen to be a Gaussian with FWHM calculated from Equation 1.15). This model image is then added to the leftover residual image giving the radio image that will be used for science. This means that some of the sources in the LOFAR map will be convolved with this ideal beam while others will be convolved with the dirty beam (Figure 4.1).

4.2.2 XID+ radio model

With the radio map being made up as a combination of sources convolved with the ideal beam and others with the dirty beam the first obvious change is that each source needs its own PSF. The second difference is that the assumption that the correlations in the error matrix are negligible is invalid. The dirty beam is large and complex (Figure 4.2) and bright sources can create artifacts in the surrounding region that increase the noise. These artifacts are caused by assumptions made to simplify the LOFAR image calibration, which would involve inverting a $N \times N$ matrix, to reduce the computational time but can cause inaccuracies when deconvolving the brightest sources. Additionally, any errors in measuring the dirty beam would causes artifacts when deconvolving the brightest sources. Fainter sources would have the same artifacts but they will be fainter than the background. However, I have not been able to account for these correlations due to computational constraints. But this is something to consider when interpreting our results.

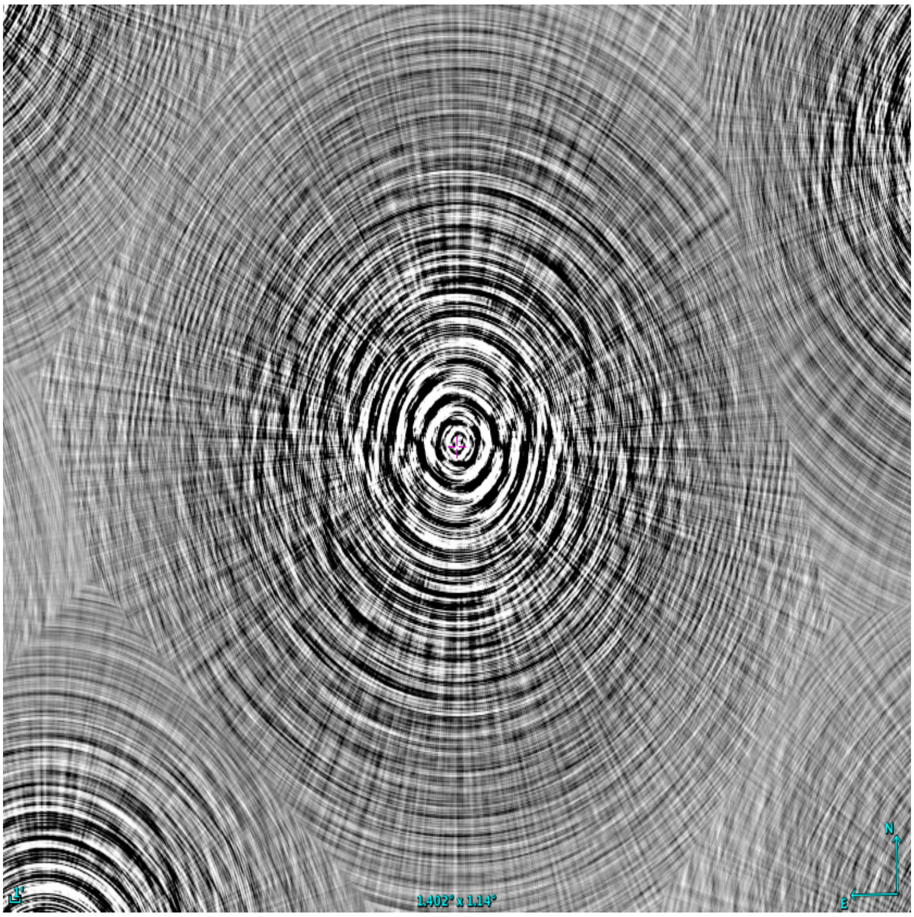

Figure 4.2: Cutout of the LOFAR dirty beam within one facet.

The biggest difference between the LOFAR maps and the FIR maps is the presence of extended sources. In the FIR maps, due partly to the low resolution of the images and the nature of FIR emission, nearly all sources can be considered to be point like and any deviations from this are minor. However, radio sources can be some of the most extended sources in the sky, especially outside of the local group. Modelling these sources in XID+ would either require adding more sources into the prior list or directly modifying the pointing matrix ($\mathbf{P}f_i$). Both methods present problems, adding sources into the prior list may be inaccurate as some extended radio emission is produced from a single source, such as radio jets. Such radio sources have been known about for decades and as such other software already exists to detect and measure the brightness of these sources (for example PyBDSF Mohan and Rafferty (2015)). Directly modifying the pointing matrix presents its own problems. To automate the process I would either need a model for the extended emission that I could parameterise, or iteratively modify the pointing matrix as part of the posterior mapping. A generic model for extended radio emission is extremely hard to create due to the huge range of shapes that radio jets can take. Iteratively modifying the pointing matrix would require running XID+ multiple times in the same region, which could quickly become computationally unfeasible depending on how complicated the source was. It would likely result in a large degeneracy between the form of the pointing matix and the flux of the source unless significant constraints were put into the form of the pointing matrix. With all these difficulties it is unlikely that XID+ will be able to accurately measure the flux of bright radio galaxies with extended emission. However, the majority of radio galaxies are near point like so this may not have a large effect. This is investigated in more detail later.

4.3 XID+ results

Here I detail how XID+ was run on the LOFAR deep field image in ELAIS-N1. First I ran the modified XID+ on the radio image from ELAIS-N1, using the radio catalogue created by PYBDSF as the prior list. I then ran XID+ with a prior list constructed of fake sources injected into the LOFAR map at random positions. In addition XID+ was run on the same prior list of fake sources without the sources being injected (so it is run on the image background). Finally I ran the modified XID+on the radio image from ELAIS-N1, using the entire ELAIS-N1 radio catalogue (created with PYBDSF) plus additional sources that have a high radio flux based on the FIRC. I then remeasured the FIRC using these results.

4.3.1 PyBDSF prior catalogue

To test the efficacy of XID+ I started by running XID+ on the ELAIS-N1 deep field image with the prior list constructed from the PyBDSF radio catalogues. These catalogues were constructed by fitting multiple Gaussians to peaks of radio emission in the map. The orientation, major and minor axis were varied in the Gaussian to obtain the best fit to the map. If multiple Gaussians were required to fit the observed emission then the Gaussians were grouped into one source if their centers were separated by less than half the sum of their FWHMs along the line joining them and there was continuous emission linking the two Gaussian centers. In these cases the source position was taken as the source centroid as determined by moment analysis. This essentially takes a weighted average of the source's pixels. I used both the catalogue of sources and components as a prior and ran on a random subset of 2443 sources (to save computation time as this was just being run as a test). The flux measured with XID+ was compared to the flux measured by PyBDSF (Figure 4.3). I compared to both the total and peak flux from PyBDSF. The peak flux is the peak flux of the Gaussian and the total flux is the integrated flux of the Gaussian. I can see that XID+ does a good job at recovering the peak flux but has an offset from the total flux. This is expected as XID+ is fitting a symmetric Gaussian to the source's position, so I expect a good agreement with the peak flux. The fact that XID+ is systematically lower than the total flux fits with the total flux being the integrated flux and therefore captures any additional flux that isn't perfectly fit by the Gaussian. There seems to be a slight trend for XID+ to underestimate the flux of the individual Gaussian components compared to source's flux. From these results I decided to include the source catalogue as part of our prior catalogue when running XID+ across the entire field. Partly because the results are less affected by systematic error but also so that I am measuring the flux of the source and not the flux of an individual Gaussian component as these components likely originate from a single galaxy and therefore all the flux should be assigned to that galaxy.

4.3.2 Injected sources

In the previous section I have confirmed that XID+ is able to measure the flux of sources that have been deconvolved with the dirty beam. However, if I want to measure the flux of fainter sources that may not have been deconvolved when the dirty image was CLEANed I need to check whether XID+ can measure the flux of sources that are convolved with the dirty beam. To investigate this I injected fake sources into the LOFAR image and

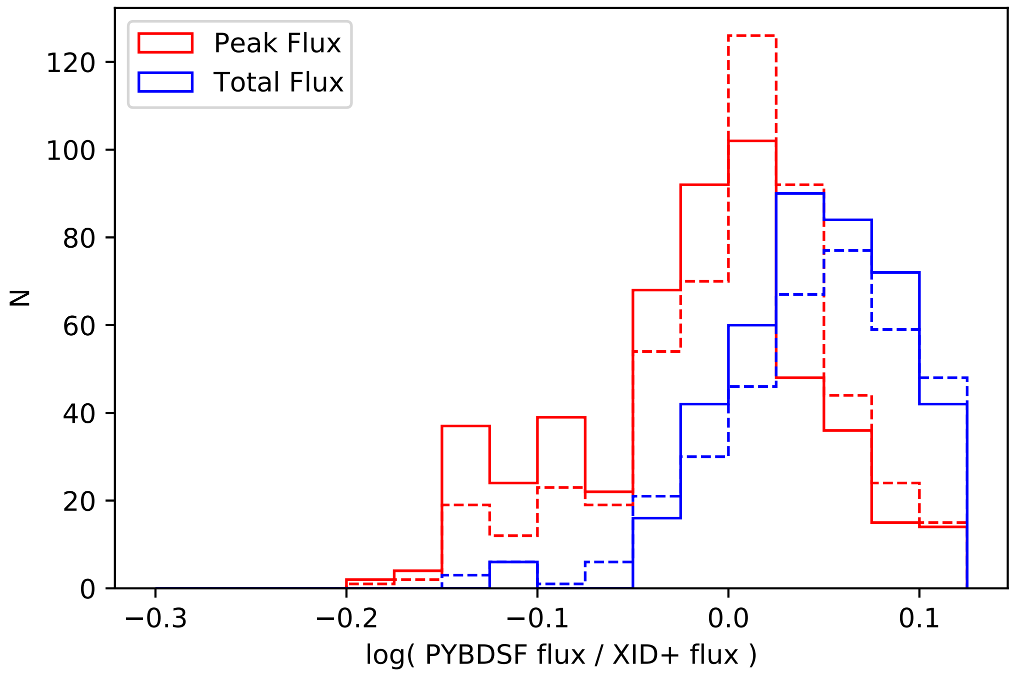

Figure 4.3: Ratio of the PyBDSF flux to the flux measured with XID+. The red lines show the comparison between the total flux while the blue line is for the peak flux. The solid and dashed lines are when comparing to the source and component PyBDSF catalogue.

convolved them with the dirty beam.

We injected 10000 sources whose fluxes are split between 100 equally spaced values in log space from 0.1mJy to 100mJy. I then looked at the shape of the flux posteriors to see at what flux they began diverge from a symmetric Gaussian. This was assessed by looking at the ratio of the 84th-50th divided by the 50th-16th percentile. I can see that sources have a symmetric posterior when their flux is > 0.1mJy. This corresponds to five times the average rms noise of the map so is reasonable that the flux posterior would start to be influenced by the error distribution at this level. This can be understood by considering the case of a prior list source that doesn't correspond to a galaxy (such as when the prior list contains unidentified artifacts). In this case XID+ will try to find a flux which best explains any background emission around the fake sources position. As the background has a Gaussian distribution with a mean of 0 and a rms of 20μm it will find a flux posterior that matches this distribution (only the right hand side of the distribution as the prior prevents a negative flux). This half gaussian flux posterior will have a high skew which allows us to identify the flux below which we are influenced by the background emission. It also indicates that I am limited by the background noise and am not dealing with many confused sources (as I expect for injected sources).

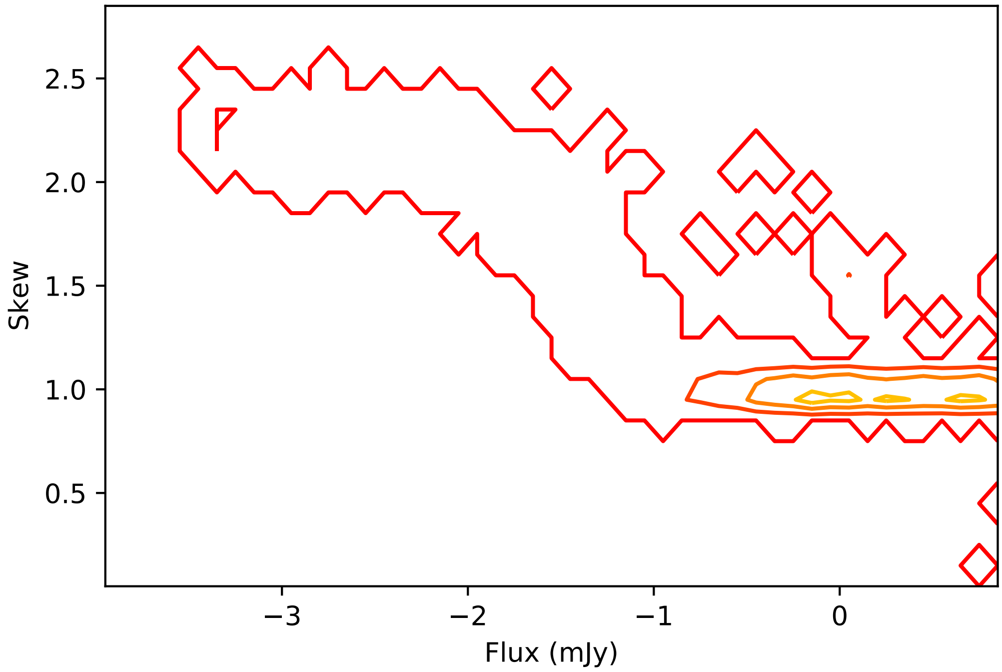

Figure 4.4: Skew of the flux posterior varying depending on the median flux. Above ~ 0.1mJy the posteriors begin to diverge from a symmetric form. Skew is defined as the ratio of the 84th-50th percentile and the 50th-16th percentile.

This gives us confidence that I can detect sources that have not been deconvolved provided they are sufficiently bright to be above the background.

4.3.3 New sources

We ran XID+ across the entire ELAIS-N1 field with the PyBDSF source catalogue as the prior. In addition, multiwavelength sources were added into the prior catalogue if their predicted radio flux is above 0.1mJy (predicted from the TIR luminosity and the FIRC). I calculated the predicted radio flux from the FIRC relation I measured in Chapter 3 from Table 3.3 given the source's TIR luminosity from the *magphys* SED fit. I removed sources from this category that were found to be crossmatches for the radio sources. The image was split in HEALPIX tiles and each tile was run in parallel. I found that tiles containing a bright source had an issue with the MCMC chains becoming stuck and not exploring the posterior. This was caused by the bright source having extended emission that is not well modelled by a point source. Most samples from the posterior will have an incredibly low likelihood because of this, in practice this likelihood was zero as it was so low the computer was unable to store it correctly. This means that if the starting points for the chains isn't near the peak of the likelihood then the gradient will be zero in all directions in parameter space. This will prevent the chains from moving as they cannot select a direction to move in. The only time the chain will move is when it is randomly kicked to a new location. These false posteriors will provide incredibly inaccurate fluxes. To solve this issue I place a circular mask around sources with a flux of > 50mJy with a radius of 30 arcseconds. This removes the majority of the bright extended emission that significantly affects the posterior while being unlikely to remove other LOFAR sources due to the low source density. However, this doesn't cover the very brightest sources that have very large extended emission as well as potential artifacts around them. In addition, some fainter sources can still have extended emission such as radio AGN that can extend for arcminutes while simultaneously being fainter than 50mJy.

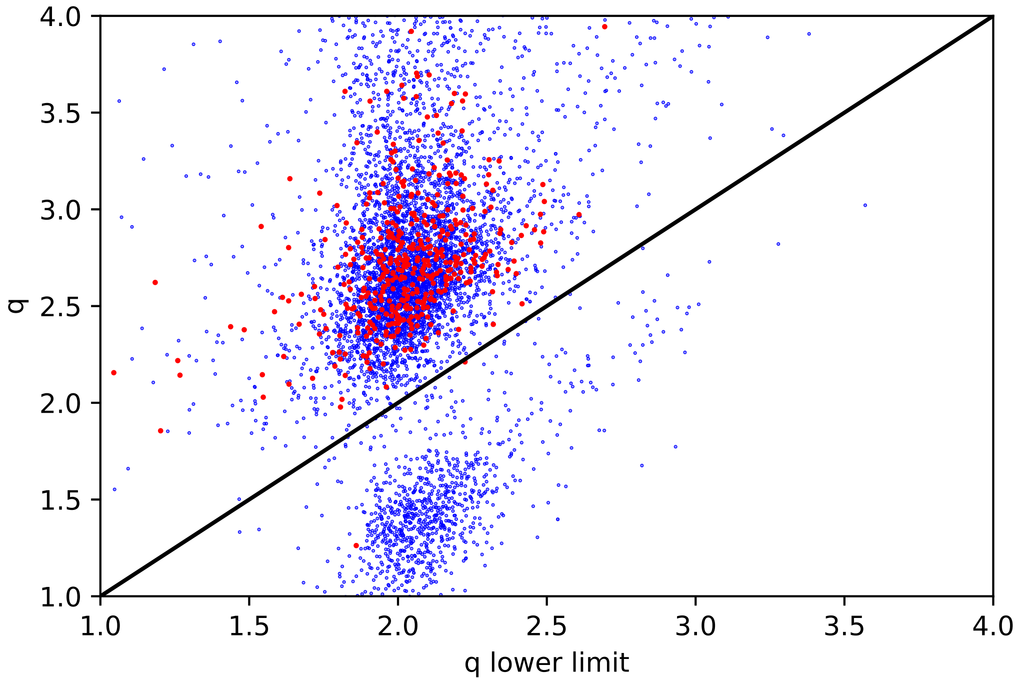

Figure 4.5: q measured using the 150MHz flux from XID+ against the lower limit of q measured with the upper limit on the 150MHz flux. The blue points show all sources that weren't part of the PyBDSF catalogue while the red points are the subset of blue points whose p value residual statistic is less than 0.5 (i.e we trust the fit that the measured flux provides to the map).

With bright sources masked we reran XID+ on the whole image with the same prior list. We evaluated the flux posterior of each source to determine whether we can trust the flux measured by XID+. This was done by creating 1000 maps by sampling from the flux posterior of the sources in the map as well as the noise posterior. For each source the surrounding pixels (pixels within one FWHM of the source position) were compared to the 1000 sample pixel counterparts and the proportion that were more than twice the pixel error from the true pixel flux was measured. This proportion is called the p value residual statistic and source where this was above 0.5 were flagged as having an unreliable flux. Using the new 150MHz flux I recalculated their q values and compared them to the upper limit on q I would measure from the error on the pixel the source is in. I find the majority of sources have a higher q than the lower limit of q I measured (figure 4.5), giving further confidence in the accuracy of these fluxes. The subset of sources whose measured q is lower than the limit expected from the error on the pixel they are located in are located near to bright sources whose extended emission or artifacts are being incorrectly assigned by XID+.

We can use these new 150MHz fluxes to remeasure the FIRC to see the effect of these new sources on the relation between q (see section 3.5 for the definition) and stellar mass. We use the methodology described in section 3.6.2 as well as accounting for the underestimation in the uncertainty caused by bootstrapping. This reduces the number of lower limits on q from 1793 to 1585 and adds 208 detected galaxies (on top of the 2353 previously detected galaxies). The new relation was found to be $q = 2.01 \pm 0.02 - 0.17 \pm 0.03M_*$ (figure 4.6) which is of minimal difference to the relation measured in section 3.6.2. This is to be expected as we only added a small number of detected galaxies to our sample (≈10% increase in sample size) which is unlikely to significantly affect the median of our sample. In addition, the use of survival analysis is designed to account for the non detections.

4.3.4 Low SNR radio sources

Our first run only included sources whose predicted 150MHz flux was five times greater than the average noise in the radio image. However, this is unlikely to detect a significant number of sources (sources whose flux is trusted based on both their posterior skew and Pval residual statistic). When we consider only the sources whose predicted SNR> 5 the sources density of our prior list will be very low and therefore we will not be able to detect faint sources whose fluxes are below the background and confusion noise. We created a prior list that includes all galaxies whose predicted radio flux is greater than two times the average background flux. We chose this limit to increase the source density to the point

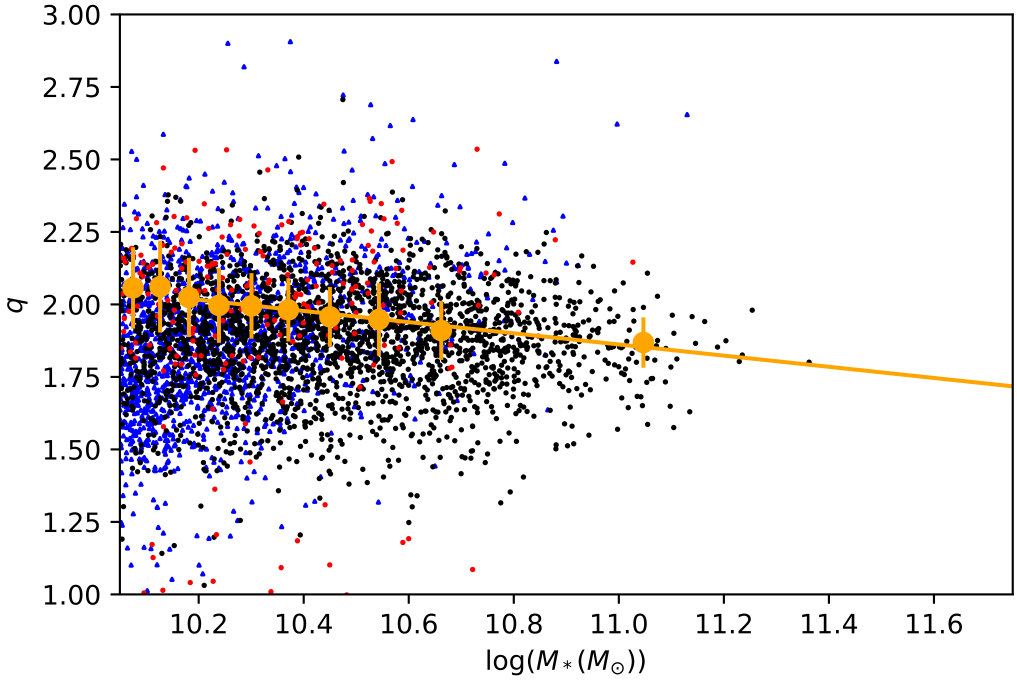

Figure 4.6: FIRC at 150MHz for LOFAR detected galaxies (black dots), galaxies whose 150MHz flux is measured using XID+ (red dots) and galaxies undetected at 150MHz (blue dots represent lower limits on q). The orange dots are the median q in each stellar mass bin measured using survival analysis and the orange line is the linear fit to these medians.

where confusion would become a relvant factor but not so high that the flux posteriors would become degenerate with their neighbours. This would occur when two sources are so close together that XID+ could assign the majority of the flux in the map to either source with equal likelihood. We masked bright sources in the same manner as described above.

From figure 4.7 we can see that the flux posteriors are symmetric below 0.1mJy, which corresponds to 5σ. This is an improvement compared to only considering the brighter sources. Figure 4.8 shows the evolution of the FIRC with stellar mass with the addition of these extra sources, 804 lower limits now have direct detections ($\approx 33\%$ of the previous sample size in section 3.6.2). With these new detections the relation is $q = 2.00 \pm 0.02 - 0.18 \pm 0.04 M_*$ again showing little to no difference with my previous results. This implies that survival analysis is measuring the underlying relation accurately and measuring the flux of previously undetected galaxies has little impact on the relation. However, it is worth investigating the reliability of these measured fluxes in more detail so they can be used for other purposes.

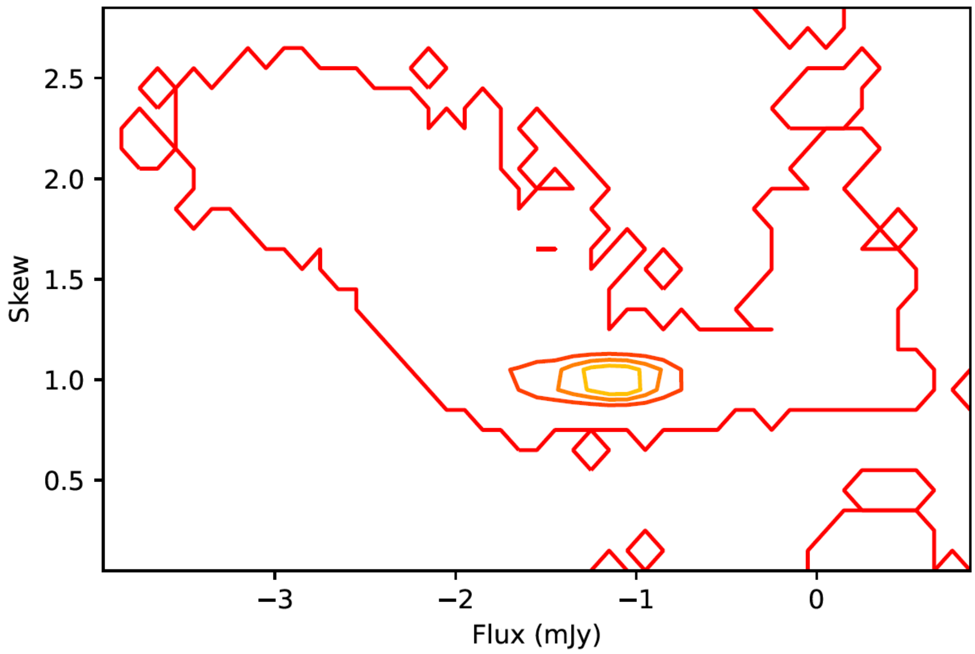

Figure 4.7: Skew of the flux posterior varying depending on the median flux for galaxies with a low predicted SNR. Above $\sim$ 0.02mJy the posteriors begin to diverge from a symmetric form. Skew is defined as the ratio of the 84th-50th percentile and the 50th-16th percentile.

XID+ measures the flux posterior of galaxies within the prior list. This posterior is then used to measure the flux and flux error for these galaxies to create a traditional catalogue. These fluxes are measured by taking the median of the flux posterior and the error is the 84th-16th percentile divided by two. However, this approach is only valid when the flux posterior is roughly symmetric and has a single peak. I plotted the flux posterior (figure 4.9) for a random 10% of sources after dividing each of them by their median. We excluded sources within tiles that are affected by unmasked extended emission. This was done by examining the p value residual statistic. If the majority of sources in a tile have a p value residual statistic > 0.5 we consider the tile to be contaminated by extended emission and the fluxes of sources within that tile cannot be trusted. This allows us to spot any patterns in the sources flux posterior and validate whether the assumptions of a single peak and symmetric flux posterior are true. From figure 4.9 we can see that there are three major shapes of flux posterior. Firstly there are sources with a single peaked distribution, with varying width, at a normalised flux of one. Fluxes and flux uncertainties measured from these distributions will be accurate, providing the p value residual statistic is less than 0.5. Secondly there is a smaller subset of sources with a heavily skewed distribution whose peak is close to zero. The median flux for these sources does not represent the peak

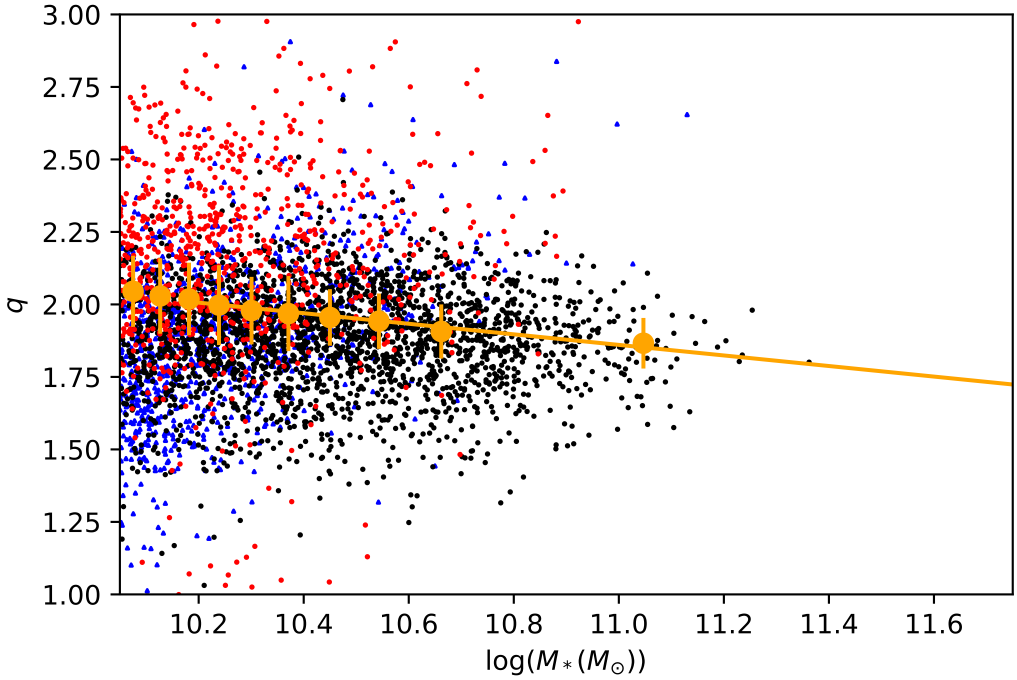

Figure 4.8: FIRC at 150MHz for LOFAR detected galaxies (black dots), galaxies whose 150MHz flux is measured using XID+ on a low predicted SNR prior list (red dots) and galaxies undetected at 150MHz (blue dots represent lower limits on q). The orange dots are the median q in each stellar mass bin measured using survival analysis and the orange line is the linear fit to these medians.

of the flux posterior and therefore cannot be relied on. However, when checking for the skew of the flux posterior these sources will be flagged as the distribution is not symmetric. Finally we have a large group of sources whose posterior has a double peak. In these cases the median has absolutely no relation to either peak while we have no idea which peak to use as they are equally likely. In addition, these distributions are symmetric and will not be picked up by examining their skew. The majority of these flux posteriors provide a good recreation of the map (as can be seen by their colour) meaning they are not caught by any of the checks we use to validate XID+ fluxes. One way around this would be to use the full posterior and sample fluxes from it that can be used for whatever purpose is required. This would account for the double peak or would allow limiting the posterior to just one of the peaks if there is a physically motivated reason for doing so.

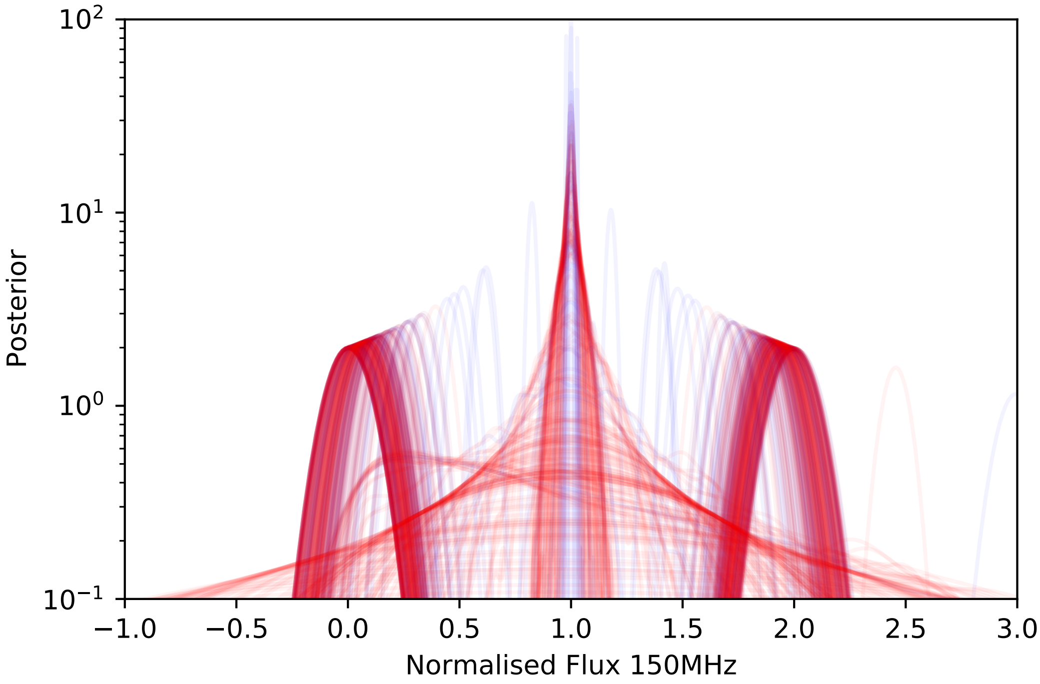

Figure 4.9: Normalised flux posterior for a random 10% of sources. The redder the line the lower its p value residual statistic (a value of 0 shows an excellent agreement between the flux posterior and the observed data) while bluer lines have a p value residual statistic closer to one, purple lines are somewhere in between. The more opaque regions show where more sources reside.

4.3.5 Comparison to other methods

XID+ is not the only software that can measure the flux of galaxies at known positions, each of which have their own advantages and disadvantages depending on how they are used. One example is the "Super-Deblended" method from Liu et al. (2018). This method measures the flux in successive bands independently, while using SED fitting to create the prior list in each band. Starting with a prior list of sources selected at 24μm and 20cm they used SED fitting to predict the emission in the FIR bands (100, 160, 250, 350 and 500μm). If the emission was deemed negligible then its predicted emission was subtracted from the image and the sources was excluded from their prior list. It should be noted that each band was fitted independently so if a sources emission at 100μm is deemed negligible it will still be considered at redder bands as high redshift sources could have negligible emission at shorter wavelengths. The fluxes are then measured for each of the prior list galaxies by fitting the PSF to the map using Monte Carlo simulations that enable reliable error estimates. The major advantages of this method over XID+ are in the method of creating a prior list in a physically motivated manner. In comparison the prior lists used for XID+ are created in a more ad hoc manner for example the prior lists I used above were created by selecting galaxies based on their predicted 150MHz fluxes. There was no physically motivated reason for the flux limit used here other then to limit the source density to prevent degeneracies in the measured flux posteriors. However, ”super-deblended” suffers from the same degeneracy problem as XID+ and as such their prior list was selected to give a source density of < 1 per beam. However, as discussed later, XID+ can be extended to incorporate hierarchical models that will provide additional constraints on the FIR and radio fluxes. The final issue with the ”super-deblended” method is in the SED fitting used to create the prior list. The inherent assumptions made when SED fitting can result in unmeasured biases and errors. Though their selection of SED components is doe to minimise these biases they are impossible to avoid and difficult to quantify.

Alternatively Malefahlo et al. (2020) used a Bayesian stacking approach to detect galaxies below the background noise. This was done by modelling the stacked flux as a combination of flux from sources plus the background noise. This method allows detections of groups of galaxies whose individual flux is well below the 5σ limit but doesn't provide individual flux measurements for each galaxy.

In conclusion, the current implementation of XID+ provides few advantages compared to other methods. However, the potential addition of hierarchical models to XID+ would allow it to provide additional constraints on the flux of individual galaxies. These constraints could allow XID+ to break the degeneracy that occurs when two sources lie within one beam width.

4.4 Future Work

Looking forward there are several directions that this work could take. Here I will outline three of these options and discuss the scientific implications and hurdles each will have

4.4.1 Deblending radio maps

As radio surveys push to greater and greater sensitivity they will detect an increasing number of confused galaxies. Using the LoTSS deep fields as an example, deblending is done by examining LOFAR sources that are made up of multiple Gaussian components which have different crossmatches from LR. The LOFAR source is examined by eye and the source is split into multiple sources if whoever is examining it thinks it is a blended radio source. This is done by an expert user, so their time is valuable and the number of expert users is limited so finding a way to automate the majority of this process would be ideal. Using XID+ to carry out this deblending uses a different procedure. Instead of crossmatching the radio sources, that have already been detected and had their fluxes measured, to known optical galaxies it would instead measure their radio flux. Currently XID+ has been run with the radio positions as priors rather than the position of the optical crossmatches. The first check that would be needed is to run XID+ on these blended sources with the optical positions as the prior catalogue.

The potential problem with this approach is that the density of optical sources may be too high. This would lead to a degeneracy between the radio flux of the optical galaxies, making it difficult to determine which galaxy is contributing. Overcoming this would require selecting which galaxies to include/exclude form the prior list. To do this I would need some way to determine which galaxies are most likely to be hosts of radio galaxies. Luckily the likelihood ratio (LR) provides a way of determining the relative likelihood of a galaxy being a radio host. This information could be included in the XID+ model to penalise galaxies with a low LR if they are assigned more flux than galaxies with a higher LR.

The alternative method for constructing the prior list would be to include galaxies based on their physical properties. Galaxies could be included if they are likely AGN hosts or are actively star forming. However, selecting galaxies that fall into these categories is not simple and any selection method will come with some inherent bias.

4.4.2 Hierarchically measure the FIRC

Even using XID+ to measure the 150MHz flux posterior to reduce the number of lower limits of q is not ideal for measuring the FIRC. What would be ideal is to include the FIRC in our model of the FIR and radio maps and measure the flux in the maps simultaneously. This would be done by modifying the model of XID+ to draw samples from a galaxy's total infrared (TIR) luminosity and radio flux. Then for a given TIR luminosity the FIR fluxes can be estimated using a SED fitting code (or a neural network to emulate the SED fitter). These fluxes can then be used to construct a model map for the sample and be compared to the observed map. I can include a hierarchical model for the FIRC, either a power law or linear fit is fine, that can provide an additional constraint on the FIR luminosity and radio flux for each galaxy (see Figure 4.10 for a visual representation of the model).

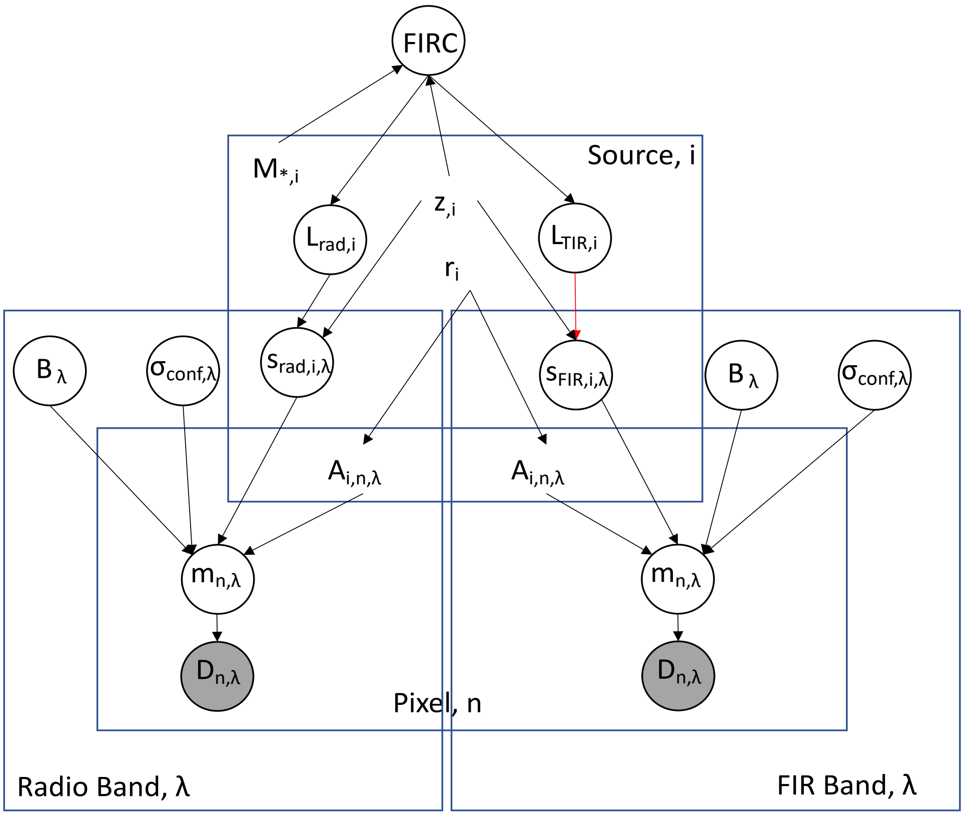

Figure 4.10: Extension of the basic XID+ model to include hierarchically measuring the FIRC by incorporating radio data. Squares represent repeated values, open circles correspond to random variables and variables without open circles are pre determined. The red line shows where the SED emulator is used.

There are some computational issues that will need to be overcome to modify XID+ to run with this model. The first is the computational time requires to run XID+ on all the FIR and radio maps simultaneously. You can see easily that the computational time will increase, especially since each iteration now requires running a SED (or SED emulator). Not a lot can be done about this other than running on smaller areas of the sky and therefore reducing the number of sources and pixels to fit. However, this brings us onto the other problem, namely the challenges of fitting the hierarchical model. If I am only able to run this version of XID+ on a small area of the sky I am likely to have a small number of sources in each region. This will make constraining the FIRC difficult if I only have a limited amount of data. I can potentially overcome this by combining the posterior from each of the separate areas with XID+ run on it.

4.4.3 Improving the current model

There is still work that can be done to improve the current model. As mentioned in 4.3.3 I have excluded the region around bright sources to enable the MCMC chains to converge. However, I only removed a circular region around each source which is unlikely to effectively remove the extended emission from these sources that isn't circularly symmetric (such as radio jets). Finding a better way to remove the extended emission will allow XID+ to run, without issue, on a larger area. One potential way of doing this would be to use the model image created during the radio image creation and then subtracting these bright sources from the image.

The other improvement would be to modify the background and confusion noise terms in XID+. In particular the assumption that the confusion noise is constant across the map will definitely be invalid. Furthermore the error matrix is assumed to be diagonal with no correlations accounted for. This assumption is valid for FIR maps but is not true for radio maps where the error around bright sources will be much greater do to emission that has been incorrectly modelled. Work could be done into better estimating the error matrix, potentially modelling the full error matrix as a sparse matrix.

4.5 Final thoughts

Overall XID+ shows a lot of promise when run on the LOFAR deep field. I found that XID+ is able to measure the same flux as PyBDSF (figure 4.3) giving evidence that the majority of fainter sources are point sources that are well fit by the clean beam. I was able to test the ability to recover sources that are convolved with the dirty beam by injecting fake sources convolved with the dirty beam. In addition I was able to test how well XID+ can measure the flux for faint sources whose flux is less than fives times the rms noise of the map. Next I ran XID+ across the entire ELAIS-N1 map while including galaxies whose predicted 150MHz flux, predicted from the FIRC, was more than five times the rms noise. I found that the new q values measured using the new 150MHz flux were consistently above the previous lower limits in q we measured based on the upper limit on the 150MHZ flux, giving confidence that the measured fluxes were reasonable. When XID+ was run on a lager prior list containing sources whose predicted flux at 150MHz was greater than twice the rms noise it was able to identify sources whose flux had a SNR<5. When these new fluxes were used to measure the FIRC no significant difference was found compared to using upper limits on these sources flux.

Moving forward I believe that the best step forward is to setup XID+ to measure the FIRC hierarchically. This would provide better constraints on the FIR fluxes of galaxies when they are correlated with the higher resolution radio map. These accurate FIR fluxes could be used to measure the TIR luminosity and provide constraints on the density of Luminous InfraRed Galaxies (LIRGs) and Hyper Luminous InfraRed Galaxies (HLIRGs). Meanwhile deblending the radio maps is less crucial currently as the majority of radio images aren't close to confusion limited based on the source density. In addition many radio telescopes have access to long baselines that can provide high resolution images that would reduce the need for deblending. The most urgent work that must be done is to change the way fluxes are measured from the posterior. Either the posterior should be directly sampled multiple times to propagate the uncertainties measured with XID+. Alternatively instead of taking the flux to be the median of the posterior a peak finding algorithm could be used to identify if multiple peaks are present and both fluxes could be recorded in any created catalogues.

Chapter 5

Conclusion

In this thesis we have examined how combining radio and FIR observations can enable a deeper understanding of galaxy evolution than considering the two separately. Here I will outline the main findings in this thesis as well as improvements that could be made to those results in the future.

Chapter 2 presents work done to crossmatch the LoTSS deep field catalogue in Lockman Hole to a multiwavelength optical and NIR catalogue. The purpose of which is to enable study of the physical properties traced by radio emission, such as AGN activity and SF, and link them to physical properties tied to the optical and NIR, such as stellar mass and redshift. This crossmatching was done with a combination of automated likelihood ratio (LR) analysis and visual inspection for sources unsuitable for the LR. In total 30402 (97.6% of the full radio source catalogue) radio galaxies were crossmatched. the LR incorporated the colour and magnitude in the r-band and at 4.5μm. Counterparts were predominately found to be redder galaxies that are likely to be massive early type galaxies that are hosting AGN. Additionally bright blue galaxies were a common counterpart, likely corresponding to the fainter star forming galaxies which the LoTSS deep fields are sensitive enough to detect. These results show the importance of including colour in the LR calculation. In addition, the colour of the crossmatches matches the expected results predicted by radio simulations such as SIMBA (Davé et al., 2019) and T-RECS (Bonaldi et al., 2019).

Of the 30402 galaxies with an identified crossmatch only 79.7% were found with the LR. Unfortunately this still leaves 5551 galaxies that needed to have their counterparts identified by eye. As radio surveys cover larger and larger areas with increasing sensitivity having to identify a similar fraction of galaxies by eye will become infeasible. To make matters worse, as the sensitivity increases the source density will also increase leading to more blended radio galaxies and more clustered sources that will be unsuitable for crossmatching with the LR. Work is being done to investigate the feasibility of using machine learning algorithms to automate the crossmatching process and reduce the need for visual inspection. An alternative approach would be use deblending software, such as XID+, to identify which sources are producing the observed radio emission in the case of blended sources. This approach is discussed more in chapter 4

Chapter 3 presents my work done to study the far infrared radio correlation (FIRC) at 150MHz. The FIRC is believed to originate from star formation. Massive stars, that primarily emit in the UV and trace recent star formation due to their short lifespans, are responsible for heating dust in the ISM and producing supernovae that accelerate electrons which emit synchrotron radiation at radio frequencies. This leads to the observed correlation between a galaxies IR and radio luminosity. Thoroughly understanding the processes that affect this relation is an important step towards developing a comprehensive radio luminosity-star formation rate relation that could take full advantage of upcoming radio surveys such as LoTSS and the SKA.

We used the LoTSS deep field data in ELAIS-N1 to construct two mass complete samples to investigate the dependence of the FIRC on redshift and stellar mass. We found that the FIRC has a stronger dependence on stellar mass, with a relatively minor dependence on redshift. The FIRC was found to follow the relation $q_{TIR}(z, M_*) = (1.98 \pm 0.02)(1+z)^{0.02\pm0.04} + (-0.22 \pm 0.03)\log(M_*) - 10.45$. We investigated the possibility of AGN activity being the cause of either dependence and found no evidence to support this.

My thoughts on the best avenue for continuing our study of the FIRC would be to investigate the spectral index of the radio emission for these galaxies. As seen in Calistro Rivera et al. (2017) there is a large dispersion radio spectral index and the choice of spectral index will have a big effect on rest frame luminosity. If we had measurement for each galaxies spectral index it could explain some of the dispersion seen in the FIRC.

In Chapter 4 I show the results of running XID+ on the LoTSS deep field ELAIS-N1. I found that XID+ was able to measure the same peak flux as PyBDSF when the PyBDSF source position was used as the prior. Next, by injecting fake sources into the map we were able to measure an unbiased flux posterior when the flux of the injected source was above 0.1mJy. Fluxes lower than this were found to have a non Gaussian posterior, likely indicating that they were being significantly affected by our flux prior convolved with the error distribution of the map. Finally XID+ was run across the entire ELAIS-N1 image with the PyBDSF source catalogue as a prior plus source from the multiwavelength catalogue whose predicted radio flux was greater then 0.1mJy (radio flux was predicted from the galaxies TIR luminosity and the FIRC). These new 150MHz fluxes were used to compute q for these galaxies and nearly all values were greater than the lower limits previously measured by calculating an upper limit on their 150MHz flux.

Bibliography

Aird, J., Nandra, K., Laird, E. S., Georgakakis, A., Ashby, M. L., Barmby, P., Coil, A. L., Huang, J. S., Koekemoer, A. M., Steidel, C. C., and Willmer, C. N. (2010). The evolution of the hard X-ray luminosity function of AGN. *Mon. Not. R. Astron. Soc.*, 401(4):2531–2551. 16

Antonucci, R. (1993). Unified models for active galactic nuclei and quasars. *Annu. Rev. Astron. Astrophys.*, 31(1):473–521. 14

Baugh, C. M. (2006). A primer on hierarchical galaxy formation: The semi-analytical approach. 19

Bell, E. F. (2003). Estimating Star Formation Rates from Infrared and Radio Luminosities: The Origin of the Radio-Infrared Correlation. *Astrophys. J.*, 586(2):794–813. 48, 50

Berta, S., Lutz, D., Santini, P., Wuyts, S., Rosario, D., Brisbin, D., Cooray, A., Franceschini, A., Gruppioni, C., Hatziminaoglou, E., Hwang, H. S., Le Floc'h, E., Magnelli, B., Nordon, R., Oliver, S., Page, M. J., Popesso, P., Pozzetti, L., Pozzi, F., Riguccini, L., Rodighiero, G., Roseboom, I., Scott, D., Symeonidis, M., Valtchanov, I., Viero, M., and Wang, L. (2013). Panchromatic spectral energy distributions of Herschel sources. *Astron. Astrophys.*, 551:100. 84

Bertin, E. (1996). SExtractor: Software for source extraction. *Astron. Astrophys. Suppl. Ser.*, 117(2):393–404. 24, 34, 52

Bertin, E., Mellier, Y., Radovich, M., Missonnier, G., Didelon, P., and Morin, B. (2002). The TERAPIX Pipeline. *Astron. Data Anal. Softw. Syst. XI*, 281:228. 33

Best, P., Kondapally, R., Duncan, K., and Smith, D. (2021). No Title. *Astron. Astrophys. Submitt.* 55, 61, 62

Best, P. N., Arts, J. N., Röttgering, H. J., Rengelink, R., Brookes, M. H., and Wall,

J. (2003). CENSORS: A Combined EIS-NVSS Survey of Radio Sources - I. Sample definition, radio data and optical identifications. 31

Béthermin, M., Wu, H. Y., Lagache, G., Davidzon, I., Ponthieu, N., Cousin, M., Wang, L., Doré, O., Daddi, E., and Lapi, A. (2017). The impact of clustering and angular resolution on far-infrared and millimeter continuum observations. *Astron. Astrophys.*, 607:89. 51, 62, 82

Birzan, L., Rafferty, D. A., McNamara, B. R., Wise, M. W., and Nulsen, P. E. J. (2004). A Systematic Study of Radio-induced X-Ray Cavities in Clusters, Groups, and Galaxies. *Astrophys. J.*, 607(2):800–809. 17

Bonaldi, A., Bonato, M., Galluzzi, V., Harrison, I., Massardi, M., Kay, S., De Zotti, G., and Brown, M. L. (2019). The Tiered Radio Extragalactic Continuum Simulation (T-RECS). *Mon. Not. R. Astron. Soc.*, 482(1):2–19. 45, 106

Bondi, H. (1952). On Spherically Symmetrical Accretion. *Mon. Not. R. Astron. Soc.*, 112(2):195–204. 20

Boquien, M., Burgarella, D., Roehlly, Y., Buat, V., Ciesla, L., Corre, D., Inoue, A. K., and Salas, H. (2018). CIGALE: a python Code Investigating GALaxy Emission. *Astron. Astrophys.*, 622:103. 9

Bouwens, R. J., Illingworth, G. D., Oesch, P. A., Franx, M., Labbé, I., Trenti, M., Van Dokkum, P., Carollo, C. M., González, V., Smit, R., and Magee, D. (2012). UV-continuum slopes at z 4-7 from the HUDF09+ERS+CANDELS observations: Discovery of a well-defined UV color-magnitude relationship for z 4 star-forming galaxies. 16

Brammer, G. B., van Dokkum, P. G., and Coppi, P. (2008). EAZY: A Fast, Public Photometric Redshift Code. *Astrophys. J.*, 686(2):1503–1513. 9

Brown, M. J. I., Dey, A., Jannuzi, B. T., Brand, K., Benson, A. J., Brodwin, M., Croton, D. J., and Eisenhardt, P. R. (2007). The Evolving Luminosity Function of Red Galaxies. *Astrophys. J.*, 654(2):858–877. 52

Brown, M. J. I., Zheng, Z., White, M., Dey, A., Jannuzi, B. T., Benson, A. J., Brand, K., Brodwin, M., and Croton, D. J. (2008). Red Galaxy Growth and the Halo Occupation Distribution. *Astrophys. J.*, 682(2):937–963. 52

Calistro Rivera, G., Lusso, E., Hennawi, J. F., and Hogg, D. W. (2016). AGNfitter: A BAYESIAN MCMC APPROACH TO FITTING SPECTRAL ENERGY DISTRIBUTIONS OF AGNs. *Astrophys. J.*, 833(1):98. 55

Calistro Rivera, G., Williams, W. L., Hardcastle, M. J., Duncan, K., Röttgering, H. J., Best, P. N., Brüggen, M., Chyzy, K. T., Conselice, C. J., de Gasperin, F., Engels, D., Gürkan, G., Intema, H. T., Jarvis, M. J., Mahony, E. K., Miley, G. K., Morabito, L. K., Prandoni, I., Sabater, J., Smith, D. J., Tasse, C., van der Werf, P. P., and White, G. J. (2017). The LOFAR window on star-forming galaxies and AGNs - curved radio SEDs and IR-radio correlation at $0 < z < 2.5$. *Mon. Not. R. Astron. Soc.*, 469(3):3468–3488. xii, xiii, 47, 49, 50, 61, 64, 65, 70, 73, 75, 76, 78, 82, 107

Calzetti, D., Kinney, A. L., and Storchi-Bergmann, T. (1994). Dust extinction of the stellar continua in starburst galaxies: The ultraviolet and optical extinction law. *Astrophys. J.*, 429:582. 7

Carlstrom, J. E. and Kronberg, P. P. (1991). H II regions in M82 - High-resolution millimeter continuum observations. *Astrophys. J.*, 366:422. 12

Carnall, A. C., Leja, J., Johnson, B. D., McLure, R. J., Dunlop, J. S., and Conroy, C. (2019). How to Measure Galaxy Star Formation Histories. I. Parametric Models. *Astrophys. J.*, 873(1):44. 55

Casali, M., Adamson, A., Alves De Oliveira, C., Almaini, O., Burch, K., Chuter, T., Elliot, J., Folger, M., Foucaud, S., Hambly, N., Hastie, M., Henry, D., Hirst, P., Irwin, M., Ives, D., Lawrence, A., Laidlaw, K., Lee, D., Lewis, J., Lunney, D., McLay, S., Montgomery, D., Pickup, A., Read, M., Rees, N., Robson, I., Sekiguchi, K., Vick, A., Warren, S., and Woodward, B. (2007). The UKIRT wide-field camera. *Astron. Astrophys.*, 467(2):777–784. 33

Casey, C. M. (2012). Far-infrared spectral energy distribution fitting for galaxies near and far. *Mon. Not. R. Astron. Soc.*, 425(4):3094–3103. 9

Casey, C. M., Narayanan, D., and Cooray, A. (2014). Dusty star-forming galaxies at high redshift. 47

Chabrier, G. (2003). Galactic Stellar and Substellar Initial Mass Function. *Publ. Astron. Soc. Pacific*, 115(809):763–795. 4, 21

Ciesla, L., Charmandaris, V., Georgakakis, A., Bernhard, E., Mitchell, P. D., Buat, V., Elbaz, D., Floc'h, E. L., Lacey, C. G., Magdis, G. E., and Xilouris, M. (2015). Constraining the properties of AGN host galaxies with Spectral Energy Distribution modeling. *Astron. Astrophys.*, 576:10. 10

Ciliegi, P., Zamorani, G., Hasinger, G., Lehmann, I., Szokoly, G., and Wilson, G. (2003). A deep VLA survey at 6 cm in the Lockman Hole. *Astron. Astrophys.*, 398(3):901–918. 29

Condon, J. (1992). Radio Emission from Normal Galaxies. *Annu. Rev. Astron. Astrophys.*, 30(1):575–611. 47

Condon, J. J. (1997). Errors in Elliptical Gaussian FITS. *Publ. Astron. Soc. Pacific*, 109:166. 38

Croton, D. J., Springel, V., White, S. D., De Lucia, G., Frenk, C. S., Gao, L., Jenkins, A., Kauffmann, G., Navarro, J. F., and Yoshida, N. (2006). The many lives of active galactic nuclei: Cooling flows, black holes and the luminosities and colours of galaxies. *Mon. Not. R. Astron. Soc.*, 365(1):11–28. 18

Da Cunha, E., Charlot, S., and Elbaz, D. (2008). A simple model to interpret the ultraviolet, optical and infrared emission from galaxies. *Mon. Not. R. Astron. Soc.*, 388(4):1595–1617. 9, 55, 81

Davé, R., Anglés-Alcázar, D., Narayanan, D., Li, Q., Rafieferantsoa, M. H., and Appleby, S. (2019). SIMBA: Cosmological simulations with black hole growth and feedback. *Mon. Not. R. Astron. Soc.*, 486(2):2827–2849. 19, 106

Davé, R., Thompson, R., and Hopkins, P. F. (2016). MUFASA: Galaxy formation simulations with meshless hydrodynamics. *Mon. Not. R. Astron. Soc.*, 462(3):3265–3284. 19

Davidson-Pilon, C., Kalderstam, J., Jacobson, N., Reed, S., Kuhn, B., Zivich, P., Williamson, M., AbdealiJK, Datta, D., Fiore-Gartland, A., Parij, A., WIlson, D., Gabriel, Moneda, L., Moncada-Torres, A., Stark, K., Gadgil, H., Jona, Singaravelan, K., Besson, L., Peña, M. S., Anton, S., Klintberg, A., GrowthJeff, Noorbakhsh, J., Begun, M., Kumar, R., Hussey, S., Seabold, S., and Golland, D. (2021). CamDavidsonPilon/lifelines: 0.25.10. 62

Davies, L. J. M., Huynh, M. T., Hopkins, A. M., Seymour, N., Driver, S. P., Robotham, A. G. R., Baldry, I. K., Bland-Hawthorn, J., Bourne, N., Bremer, M. N., Brown, M. J. I., Brough, S., Cluver, M., Grootes, M. W., Jarvis, M., Loveday, J., Moffet, A., Owers, M., Phillipps, S., Sadler, E., Wang, L., Wilkins, S., and Wright, A. (2017). Galaxy And Mass Assembly: The 1.4GHz SFR indicator, SFR-M* relation and predictions for ASKAP-GAMA. *MNRAS*, 466:2312–2324. 47

Del Moro, A., Alexander, D. M., Mullaney, J. R., Daddi, E., Pannella, M., Bauer, F. E., Pope, A., Dickinson, M., Elbaz, D., Barthel, P. D., Garrett, M. A., Brandt, W. N., Charmandaris, V., Chary, R. R., Dasyra, K., Gilli, R., Hickox, R. C., Hwang, H. S., Ivison, R. J., Juneau, S., Le Floc'h, E., Luo, B., Morrison, G. E., Rovilos, E., Sargent, M. T., and Xue, Y. Q. (2013). GOODS- Herschel : radio-excess signature of hidden AGN activity in distant star-forming galaxies. *Astron. Astrophys.*, 549:A59. 47

Delhaize, J., Smolčić, V., Delvecchio, I., Novak, M., Sargent, M., Baran, N., Magnelli, B., Zamorani, G., Schinnerer, E., Murphy, E. J., Aravena, M., Berta, S., Bondi, M., Capak, P., Carilli, C., Ciliegi, P., Civano, F., Ilbert, O., Karim, A., Laigle, C., Le Fèvre, O., Marchesi, S., McCracken, H. J., Salvato, M., Seymour, N., and Tasca, L. (2017). The VLA-COSMOS 3 GHz Large Project: The infrared-radio correlation of star-forming galaxies and AGN to z 6. *Astron. Astrophys.*, 602. xii, 47, 49, 50, 64, 65, 70, 72, 73, 74

Delvecchio, I., Daddi, E., Sargent, M. T., Jarvis, M. J., Elbaz, D., Jin, S., Liu, D., Whittam, I. H., Algera, H., Carraro, R., D'Eugenio, C., Delhaize, J., Kalita, B. S., Leslie, S., Molnár, D. C., Novak, M., Prandoni, I., Smolčić, V., Ao, Y., Aravena, M., Bournaud, F., Collier, J. D., Randriamampandry, S. M., Randriamanakoto, Z., Rodighiero, G., Schober, J., White, S. V., and Zamorani, G. (2021). The infrared-radio correlation of star-forming galaxies is strongly M-dependent but nearly redshift-invariant since z 4. *Astron. Astrophys.*, 647:25. xii, xiii, xiv, 49, 50, 71, 74, 75, 76, 77, 78, 79, 81, 82

Dewdney, P. E., Hall, P. J., Schilizzi, R. T., and Lazio, T. J. L. (2009). The square kilometre array. *Proc. IEEE*, 97(8):1482–1496. 13

Donley, J. L., Koekemoer, A. M., Brusa, M., Capak, P., Cardamone, C. N., Civano, F., Ilbert, O., Impey, C. D., Kartaltepe, J. S., Miyaji, T., Salvato, M., Sanders, D. B., Trump, J. R., and Zamorani, G. (2012). Identifying luminous active galactic nuclei in deep surveys: Revised IRAC selection criteria. 61

Duncan, K. J., Kondapally, R., Brown, M. J. I., Bonato, M., Best, P. N., Röttgering, H.

J. A., Bondi, M., Bowler, R. A. A., Cochrane, R. K., Gürkan, G., Hardcastle, M. J., Jarvis, M. J., Kunert-Bajraszewska, M., Leslie, S. K., Małek, K., Morabito, L. K., O'sullivan, S. P., Prandoni, I., Sabater, J., and Shimwell, T. W. (2021). The LOFAR Two-meter Sky Survey: Deep Fields Data Release 1 IV. Photometric redshifts and stellar masses. *Astron. Astrophys.*, 648:21. 51, 54, 59, 61, 81

Eldridge, J. J., Stanway, E. R., Xiao, L., Mcclelland, L. A. S., Taylor, G., Ng, M., Greis, S. M. L., and Bray, J. C. (2017). Binary Population and Spectral Synthesis Version 2.1: Construction, Observational Verification, and New Results. *Publ. Astron. Soc. Aust.*, 34:61. 6

Fabian, A. (2012). Observational Evidence of Active Galactic Nuclei Feedback. *Annu. Rev. Astron. Astrophys.*, 50(1):455–489. 16

Fazio, G. G., Hora, J. L., Allen, L. E., Ashby, M. L. N., Barmby, P., Deutsch, L. K., Huang, J.-S., Kleiner, S., Marengo, M., Megeath, S. T., Melnick, G. J., Pahre, M. A., Patten, B. M., Polizotti, J., Smith, H. A., Taylor, R. S., Wang, Z., Willner, S. P., Hoffmann, W. F., Pipher, J. L., Forrest, W. J., McMurty, C. W., McCreight, C. R., McKelvey, M. E., McMurray, R. E., Koch, D. G., Moseley, S. H., Arendt, R. G., Mentzell, J. E., Marx, C. T., Losch, P., Mayman, P., Eichhorn, W., Krebs, D., Jhabvala, M., Gezari, D. Y., Fixsen, D. J., Flores, J., Shakoorzadeh, K., Jungo, R., Hakun, C., Workman, L., Karpati, G., Kichak, R., Whitley, R., Mann, S., Tollestrup, E. V., Eisenhardt, P., Stern, D., Gorjian, V., Bhattacharya, B., Carey, S., Nelson, B. O., Glaccum, W. J., Lacy, M., Lowrance, P. J., Laine, S., Reach, W. T., Stauffer, J. A., Surace, J. A., Wilson, G., Wright, E. L., Hoffman, A., Domingo, G., and Cohen, M. (2004). The Infrared Array Camera (IRAC) for the Spitzer Space Telescope. *Astrophys. J. Suppl. Ser.*, 154(1):10–17. 33

Ferrarese, L. and Merritt, D. (2000). A FUNDAMENTAL RELATION BETWEEN SUPERMASSIVE BLACK HOLES AND THEIR HOST GALAXIES. Technical report. 16

Flesch, E. W. (2019). The Million Quasars (Milliquas) Catalogue, v6.4. 61

Fleuren, S., Sutherland, W., Dunne, L., Smith, D. J. B., Maddox, S. J., González-Nuevo, J., Findlay, J., Auld, R., Baes, M., Bond, N. A., Bonfield, D. G., and Bourne, N. (2012). Herschel-ATLAS: VISTA VIKING near-infrared counterparts in the Phase 1 GAMA 9-h data. *Mon. Not. R. Astron. Soc*, 423:2407–2424. 28, 29, 39

Fritz, J., Franceschini, A., and Hatziminaoglou, E. (2006). Revisiting the infrared spectra of active galactic nuclei with a new torus emission model. *Mon. Not. R. Astron. Soc.*, 366(3):767–786. 55

Geach, J. E., Dunlop, J. S., Halpern, M., Smail, I., van der Werf, P., Alexander, D. M., Almaini, O., Aretxaga, I., Arumugam, V., Asboth, V., Banerji, M., Beanlands, J., Best, P. N., Blain, A. W., Birkinshaw, M., Chapin, E. L., Chapman, S. C., Chen, C. C., Chrysostomou, A., Clarke, C., Clements, D. L., Conselice, C., Coppin, K. E., Cowley, W. I., Danielson, A. L., Eales, S., Edge, A. C., Farrah, D., Gibb, A., Harrison, C. M., Hine, N. K., Hughes, D., Ivison, R. J., Jarvis, M., Jenness, T., Jones, S. F., Karim, A., Koprowski, M., Knudsen, K. K., Lacey, C. G., Mackenzie, T., Marsden, G., McAlpine, K., McMahon, R., Meijerink, R., Michalowski, M. J., Oliver, S. J., Page, M. J., Peacock, J. A., Rigopoulou, D., Robson, E. I., Roseboom, I., Rotermund, K., Scott, D., Serjeant, S., Simpson, C., Simpson, J. M., Smith, D. J., Spaans, M., Stanley, F., Stevens, J. A., Swinbank, A. M., Targett, T., Thomson, A. P., Valiante, E., Wake, D. A., Webb, T. M., Willott, C., Zavala, J. A., and Zemcov, M. (2017). The SCUBA-2 Cosmology Legacy Survey: 850 μm maps, catalogues and number counts. *Mon. Not. R. Astron. Soc.*, 465(2):1789–1806. 54

Griffin, M. J., Abergel, A., Abreu, A., Ade, P. A., André, P., Augueres, J. L., Babbedge, T., Bae, Y., Baillie, T., Baluteau, J. P., Barlow, M. J., Bendo, G., Benielli, D., Bock, J. J., Bonhomme, P., Brisbin, D., Brockley-Blatt, C., Caldwell, M., Cara, C., Castro-Rodriguez, N., Cerulli, R., Chanial, P., Chen, S., Clark, E., Clements, D. L., Clerc, L., Coker, J., Communal, D., Conversi, L., Cox, P., Crumb, D., Cunningham, C., Daly, F., Davis, G. R., DeAntoni, P., Delderfield, J., Devin, N., Di Giorgio, A., Didschuns, I., Dohlen, K., Donati, M., Dowell, A., Dowell, C. D., Duband, L., Dumaye, L., Emery, R. J., Ferlet, M., Ferrand, D., Fontignie, J., Fox, M., Franceschini, A., Frerking, M., Fulton, T., Garcia, J., Gastaud, R., K.Gear, W., Glenn, J., Goizel, A., Griffin, D. K., Grundy, T., Guest, S., Guillemet, L., Hargrave, P. C., Harwit, M., Hastings, P., Hatziminaoglou, E., Herman, M., Hinde, B., Hristov, V., Huang, M., Imhof, P., Isaak, K. J., Israelsson, U., Ivison, R. J., Jennings, D., Kiernan, B., King, K. J., Lange, A. E., Latter, W., Laurent, G., Laurent, P., Leeks, S. J., Lellouch, E., Levenson, L., Li, B., Li, J., Lilienthal, J., Lim, T., Liu, S. J., Lu, N., Madden, S., Mainetti, G., Marliani, P., McKay, D., Mercier, K., Molinari, S., Morris, H., Moseley, H., Mulder, J., Mur, M., Naylor, D. A., Nguyen, H., O'Halloran, B., Oliver, S., Olofsson, G., Olofsson, H. G., Orfei, R., J.Page, M., Pain, I., Panuzzo, P., Papageorgiou, A., Parks, G., Parr-Burman, P., Pearce, A., Pearson, C., Pérez-Fournon, I., Pinsard, F., Pisano, G., Podosek, J., Pohlen, M., Polehampton, E. T., Pouliquen, D., Rigopoulou, D., Rizzo, D., G.Roseboom, I., Roussel, H., Rowan-Robinson, M., Rownd, B., Saraceno, P., Sauvage, M., Savage, R., Savini, G., Sawyer, E., Scharmberg, C., Schmitt, D., Schneider, N., Schulz, B., Schwartz, A., Shafer, R., Shupe, D. L., Sibthorpe, B., Sidher, S., Smith, A., Smith, A. J., Smith, D., Spencer, L., Stobie, B., Sudiwala, R., Sukhatme, K., Surace, C., Stevens, J. A., Swinyard, B. M., Trichas, M., Tourette, T., Triou, H., Tseng, S., Tucker, C., Turner, A., Vaccari, M., Valtchanov, I., Vigroux, L., Virique, E., Voellmer, G., Walker, H., Ward, R., Waskett, T., Weilert, M., Wesson, R., White, G. J., Whitehouse, N., Wilson, C. D., Winter, B., Woodcraft, A. L., Wright, G. S., Xu, C. K., Zavagno, A., Zemcov, M., Zhang, L., and Zonca, E. (2010). The Herschel -SPIRE instrument and its in-flight performance. *Astron. Astrophys.*, 518(4). 23, 52

Gruppioni, C., Pozzi, F., Rodighiero, G., Delvecchio, I., Berta, S., Pozzetti, L., Zamorani, G., Andreani, P., Cimatti, A., Ilbert, O., Le Floc'h, E., Lutz, D., Magnelli, B., Marchetti, L., Monaco, P., Nordon, R., Oliver, S., Popesso, P., Riguccini, L., Roseboom, I., Rosario, D. J., Sargent, M., Vaccari, M., Altieri, B., Aussel, H., Bongiovanni, A., Cepa, J., Daddi, E., Domínguez-Sánchez, H., Elbaz, D., Schreiber, N. F., Genzel, R., Iribarrem, A., Magliocchetti, M., Maiolino, R., Poglitsch, A., García, A. P., Sanchez-Portal, M., Sturm, E., Tacconi, L., Valtchanov, I., Amblard, A., Arumugam, V., Bethermin, M., Bock, J., Boselli, A., Buat, V., Burgarella, D., Castro-Rodríguez, N., Cava, A., Chanial, P., Clements, D. L., Conley, A., Cooray, A., Dowell, C. D., Dwek, E., Eales, S., Franceschini, A., Glenn, J., Griffin, M., Hatziminaoglou, E., Ibar, E., Isaak, K., Ivison, R. J., Lagache, G., Levenson, L., Lu, N., Madden, S., Maffei, B., Mainetti, G., Nguyen, H. T., O'Halloran, B., Page, M. J., Panuzzo, P., Papageorgiou, A., Pearson, C. P., Pérez-Fournon, I., Pohlen, M., Rigopoulou, D., Rowan-Robinson, M., Schulz, B., Scott, D., Seymour, N., Shupe, D. L., Smith, A. J., Stevens, J. A., Symeonidis, M., Trichas, M., Tugwell, K. E., Vigroux, L., Wang, L., Wright, G., Xu, C. K., Zemcov, M., Bardelli, S., Carollo, M., Contini, T., Le Févre, O., Lilly, S., Mainieri, V., Renzini, A., Scodeggio, M., and Zucca, E. (2013). The Herschel* PEP/HerMES luminosity function - I. Probing the evolution of PACS selected Galaxies to z $$ 4. *Mon. Not. R. Astron. Soc.*, 432(1):23–52. 50

Guo, Q., White, S., Boylan-Kolchin, M., De Lucia, G., Kauffmann, G., Lemson, G., Li, C., Springel, V., and Weinmann, S. (2011). From dwarf spheroidals to cD galaxies:

Simulating the galaxy population in a ΛCDM cosmology. *Mon. Not. R. Astron. Soc.*, 413(1):101–131. 19

Gurkan, G., Hardcastle, M. J., Smith, D. J. B., Best, P. N., Bourne, N., Calistro-Rivera, G., Heald, G., Jarvis, M. J., Prandoni, I., Rottgering, H. J. A., Sabater, J., Shimwell, T., Tasse, C., and Williams, W. L. (2018). LOFAR/H-ATLAS: The low-frequency radio luminosity - star-formation rate relation. *Mon. Not. R. Astron. Soc.*, 475(3):3010–3028. 47, 50

Harrison, C. M., Alexander, D. M., Swinbank, A. M., Smail, I., Alaghband-Zadeh, S., Bauer, F. E., Chapman, S. C., Del Moro, A., Hickox, R. C., Ivison, R. J., Menéndez-Delmestre, K., Mullaney, J. R., and Nesvadba, N. P. (2012). Energetic galaxy-wide outflows in high-redshift ultraluminous infrared galaxies hosting AGN activity. *Mon. Not. R. Astron. Soc.*, 426(2):1073–1096. 16

Heesen, V., Buie, E., Huff, C. J., Perez, L. A., Woolsey, J. G., Rafferty, D. A., Basu, A., Beck, R., Brinks, E., Horellou, C., Scannapieco, E., Brüggen, M., Dettmar, R. J., Sendlinger, K., Nikiel-Wroczyński, B., Chy, K. T., Best, P. N., Heald, G. H., and Paladino, R. (2019). Calibrating the relation of low-frequency radio continuum to star formation rate at 1 kpc scale with LOFAR. *Astron. Astrophys.*, 622:8. 49

Helou, G. and Bicay, M. D. (2002). A physical model of the infrared-to-radio correlation in galaxies. *Astrophys. J.*, 415:93. 47

Hewett, P. C., Warren, S. J., Leggett, S. K., and Hodgkin, S. T. (2006). The UKIRT Infrared Deep Sky Survey ZY JHK photometric system: Passbands and synthetic colours. *Mon. Not. R. Astron. Soc.*, 367(2):454–468. 33

Hildebrandt, H., Choi, A., Heymans, C., Blake, C., Erben, T., Miller, L., Nakajima, R., van Waerbeke, L., Viola, M., Buddendiek, A., Harnois-Déraps, J., Hojjati, A., Joachimi, B., Joudaki, S., Kitching, T. D., Wolf, C., Gwyn, S., Johnson, N., Kuijken, K., Sheikhbahaee, Z., Tudorica, A., and Yee, H. K. (2016). RCSLenS: The Red Cluster Sequence Lensing Survey. *Mon. Not. R. Astron. Soc.*, 463(1):635–654. 32

HöGBOM, J. (1974). Aperture synthesis with a non-regular distribution of interferometer baselines. *J. Chem. Inf. Model.*, 53(9):1689–1699. 89

Hurley, P. D., Oliver, S., Betancourt, M., Clarke, C., Cowley, W. I., Duivenvoorden, S., Farrah, D., Griffin, M., Lacey, C., Le Floc'h, E., Papadopoulos, A., Sargent, M., Scudder, J. M., Vaccari, M., Valtchanov, I., and Wang, L. (2017). HELP: XID+, the probabilistic de-blender for Herschel SPIRE maps. *Mon. Not. R. Astron. Soc.*, 464(1):885–896. 24, 50, 52, 88

Jansky, K. G. (1933). Electrical phenomena that apparently are of interstellar origin. *Pop. Astron.*, 41:548. 13

Kaplan E. L. and Meier Poul (1958). Nonparametric Estimation from Incomplete Observations. *J. Am. Stat. Assoc.*, 53(282):457–481. 62

Kennicutt, Jr., R. C. (1998). The Global Schmidt Law in Star-forming Galaxies. *Astrophys. J.*, 498(2):541–552. 5, 79

Kondapally, R., Best, P. N., Hardcastle, M. J., Nisbet, D., Bonato, M., Sabater, J., Duncan, K. J., McCheyne, I., Cochrane, R. K., A Bowler, R. A., Williams, W. L., Shimwell, T. W., Tasse, C., Croston, J. H., Goyal, A., Jamrozy, M., Jarvis, M. J., Mahatma, V. H., A Röttgering, H. J., B Smith, D. J., Wołowska, A., Bondi, M., Brienza, M., I Brown, M. J., Brüggen, M., Chambers, K., Garrett, M. A., Gürkan, G., Huber, M., Kunert-Bajraszewska, M., Magnier, E., Mingo, B., Mostert, R., Nikiel-Wroczy, B., Paladino, R., Ploeckinger, T., Prandoni, I., Rosenthal, M. J., Schwarz, D. J., Shulevski, A., Wagenveld, J. D., and Wang, L. (2021). The LOFAR Two-meter Sky Survey: Deep Fields Data Release 1 III. Host-galaxy identifications and value added catalogues. *Astron. Astrophys.*, 648. 27, 28, 32, 34, 38, 44, 51, 52, 55, 57, 81

Körding, E. G., Jester, S., and Fender, R. (2008). Measuring the accretion rate and kinetic luminosity functions of supermassive black holes. *Mon. Not. R. Astron. Soc.*, 383(1):277–288. 21

Kroupa, P. (2001). On the variation of the initial mass function. *Mon. Not. R. Astron. Soc.*, 322(2):231–246. 4

Lacki, B. C., Thompson, T. A., and Quataert, E. (2010). The physics of the far-infrared-radio correlation. I. Calorimetry, conspiracy, and implications. *Astrophys. J.*, 717(1):1–28. 48, 49, 60, 80

Lawrence, A., Warren, S. J., Almaini, O., Edge, A. C., Hambly, N. C., Jameson, R. F., Lucas, P., Casali, M., Adamson, A., Dye, S., Emerson, J. P., Foucaud, S., Hewett, P., Hirst, P., Hodgkin, S. T., Irwin, M. J., Lodieu, N., McMahon, R. G., Simpson, C., Smail, I., Mortlock, D., and Folger, M. (2007). The UKIRT infrared deep sky survey (UKIDSS). *Mon. Not. R. Astron. Soc.*, 379(4):1599–1617. 33

Leslie, S. K., Schinnerer, E., Liu, D., Magnelli, B., Algera, H., Karim, A., Davidzon, I., Gozaliasl, G., Jiménez-Andrade, E. F., Lang, P., Sargent, M. T., Novak, M., Groves, B., Smolčić, V., Zamorani, G., Vaccari, M., Battisti, A., Vardoulaki, E., Peng, Y., and Kartaltepe, J. (2020). The VLA-COSMOS 3 GHz Large Project: Evolution of Specific Star Formation Rates out to z 5. *Astrophys. J.*, 899(1):58. xiii, 74, 79, 82

Li, D. and Pan, Z. (2016). The Five-hundred-meter Aperture Spherical Radio Telescope project. *Radio Sci.*, 51(7):1060–1064. 25

Liu, D., Daddi, E., Dickinson, M., Owen, F., Pannella, M., Sargent, M., Béthermin, M., Magdis, G., Gao, Y., Shu, X., Wang, T., Jin, S., and Inami, H. (2018). "Super-deblended" Dust Emission in Galaxies. I. The GOODS-North Catalog and the Cosmic Star Formation Rate Density out to Redshift 6. *Astrophys. J.*, 853(2):172. 100

Lonsdale, C. J., Smith, H. E., Rowan-Robinson, M., Surace, J., Shupe, D., Xu, C., Oliver, S., Padgett, D., Fang, F., Conrow, T., Franceschini, A., Gautier, N., Griffin, M., Hacking, P., Masci, F., Morrison, G., O'Linger, J., Owen, F., Pérez-Fournon, I., Pierre, M., Puetter, R., Stacey, G., Castro, S., Del Carmen Polletta, M., Farrah, D., Jarrett, T., Frayer, D., Siana, B., Babbedge, T., Dye, S., Fox, M., Gonzalez-Solares, E., Salaman, M., Berta, S., Condon, J. J., Dole, H., and Serjeant, S. (2003). SWIRE: The SIRTF Wide-Area Infrared Extragalactic Survey. *Publ. Astron. Soc. Pacific*, 115(810):897–927. 33

Magnelli, B., Ivison, R. J., Lutz, D., Valtchanov, I., Farrah, D., Berta, S., Bertoldi, F., Bock, J., Cooray, A., Ibar, E., Karim, A., Le Floc'h, E., Nordon, R., Oliver, S. J., Page, M., Popesso, P., Pozzi, F., Rigopoulou, D., Riguccini, L., Rodighiero, G., Rosario, D., Roseboom, I., Wang, L., and Wuyts, S. (2015). The far-infrared/radio correlation and radio spectral index of galaxies in the SFR-Mplane up to z˜2. *Astron. Astrophys.*, 573:45. 48, 60, 80

Malefahlo, E., Santos, M. G., Jarvis, M. J., White, S. V., and Zwart, J. T. (2020). The optically selected 1.4-GHz quasar luminosity function below 1 mJy. *Mon. Not. R. Astron. Soc.*, 492(4):5297–5312. 101

Małek, K., Buat, V., Burgarella, D., Roehlly, Y., and Shirley, R. (2019). HELP project - a dreamed-of multiwavelength dataset for SED fitting: The influence of used models for the main physical properties of galaxies. *Proc. Int. Astron. Union*, 15(S341):39–43. 10, 60

Mandal, S., Prandoni, I., Hardcastle, M. J., Shimwell, T. W., Intema, H. T., Tasse, C., van Weeren, R. J., Algera, H., Emig, K. L., Röttgering, H. J. A., Schwarz, D. J., Siewert, T. M., Best, P. N., Bonato, M., Bondi, M., Jarvis, M. J., Kondapally, R., Leslie, S. K., Mahatma, V. H., Sabater, J., Retana-Montenegro, E., and Williams, W. L. (2021). Extremely deep 150 MHz source counts from the LoTSS Deep Fields. *Astron. Astrophys.*, 648:A5. 52

Martin, D. C., Fanson, J., Schiminovich, D., Morrissey, P., Friedman, P. G., Barlow, T. A., Conrow, T., Grange, R., Jelinsky, P. N., Milliard, B., Siegmund, O. H. W., Bianchi, L., Byun, Y.-I., Donas, J., Forster, K., Heckman, T. M., Lee, Y.-W., Madore, B. F., Malina, R. F., Neff, S. G., Rich, R. M., Small, T., Surber, F., Szalay, A. S., Welsh, B., Wyder, T. K., and Al, M. E. T. (2005). The galexy evolution explorer: galex documentation. *Astrophys. J.*, 619(2000):1–6. 32

Mauch, T. and Sadler, E. M. (2007). Radio sources in the 6dFGS: local luminosity functions at 1.4 GHz for star-forming galaxies and radio-loud AGN. *Mon. Not. R. Astron. Soc*, 375:931–950. 21

Mauduit, J.-C., Lacy, M., Farrah, D., Surace, J. A., Jarvis, M., Oliver, S., Maraston, C., Vaccari, M., Marchetti, L., Zeimann, G., Gonzáles-Solares, E. A., Pforr, J., Petric, A. O., Henriques, B., Thomas, P. A., Afonso, J., Rettura, A., Wilson, G., Falder, J. T., Geach, J. E., Huynh, M., Norris, R. P., Seymour, N., Richards, G. T., Stanford, S. A., Alexander, D. M., Becker, R. H., Best, P. N., Bizzocchi, L., Bonfield, D., Castro, N., Cava, A., Chapman, S., Christopher, N., Clements, D. L., Covone, G., Dubois, N., Dunlop, J. S., Dyke, E., Edge, A., Ferguson, H. C., Foucaud, S., Franceschini, A., Gal, R. R., Grant, J. K., Grossi, M., Hatziminaoglou, E., Hickey, S., Hodge, J. A., Huang, J.-S., Ivison, R. J., Kim, M., LeFevre, O., Lehnert, M., Lonsdale, C. J., Lubin, L. M., McLure, R. J., Messias, H., Martínez-Sansigre, A., Mortier, A. M. J., Nielsen, D. M., Ouchi, M., Parish, G., Perez-Fournon, I., Pierre, M., Rawlings, S., Readhead, A., Ridgway, S. E., Rigopoulou, D., Romer, A. K., Rosebloom, I. G., Rottgering, H. J. A., Rowan-Robinson, M., Sajina, A., Simpson, C. J., Smail, I., Squires, G. K., Stevens, J. A., Taylor, R., Trichas, M., Urrutia, T., van Kampen, E., Verma, A., and Xu, C. K. (2012). The Spitzer Extragalactic Representative Volume Survey (SERVS): Survey Definition and Goals*. *Publ. Astron. Soc. Pacific*, 124(917):714–736. 33

Mcalpine, K., Smith, D. J., Jarvis, M. J., Bonfield, D. G., and Fleuren, S. (2012). The likelihood ratio as a tool for radio continuum surveys with Square Kilometre Array precursor telescopes. *Mon. Not. R. Astron. Soc.*, 423(1):132–140. 28

Miller, G. E. and Scalo, J. M. (1979). The initial mass function and stellar birthrate in the solar neighborhood. *Astrophys. J. Suppl. Ser.*, 41:513. 4

Mohan, N. and Rafferty, D. (2015). PyBDSM: Python Blob Detection and Source Finder. *Astrophys. Source Code Libr.*, page ascl:1502.007. 37, 91

Molnár, D. C., Sargent, M. T., Delhaize, J., Delvecchio, I., Smolcić, V., Novak, M., Schinnerer, E., Zamorani, G., Bondi, M., Herrera-Ruiz, N., Murphy, E. J., Vardoulaki, E., Karim, A., Leslie, S., Magnelli, B., Carollo, C. M., and Middelberg, E. (2018). The infrared-radio correlation of spheroid-and disc-dominated star-forming galaxies to z ˜ 1.5 in the COSMOS field. *Mon. Not. R. Astron. Soc.*, 475(1):827–838. 50

Molnár, D. C., Sargent, M. T., Elbaz, D., Papadopoulos, P. P., and Silk, J. (2017). Further evidence for a quasar-driven jet impacting its neighbour galaxy: The saga of HE04502958 continues. *Mon. Not. R. Astron. Soc.*, 467(1):586–596. 17

Molnár, D. C., Sargent, M. T., Leslie, S., Magnelli, B., Schinnerer, E., Zamorani, G., Delhaize, J., Smolčić, V., Tisanić, K., and Vardoulaki, E. (2021). The non-linear infrared-radio correlation of low-z galaxies: Implications for redshift evolution, a new radio SFR recipe, and how to minimize selection bias. *Mon. Not. R. Astron. Soc.*, 504(1):118–145. xii, 68, 75, 82

Morrissey, P., Conrow, T., Barlow, T. A., Small, T., Seibert, M., Wyder, T. K., Budavari, T., Arnouts, S., Friedman, P. G., Forster, K., Martin, D. C., Neff, S. G., Schiminovich, D., Bianchi, L., Donas, J., Heckman, T. M., Lee, Y.-W., Madore, B. F., Milliard, B., Rich, R. M., Szalay, A. S., Welsh, B. Y., and Yi, S. K. (2007). The Calibration and Data Products of GALEX. *Astrophys. J. Suppl. Ser.*, 173(2):682–697. 32

Murphy, E. J. (2009). The far-infrared-radio correlation at high redshifts: Physical considerations and prospects for the square kilometer array. *Astrophys. J.*, 706(1):482–496. 47, 49

Muzzin, A., Wilson, G., Yee, H. K., Hoekstra, H., Gilbank, D., Surace, J., Lacy, M., Blindert, K., Majumdar, S., Demarco, R., Gardner, J. P., Gladders, M., and Lonsdale, C. (2009). Spectroscopic confirmation of two massive red-sequence-selected galaxy clusters at z 1.2 in the SpARCS-north cluster survey. 32

Nguyen, H. T., Schulz, B., Levenson, L., Amblard, A., Arumugam, V., Aussel, H., Babbedge, T., Blain, A., Bock, J., Boselli, A., Buat, V., Castro-Rodriguez, N., Cava, A., Chanial, P., Chapin, E., Clements, D. L., Conley, A., Conversi, L., Cooray, A., Dowell, C. D., Dwek, E., Eales, S., Elbaz, D., Fox, M., Franceschini, A., Gear, W., Glenn, J., Griffin, M., Halpern, M., Hatziminaoglou, E., Ibar, E., Isaak, K., Ivison, R. J., Lagache, G., Lu, N., Madden, S., Maffei, B., Mainetti, G., Marchetti, L., Marsden, G., Marshall, J., O'Halloran, B., Oliver, S. J., Omont, A., Page, M. J., Panuzzo, P., Papageorgiou, A., Pearson, C. P., Perez Fournon, I., Pohlen, M., Rangwala, N., Rigopoulou, D., Rizzo, D., Roseboom, I. G., Rowan-Robinson, M., Scott, D., Seymour, N., Shupe, D. L., Smith, A. J., Stevens, J. A., Symeonidis, M., Trichas, M., Tugwell, K. E., Vaccari, M., Valtchanov, I., Vigroux, L., Wang, L., Ward, R., Wiebe, D., Wright, G., Xu, C. K., and Zemcov, M. (2010). HerMES: The SPIRE confusion limit. *Astron. Astrophys.*, 518(8):5. 24

Nisbet, D. M. (2018). Role of active galactic nuclei in galaxy evolution. *PhD Thesis*. 31, 38

Oliver, S. J., Bock, J., Altieri, B., Amblard, A., Arumugam, V., Aussel, H., Babbedge, T., Beelen, A., Béthermin, M., Blain, A., Boselli, A., Bridge, C., Brisbin, D., Buat, V., Burgarella, D., Castro-Rodríguez, N., Cava, A., Chanial, P., Cirasuolo, M., Clements, D. L., Conley, A., Conversi, L., Cooray, A., Dowell, C. D., Dubois, E. N., Dwek, E., Dye, S., Eales, S., Elbaz, D., Farrah, D., Feltre, A., Ferrero, P., Fiolet, N., Fox, M., Franceschini, A., Gear, W., Giovannoli, E., Glenn, J., Gong, Y., González Solares, E. A., Griffin, M., Halpern, M., Harwit, M., Hatziminaoglou, E., Heinis, S., Hurley, P., Hwang, H. S., Hyde, A., Ibar, E., Ilbert, O., Isaak, K., Ivison, R. J., Lagache, G., Le Floc'h, E., Levenson, L., Faro, B. L., Lu, N., Madden, S., Maffei, B., Magdis, G., Mainetti, G., Marchetti, L., Marsden, G., Marshall, J., Mortier, A. M., Nguyen, H. T., O'Halloran, B., Omont, A., Page, M. J., Panuzzo, P., Papageorgiou, A., Patel, H., Pearson, C. P., Pérez-Fournon, I., Pohlen, M., Rawlings, J. I., Raymond, G., Rigopoulou, D., Riguccini, L., Rizzo, D., Rodighiero, G., Roseboom, I. G., Rowan-Robinson, M., Sánchez Portal, M., Schulz, B., Scott, D., Seymour, N., Shupe, D. L., Smith, A. J., Stevens, J. A., Symeonidis, M., Trichas, M., Tugwell, K. E., Vaccari, M., Valtchanov, I., Vieira, J. D., Viero, M., Vigroux, L., Wang, L., Ward, R., Wardlow, J., Wright, G., Xu, C. K., and Zemcov, M. (2012). The Herschel Multi-tiered Extragalactic Survey: HerMES. *Mon. Not. R. Astron. Soc.*, 424(3):1614–1635. 52, 81

Pérez-Torres, M., Mattila, S., Alonso-Herrero, A., Aalto, S., and Efstathiou, A. (2021). Star formation and nuclear activity in luminous infrared galaxies: an infrared through radio review. 16

Pilbratt, G. L., Riedinger, J. R., Passvogel, T., Crone, G., Doyle, D., Gageur, U., Heras, A. M., Jewell, C., Metcalfe, L., Ott, S., and Schmidt, M. (2010). Herschel Space Observatory. *Astron. Astrophys.*, 518(7-8):1. 23, 53

Poglitsch, A., Waelkens, C., Geis, N., Feuchtgruber, H., Van Den Bussche, B., Rodriguez, L., Krause, O., Renotte, E., Van Hoof, C., Saraceno, P., Cepa, J., Kerschbaum, F., Agnèse, P., Ali, B., Altieri, B., Andreani, P., Augueres, J. L., Balog, Z., Barl, L., Bauer, O. H., Belbachir, N., Benedettini, M., Billot, N., Boulade, O., Bischof, H., Blommaert, J., Callut, E., Cara, C., Cerulli, R., Cesarsky, D., Contursi, A., Creten, Y., De Meester, W., Doublier, V., Doumayrou, E., Duband, L., Exter, K., Genzel, R., Gillis, J. M., Grözinger, U., Henning, T., Herreros, J., Huygen, R., Inguscio, M., Jakob, G., Jamar, C., Jean, C., De Jong, J., Katterloher, R., Kiss, C., Klaas, U., Lemke, D., Lutz, D., Madden, S., Marquet, B., Martignac, J., Mazy, A., Merken, P., Montfort, F., Morbidelli, L., Müller, T., Nielbock, M., Okumura, K., Orfei, R., Ottensamer, R., Pezzuto, S., Popesso, P., Putzeys, J., Regibo, S., Reveret, V., Royer, P., Sauvage, M., Schreiber, J., Stegmaier, J., Schmitt, D., Schubert, J., Sturm, E., Thiel, M., Tofani, G., Vavrek, R., Wetzstein, M., Wieprecht, E., and Wiezorrek, E. (2010). The photodetector array camera and Spectrometer (PACS) on the herschel space observatory. *Astron. Astrophys.*, 518(4):L2. 23, 52

Pozzetti, L., Bolzonella, M., Zucca, E., Zamorani, G., Lilly, S., Renzini, A., Moresco, M., Mignoli, M., Cassata, P., Tasca, L., Lamareille, F., Maier, C., Meneux, B., Halliday, C., Oesch, P., Vergani, D., Caputi, K., Kovač, K., Cimatti, A., Cucciati, O., Iovino, A., Peng, Y., Carollo, M., Contini, T., Kneib, J. P., Le Févre, O., Mainieri, V., Scodeggio, M., Bardelli, S., Bongiorno, A., Coppa, G., De La Torre, S., De Ravel, L., Franzetti, P., Garilli, B., Kampczyk, P., Knobel, C., Le Borgne, J. F., Le Brun, V., Pellò, R., Perez Montero, E., Ricciardelli, E., Silverman, J. D., Tanaka, M., Tresse, L., Abbas, U., Bottini, D., Cappi, A., Guzzo, L., Koekemoer, A. M., Leauthaud, A., MacCagni, D., Marinoni, C., McCracken, H. J., Memeo, P., Porciani, C., Scaramella, R., Scarlata, C., and Scoville, N. (2010). ZCOSMOS - 10k-bright spectroscopic sample: The bimodality in the galaxy stellar mass function: Exploring its evolution with redshift. *Astron. Astrophys.*, 523(1):13. 59

Ramasawmy, J., Geach, J. E., Hardcastle, M. J., Best, P. N., Bonato, M., Bondi, M., Calistro Rivera, G., Cochrane, R. K., Conway, J. E., Coppin, K., Duncan, K. J., Dunlop, J. S., Franco, M., García-Vergara, C., Jarvis, M. J., Kondapally, R., McCheyne, I., Prandoni, I., Röttgering, H. J., Smith, D. J., Tasse, C., and Wang, L. (2021). Low-frequency radio spectra of submillimetre galaxies in the Lockman Hole. *Astron. Astrophys.*, 648:A14. 54

Read, S. C., Smith, D. J., Gürkan, G., Hardcastle, M. J., Williams, W. L., Best, P. N., Brinks, E., Calistro-Rivera, G., Chyzy, K. T., Duncan, K., Dunne, L., Jarvis, M. J., Morabito, L. K., Prandoni, I., Röttgering, H. J., Sabater, J., and Viaene, S. (2018). The Far-Infrared Radio Correlation at low radio frequency with LOFAR/H-ATLAS. *Mon. Not. R. Astron. Soc.*, 480(4):5625–5644. 49, 50

Rieke, G. H., Young, E. T., Engelbracht, C. W., Kelly, D. M., Low, F. J., Haller, E. E., Beeman, J. W., Gordon, K. D., Stansberry, J. A., Misselt, K. A., Cadien, J., Morrison, J. E., Rivlis, G., Latter, W. B., Noriega-Crespo, A., Padgett, D. L., Stapelfeldt, K. R., Hines, D. C., Egami, E., Muzerolle, J., Alonso-Herrero, A., Blaylock, M., Dole, H., Hinz, J. L., Le Floc'h, E., Papovich, C., Perez-Gonzalez, P. G., Smith, P. S., Su, K. Y. L., Bennett, L., Frayer, D. T., Henderson, D., Lu, N., Masci, F., Pesenson, M., Rebull, L., Rho, J., Keene, J., Stolovy, S., Wachter, S., Wheaton, W., Werner, M. W., and Richards, P. L. (2004). The Multiband Imaging Photometer for Spitzer (MIPS). *Astrophys. J. Suppl. Ser.*, 154(1):25–29. 52, 83

Roseboom, I. G., Oliver, S. J., Kunz, M., Altieri, B., Amblard, A., Arumugam, V., Auld, R., Aussel, H., Babbedge, T., Béthermin, M., Blain, A., Bock, J., Boselli, A., Brisbin, D., Buat, V., Burgarella, D., Castro-Rodríguez, N., Cava, A., Chanial, P., Chapin, E., Clements, D. L., Conley, A., Conversi, L., Cooray, A., Dowell, C. D., Dwek, E., Dye, S., Eales, S., Elbaz, D., Farrah, D., Fox, M., Franceschini, A., Gear, W., Glenn, J., Solares, E. A., Griffin, M., Halpern, M., Harwit, M., Hatziminaoglou, E., Huang, J., Ibar, E., Isaak, K., Ivison, R. J., Lagache, G., Levenson, L., Lu, N., Madden, S., Maffei, B., Mainetti, G., Marchetti, L., Marsden, G., Mortier, A. M., Nguyen, H. T., O'Halloran, B., Omont, A., Page, M. J., Panuzzo, P., Papageorgiou, A., Patel, H., Pearson, C. P., Pérez-Fournon, I., Pohlen, M., Rawlings, J. I., Raymond, G., Rigopoulou, D., Rizzo, D., Rowan-Robinson, M., Portal, M. S., Schulz, B., Scott, D., Seymour, N., Shupe, D. L., Smith, A. J., Stevens, J. A., Symeonidis, M., Trichas, M., Tugwell, K. E., Vaccari, M., Valtchanov, I., Vieira, J. D., Vigroux, L., Wang, L., Ward, R., Wright, G., Xu, C. K., and Zemcov, M. (2010). The Herschel Multi-Tiered Extragalactic Survey: Source extraction and cross-identifications in confusion-dominated SPIRE images. *Mon. Not. R. Astron. Soc.*, 409(1):48–65. 24

Röttgering, H. J. and Bremer, M. A. (1997). The Westerbork Northern Sky Survey (WENSS): I. A 570 square degree Mini-Survey around the North Ecliptic Pole. *Astron. Astrophys. Suppl. Ser.*, 124(2):259–280. 38

Sabater, J., Best, P. N., Hardcastle, M. J., Shimwell, T. W., Tasse, C., Williams, W. L., Brüggen, M., Cochrane, R. K., Croston, J. H., De Gasperin, F., Duncan, K. J., Gürkan, G., Mechev, A. P., Morabito, L. K., Prandoni, I., Röttgering, H. J., Smith, D. J., Harwood, J. J., Mingo, B., Mooney, S., and Saxena, A. (2020). The LoTSS view of radio AGN in the local Universe: The most massive galaxies are always switched on. 45, 50, 80

Sabater, J., Best, P. N., Tasse, C., Hardcastle, M. J., Shimwell, T. W., Nisbet, D., Jelic, V., Callingham, J. R., Röttgering, H. J. A., Bonato, M., Bondi, M., Ciardi, B., Cochrane, R. K., Jarvis, M. J., Kondapally, R., Koopmans, L. V. E., O'sullivan, S. P., Prandoni, I., Schwarz, D. J., Smith, D. J. B., Wang, L., Williams, W. L., and Zaroubi, S. (2021). The LOFAR Two-meter Sky Survey: Deep Fields Data Release 1 II. The ELAIS-N1 LOFAR deep field. *Astron. Astrophys.*, 648. 50, 51, 61

Safarzadeh, M., Ferguson, H. C., Lu, Y., Inami, H., and Somerville, R. S. (2014). A NOVEL TECHNIQUE TO IMPROVE PHOTOMETRY IN CONFUSED IMAGES USING GRAPHS AND BAYESIAN PRIORS. *Astrophys. J.*, 798(7pp):91. 53

Salpeter, E. E. (1955). THE LUMINOSITY FUNCTION AND STELLAR EVOLUTION Edwin E. Salpeter* Australian National University, Canberra, and Cornell University Received July 29, 1954. *Astrophys. J.*, 121:161–167. 4

Sargent, M. T., Daddi, E., Béthermin, M., Aussel, H., Magdis, G., Hwang, H. S., Juneau, S., Elbaz, D., and Da Cunha, E. (2014). REGULARITY UNDERLYING COMPLEXITY: A REDSHIFT-INDEPENDENT DESCRIPTION OF THE CONTINUOUS VARIATION OF GALAXY-SCALE MOLECULAR GAS PROPERTIES IN THE MASS-STAR FORMATION RATE PLANE. *Astrophys. J.*, 793(34pp):19. 60

Sargent, M. T., Schinnerer, E., Murphy, E., Carilli, C. L., Helou, G., Aussel, H., Le Floc'H, E., Frayer, D. T., Ilbert, O., Oesch, P., Salvato, M., Smolčić, V., Kartaltepe, J., and Sanders, D. B. (2010). No evolution in the IR-radio relation for IR-luminous galaxies at z < 2 in the cosmos field. *Astrophys. J. Lett.*, 714(2 PART 2):190–195. 47, 49, 50

Savage, R. S. and Oliver, S. (2007). Bayesian Methods of Astronomical Source Extraction. *Astrophys. J.*, 661(2):1339–1346. 24

Schaye, J., Crain, R. A., Bower, R. G., Furlong, M., Schaller, M., Theuns, T., Dalla Vecchia, C., Frenk, C. S., Mccarthy, I. G., Helly, J. C., Jenkins, A., Rosas-Guevara, Y. M., White, S. D., Baes, M., Booth, C. M., Camps, P., Navarro, J. F., Qu, Y., Rahmati, A., Sawala, T., Thomas, P. A., and Trayford, J. (2015). The EAGLE project: Simulating the evolution and assembly of galaxies and their environments. *Mon. Not. R. Astron. Soc.*, 446(1):521–554. 19

Schmidt, M. (1963). 3C 273: A star-like object with large red-shift. *Nature*, 197(4872):1040. 13

Schmitt, J. H. M. M. (1985). Statistical analysis of astronomical data containing upper bounds - General methods and examples drawn from X-ray astronomy. *Astrophys. J.*, 293:178. 62

Schreiber, C., Pannella, M., Elbaz, D., Béthermin, M., Inami, H., Dickinson, M., Magnelli, B., Wang, T., Aussel, H., Daddi, E., Juneau, S., Shu, X., Sargent, M. T., Buat, V., Faber, S. M., Ferguson, H. C., Giavalisco, M., Koekemoer, A. M., Magdis, G., Morrison, G. E., Papovich, C., Santini, P., and Scott, D. (2015). The Herschel view of the dominant mode of galaxy growth from z = 4 to the present day. *Astron. Astrophys.*, 575:74. xiii, 74, 79, 82

Shimwell, T. W., Röttgering, H. J., Best, P. N., Williams, W. L., Dijkema, T. J., De Gasperin, F., Hardcastle, M. J., Heald, G. H., Hoang, D. N., Horneffer, A., Intema, H., Mahony, E. K., Mandal, S., Mechev, A. P., Morabito, L., Oonk, J. B., Rafferty, D., Retana-Montenegro, E., Sabater, J., Tasse, C., Van Weeren, R. J., Brüggen, M., Brunetti, G., Chy, K. T., Conway, J. E., Haverkorn, M., Jackson, N., Jarvis, M. J., McKean, J. P., Miley, G. K., Morganti, R., White, G. J., Wise, M. W., Van Bemmel, I. M., Beck, R., Brienza, M., Bonafede, A., Calistro Rivera, G., Cassano, R., Clarke, A. O., Cseh, D., Deller, A., Drabent, A., Van Driel, W., Engels, D., Falcke, H., Ferrari, C., Fröhlich, S., Garrett, M. A., Harwood, J. J., Heesen, V., Hoeft, M., Horellou, C., Israel, F. P., Kapińska, A. D., Kunert-Bajraszewska, M., McKay, D. J., Mohan, N. R., Orrú, E., Pizzo, R. F., Prandoni, I., Schwarz, D. J., Shulevski, A., Sipior, M., Smith, D. J., Sridhar, S. S., Steinmetz, M., Stroe, A., Varenius, E., Van Der Werf, P. P., Zensus, J. A., and Zwart, J. T. (2017). The LOFAR Two-metre Sky Survey: I. Survey description and preliminary data release. *Astron. Astrophys.*, 598:104. 51

Shimwell, T. W., Tasse, C., Hardcastle, M. J., Mechev, A. P., Williams, W. L., Best, P. N., Röttgering, H. J. A., Callingham, J. R., Dijkema, T. J., de Gasperin, F., Hoang, D. N., Hugo, B., Mirmont, M., Oonk, J. B. R., Prandoni, I., Rafferty, D., Sabater, J., Smirnov, O., van Weeren, R. J., White, G. J., Atemkeng, M., Bester, L., Bonnassieux, E., Brüggen, M., Brunetti, G., Chyży, K. T., Cochrane, R., Conway, J. E., Croston, J. H., Danezi, A., Duncan, K., Haverkorn, M., Heald, G. H., Iacobelli, M., Intema, H. T., Jackson, N., Jamrozy, M., Jarvis, M. J., Lakhoo, R., Mevius, M., Miley, G. K., Morabito, L., Morganti, R., Nisbet, D., Orrú, E., Perkins, S., Pizzo, R. F., Schrijvers, C., Smith, D. J. B., Vermeulen, R., Wise, M. W., Alegre, L., Bacon, D. J., van Bemmel, I. M., Beswick, R. J., Bonafede, A., Botteon, A., Bourke, S., Brienza, M., Calistro Rivera, G., Cassano, R., Clarke, A. O., Conselice, C. J., Dettmar, R. J., Drabent, A., Dumba, C., Emig, K. L., Enßlin, T. A., Ferrari, C., Garrett, M. A., Génova-Santos, R. T., Goyal, A., Gürkan, G., Hale, C., Harwood, J. J., Heesen, V., Hoeft, M., Horellou, C., Jackson, C., Kokotanekov, G., Kondapally, R., Kunert-Bajraszewska, M., Mahatma, V., Mahony, E. K., Mandal, S., McKean, J. P., Merloni, A., Mingo, B., Miskolczi, A., Mooney, S., Nikiel-Wroczyński, B., O'Sullivan, S. P., Quinn, J., Reich, W., Roskowiński, C., Rowlinson, A., Savini, F., Saxena, A., Schwarz, D. J., Shulevski, A., Sridhar, S. S., Stacey, H. R., Urquhart, S., van der Wiel, M. H. D., Varenius, E., Webster, B., and Wilber, A. (2019). The LOFAR Two-metre Sky Survey. *Astron. Astrophys.*, 622:A1. 48, 81

Shirley, R., Roehlly, Y., Hurley, P. D., Buat, V., Del Carmen Campos Varillas, M., Duivenvoorden, S., Duncan, K. J., Efstathiou, A., Farrah, D., Solares, E. G., Malek, K., Marchetti, L., McCheyne, I., Papadopoulos, A., Pons, E., Scipioni, R., Vaccari, M., and Oliver, S. (2019). Help: A catalogue of 170 million objects, selected at 0.36–4.5 μm, from 1270 deg2 of prime extragalactic fields. *Mon. Not. R. Astron. Soc.*, 490(1):634–656. 53

Smith, D. J., Dunne, L., da Cunha, E., Rowlands, K., Maddox, S. J., Gomez, H. L., Bonfield, D. G., Charlot, S., Driver, S. P., Popescu, C. C., Tuffs, R. J., Dunlop, J. S., Jarvis, M. J., Seymour, N., Symeonidis, M., Baes, M., Bourne, N., Clements, D. L., Cooray, A., De Zotti, G., Dye, S., Eales, S., Scott, D., Verma, A., van der Werf, P., Andrae, E., Auld, R., Buttiglione, S., Cava, A., Dariush, A., Fritz, J., Hopwood, R., Ibar, E., Ivison, R. J., Kelvin, L., Madore, B. F., Pohlen, M., Rigby, E. E., Robotham, A., Seibert, M., and Temi, P. (2012). Herschel-ATLAS: Multi-wavelength SEDs and physical properties of 250 μm selected galaxies at z < 0.5. *Mon. Not. R. Astron. Soc.*, 427(1):703–727. 61

Smith, D. J., Dunne, L., Maddox, S. J., Eales, S., Bonfield, D. G., Jarvis, M. J., Sutherland, W., Fleuren, S., Rigby, E. E., Thompson, M. A., Baldry, I. K., Bamford, S., Buttiglione, S., Cava, A., Clements, D. L., Cooray, A., Croom, S., Dariush, A., de Zotti, G., Driver, S. P., Dunlop, J. S., Fritz, J., Hill, D. T., Hopkins, A., Hopwood, R., Ibar, E., Ivison, R. J., Jones, D. H., Kelvin, L., Leeuw, L., Liske, J., Loveday, J., Madore, B. F., Norberg, P., Panuzzo, P., Pascale, E., Pohlen, M., Popescu, C. C., Prescott, M., Robotham, A., Rodighiero, G., Scott, D., Seibert, M., Sharp, R., Temi, P., Tuffs, R. J., van der Werf, P., and van Kampen, E. (2011). Herschel-ATLAS: Counterparts from the ultraviolet-near-infrared in the science demonstration phase catalogue. *Mon. Not. R. Astron. Soc.*, 416(2):857–872. 28

Smith, D. J., Jarvis, M. J., Hardcastle, M. J., Vaccari, M., Bourne, N., Dunne, L., Ibar, E., Maddox, N., Prescott, M., Vlahakis, C., Eales, S., Maddox, S. J., Smith, M. W., Valiante, E., and de Zotti, G. (2014). The temperature dependence of the far-infrared-radio correlation in the Herschel-ATLAS. *Mon. Not. R. Astron. Soc.*, 445(3):2232–2243. 49

Smith, D. J. B., Haskell, P., Gürkan, G., Best, P. N., Hardcastle, M. J., Kondapally, R., Williams, W., Duncan, K. J., Cochrane, R. K., McCheyne, I., Röttgering, H. J. A., Sabater, J., Shimwell, T. W., Tasse, C., Bonato, M., Bondi, M., Jarvis, M. J., Leslie, S. K., Prandoni, I., and Wang, L. (2021). The LOFAR Two-metre Sky Survey Deep Fields. *Astron. Astrophys.*, 648:A6. xi, xii, 49, 50, 59, 62, 66, 71, 82, 83

Smolčić, V., Novak, M., Delvecchio, I., Ceraj, L., Bondi, M., Delhaize, J., Marchesi, S., Murphy, E., Schinnerer, E., Vardoulaki, E., and Zamorani, G. (2017). The VLA-COSMOS 3 GHz Large Project: Cosmic evolution of radio AGN and implications for radio-mode feedback since z ˜ 5. *Astron. Astrophys.*, 602:6. 50

Springel, V., White, S. D., Jenkins, A., Frenk, C. S., Yoshida, N., Gao, L., Navarro, J., Thacker, R., Croton, D., Helly, J., Peacock, J. A., Cole, S., Thomas, P., Couchman, H., Evrard, A., Colberg, J., and Pearce, F. (2005). Simulations of the formation, evolution and clustering of galaxies and quasars. *Nature*, 435(7042):629–636. 19

Stalevski, M., Ricci, C., Ueda, Y., Lira, P., Fritz, J., and Baes, M. (2016). The dust covering factor in active galactic nuclei. *Mon. Not. R. Astron. Soc.*, 458(3):2288–2302. 55

Sutherland, W. and Saunders, W. (1992). On the likelihood ratio for source identification. *Mon. Not. R. Astron. Soc.*, 259(3):413–420. 28, 55

Symeonidis, M., Giblin, B. M., Page, M. J., Pearson, C., Bendo, G., Seymour, N., and Oliver, S. J. (2016). AGN are cooler than you think: The intrinsic far-IR emission from QSOs. *Mon. Not. R. Astron. Soc.*, 459(1):257–276. 17

Szalay, A. S., Connolly, A. J., and Szokoly, G. P. (1999). Simultaneous Multicolor Detection of Faint Galaxies in the Hubble Deep Field. *Astron. J.*, 117(1):68–74. 33

Tasse, C., Hugo, B., Mirmont, M., Smirnov, O., Atemkeng, M., Bester, L., Hardcastle, M. J., Lakhoo, R., Perkins, S., and Shimwell, T. (2018). Astronomy Faceting for direction-dependent spectral deconvolution. *Astrophys. A&A*, 611:87. 35

Tasse, C., Shimwell, T., Hardcastle, M. J., O'Sullivan, S. P., Van Weeren, R., Best, P. N., Bester, L., Hugo, B., Smirnov, O., Sabater, J., Calistro-Rivera, G., De Gasperin, F., Morabito, L. K., Röttgering, H., Williams, W. L., Bonato, M., Bondi, M., Botteon, A., Brüggen, M., Brunetti, G., Chyay, K. T., Garrett, M. A., Gürkan, G., Jarvis, M. J., Kondapally, R., Mandal, S., Prandoni, I., Repetti, A., Retana-Montenegro, E., Schwarz, D. J., Shulevski, A., and Wiaux, Y. (2021). The LOFAR Two-meter Sky Survey: Deep Fields Data Release 1: I. Direction-dependent calibration and imaging. *Astron. Astrophys.*, 648. 37, 51, 61, 89

Terzian, Y. (1972). Thermal Radio Emission from Normal Galaxies. *Symp. - Int. Astron. Union*, 44:75–81. 12, 20, 50

Thomas, N., Davé, R., Jarvis, M. J., and Anglés-Alcázar, D. (2021). The radio galaxy population in the SIMBA simulations. *Mon. Not. R. Astron. Soc.*, 503(3):3492–3509. 45

Vaccari, M. and Consortium, T. H. (2015). HELP : The Herschel Extragalactic Legacy Project & The Coming of Age of Multi-Wavelength Astrophysics. Technical report. 50

Valtchanov, I., Hopwood, R., Polehampton, E., Benielli, D., Fulton, T., Imhof, P., Konopczyński, T., Lim, T., Lu, N., Marchili, N., Naylor, D., and Swinyard, B. (2014). Relative pointing offset analysis of calibration targets with repeated observations with Herschel-SPIRE Fourier-transform spectrometer. *Exp. Astron.*, 37(2):207–223. 23

van der Kruit, P. C. (1971). Observations of Core Sources in Seyfert and Normal Galaxies with the Westerbork Synthesis Radio Telescope at 1415MHz. *Astron. Astrophys.*, 15(15):110–122. 47

Van Haarlem, M. P., Wise, M. W., Gunst, A. W., Heald, G., McKean, J. P., Hessels, J. W., De Bruyn, A. G., Nijboer, R., Swinbank, J., Fallows, R., Brentjens, M., Nelles, A., Beck, R., Falcke, H., Fender, R., Hörandel, J., Koopmans, L. V., Mann, G., Miley, G., Röttgering, H., Stappers, B. W., Wijers, R. A., Zaroubi, S., Van Den Akker, M., Alexov, A., Anderson, J., Anderson, K., Van Ardenne, A., Arts, M., Asgekar, A., Avruch, I. M., Batejat, F., Bähren, L., Bell, M. E., Bell, M. R., Van Bemmel, I., Bennema, P., Bentum, M. J., Bernardi, G., Best, P., Bîrzan, L., Bonafede, A., Boonstra, A. J., Braun, R., Bregman, J., Breitling, F., Van De Brink, R. H., Broderick, J., Broekema, P. C., Brouw, W. N., Brüggen, M., Butcher, H. R., Van Cappellen, W., Ciardi, B., Coenen, T., Conway, J., Coolen, A., Corstanje, A., Damstra, S., Davies, O., Deller, A. T., Dettmar, R. J., Van Diepen, G., Dijkstra, K., Donker, P., Doorduin, A., Dromer, J., Drost, M., Van Duin, A., Eislöffel, J., Van Enst, J., Ferrari, C., Frieswijk, W., Gankema, H., Garrett, M. A., De Gasperin, F., Gerbers, M., De Geus, E., Grießmeier, J. M., Grit, T., Gruppen, P., Hamaker, J. P., Hassall, T., Hoeft, M., Holties, H. A., Horneffer, A., Van Der Horst, A., Van Houwelingen, A., Huijgen, A., Iacobelli, M., Intema, H., Jackson, N., Jelic, V., De Jong, A., Juette, E., Kant, D., Karastergiou, A., Koers, A., Kollen, H., Kondratiev, V. I., Kooistra, E., Koopman, Y., Koster, A., Kuniyoshi, M., Kramer, M., Kuper, G., Lambropoulos, P., Law, C., Van Leeuwen, J., Lemaitre, J., Loose, M., Maat, P., Macario, G., Markoff, S., Masters, J., McFadden, R. A., McKay-Bukowski, D., Meijering, H., Meulman, H., Mevius, M., Middelberg, E., Millenaar, R., Miller-Jones, J. C., Mohan, R. N., Mol, J. D., Morawietz, J., Morganti, R., Mulcahy, D. D., Mulder, E., Munk, H., Nieuwenhuis, L., Van Nieuwpoort, R., Noordam, J. E., Norden, M., Noutsos, A., Offringa, A. R., Olofsson, H., Omar, A., Orrú, E., Overeem, R., Paas, H., Pandey-Pommier, M., Pandey, V. N., Pizzo, R., Polatidis, A., Rafferty, D., Rawlings, S., Reich, W., De Reijer, J. P., Reitsma, J., Renting, G. A., Riemers, P., Rol, E., Romein, J. W., Roosjen, J., Ruiter, M., Scaife, A., Van Der Schaaf, K., Scheers, B., Schellart, P., Schoenmakers, A., Schoonderbeek, G., Serylak, M., Shulevski, A., Sluman, J., Smirnov, O., Sobey, C., Spreeuw, H., Steinmetz, M., Sterks, C. G., Stiepel, H. J., Stuurwold, K., Tagger, M., Tang, Y., Tasse, C., Thomas, I., Thoudam, S., Toribio, M. C., Van Der Tol, B., Usov, O., Van Veelen, M., Van Der Veen, A. J., Ter Veen, S., Verbiest, J. P., Vermeulen, R., Vermaas, N., Vocks, C., Vogt, C., De Vos, M., Van Der Wal, E., Van

Weeren, R., Weggemans, H., Weltevrede, P., White, S., Wijnholds, S. J., Wilhelmsson, T., Wucknitz, O., Yatawatta, S., Zarka, P., Zensus, A., and Van Zwieten, J. (2013). LOFAR: The low-frequency array. 13, 35, 36

van Weeren, R. J., Williams, W. L., Hardcastle, M. J., Shimwell, T. W., Rafferty, D. A., Sabater, J., Heald, G., Sridhar, S. S., Dijkema, T. J., Brunetti, G., Brüggen, M., Andrade-Santos, F., Ogrean, G. A., Röttgering, H. J. A., Dawson, W. A., Forman, W. R., de Gasperin, F., Jones, C., Miley, G. K., Rudnick, L., Sarazin, C. L., Bonafede, A., Best, P. N., Bîrzan, L., Cassano, R., Chyży, K. T., Croston, J. H., Ensslin, T., Ferrari, C., Hoeft, M., Horellou, C., Jarvis, M. J., Kraft, R. P., Mevius, M., Intema, H. T., Murray, S. S., Orrú, E., Pizzo, R., Simionescu, A., Stroe, A., van der Tol, S., and White, G. J. (2016). LOFAR FACET CALIBRATION. *Astrophys. J. Suppl. Ser.*, 223(1):2. 35

Veilleux, S., Cecil, G., and Bland-Hawthorn, J. (2005). Galactic winds. In *Annu. Rev. Astron. Astrophys.*, volume 43, pages 769–826. Annual Reviews. 16

Voelk, H. J. (1989). The correlation between radio and far-infrared emission for disk galaxies - A calorimeter theory. *Astron. Astrophys. (ISSN 0004-6361)*, 218:67–70. 48

Wang, L., Gao, F., Duncan, K. J., Williams, W. L., Rowan-Robinson, M., Sabater, J., Shimwell, T. W., Bonato, M., Calistro-Rivera, G., Chyż Y, K. T., Farrah, D., Gürkan, G., Hardcastle, M. J., McCheyne, I., Prandoni, I., Read, S. C., Röttgering, H. J., and Smith, D. J. (2019). A LOFAR-IRAS cross-match study: The far-infrared radio correlation and the 150 MHz luminosity as a star-formation rate tracer. *Astron. Astrophys.*, 631. 49, 70, 71

Webber, J. C. and Willis, A. G. (1971). Radio continuum observations of maffei 2. *Nature*, 231(5297):36. 12

Werner, M. W. (2004). The spitzer space telescope mission. *Adv. Sp. Res.*, 36(6):1048–1049. 33

Wilkins, S. M., Lovell, C. C., Fairhurst, C., Feng, Y., Di Matteo, T., Croft, R., Kuusisto, J., Vijayan, A. P., and Thomas, P. (2020). Nebular-line emission during the Epoch of Reionization. *Mon. Not. R. Astron. Soc.*, 493(4):6079–6094. 8

Williams, W. L., Hardcastle, M. J., Best, P. N., Sabater, J., Croston, J. H., Duncan, K., Shimwell, T. W., Röttgering, H. J. A., Nisbet, D., Gürkan, G., Alegre, L., Cochrane,

R. K., Goyal, A., Hale, C. L., Jackson, N., Jamrozy, M., Kondapally, R., Kunert-Bajraszewska, M., Mahatma, V. H., Mingo, B., Morabito, L. K., Prandoni, I., Roskowinski, C., Shulevski, A., Smith, D. J. B., Tasse, C., Urquhart, S., Webster, B., White, G. J., Beswick, R. J., Callingham, J. R., Chy˙ Zy, K. T., De Gasperin, F., Harwood, J. J., Hoeft, M., Iacobelli, M., Mckean, J. P., Mechev, A. P., Miley, G. K., Schwarz, D. J., and Van Weeren, R. J. (2018). The LOFAR Two-metre Sky Survey III. First Data Release: optical/IR identifications and value-added catalogue. Technical report. 28, 38

Wilson, T. L. T. L., Rohlfs, K. K., and Hüttemeister, S. S. (1997). Tools of radio astronomy. *Choice Rev. Online*, 35(04):35–2078–35–2078. 26, 32

Woo, J. H., Schulze, A., Park, D., Kang, W. R., Kim, S. C., and Riechers, D. A. (2013). Do quiescent and active galaxies have different M BH-σ * relations? *Astrophys. J.*, 772(1):49. 16

Yun, M. S., Reddy, N. A., and Condon, J. J. (2002). Radio Properties of Infrared-Selected Galaxies in the IRAS 2 Jy Sample . *Astrophys. J.*, 554(2):803–822. 47